THE STUDY OF (p, d) REACTIONS ON ^{13}C, ^{11}B, AND ^{10}Be IN INVERSE KINEMATICS

By

Xiaodong Liu

A DISSERTATION

Submitted to
Michigan State University
in partial fulfillment of the requirements
for the Degree of

DOCTOR OF PHILOSOPHY

Department of Physics and Astronomy

2005

ABSTRACT

THE STUDY OF (p, d) REACTIONS ON ^{13}C, ^{11}B, AND ^{10}Be IN INVERSE KINEMATICS

By

Xiaodong Liu

This work studied the one neutron transfer reactions on ^{13}C, ^{11}B, and ^{10}Be in inverse kinematics using detectors with high angular and high energy resolution. The (p,d) reactions were performed using secondary beams of ^{13}C, ^{11}B, and ^{10}Be on polyethylene targets $(CH_2)_n$. The experiment was performed at the National Cyclotron Superconducting Laboratory (NSCL) at Michigan State University. Neutron spectroscopic factors have been extracted for the transfers from the ground states of ^{13}C, ^{11}B, and ^{10}Be to the ground states of ^{12}C, ^{10}B, ^{9}Be and from the ground state of ^{13}C to the first excited state of ^{12}C. The theories of DWBA and ADBA were reviewed and the approximations of zero-range, finite range, and non-locality were examined. Sensitivities of the optical–model potentials in the extraction of the spectroscopic factor were analyzed. The results of this work indicated that a transfer reaction in inverse kinematics provides a unique tool for the study of the structures of the radioactive nuclei and that reliable spectroscopic factors must be extracted with a systematic and consistent approach using global optical-model potentials.

To

my wife - Yu Liang

and

my daughter - Liying Liu

ACKNOWLEDGMENTS

First of all, I would express my deepest gratitude to my advisor, Dr. Betty M. Tsang. I could not have completed this thesis without her tremendous support and guidance. She taught me how to solve somehow impossible problems by detailed inspections and unremitting effort. The experience of making progress through gloomy zenith has been wonderful and invaluable. I also learned much from her enthusiasm for life as well as for the nuclei.

I own my sincere thanks to C. K. Gelbke, P. Hosmer, T. Liu, W. G. Lynch, R. Shomin, W. Tan, G. Verde, A. Wagner, M. Wallace, H. Xi and H. Xu. I am also indebted to L. Beaulieu, B. Davin, Y. Larochelle, T. Lefort, R. T. de Souza, R. Yanez and V. E. Viola from Indiana University, as well as R. J. Charity and L. G. Sobotka from Washington University. I would also express my gratitude to the REU students, K. Chalut, S. Farges, M. D. Lennek, M. Ramos, and S. Seun for their massive work.

I would like to thank Dr. F. Nunes, Dr. M. Famiano, and Dr. F. Delaunay for their great help on theoretical calculations and discussions. I am deeply indebted to Dr. J. A. Tostevin who offered the TWOFNR program from Surrey University and gave us invaluable help on theoretical analyses.

Great thanks to Dr. Daniel Bazin who taught me a lot about the S800 spectrometer and beam transmission. I would also thank Dr. Marc-Jan van Goethem and Michal Mocho for their help during my analyses.

Special thanks go to Dr. William G. Lynch who always gave me excellent ideas and philosophical understanding of physics throughout my thesis experiment and data analyses.

I would like to acknowledge the excellent support at the National Superconducting Cyclotron Laboratory at Michigan State University. I appreciate the help from J. Yurkon of the detector laboratory, L. Morris of the design group, J. Vincent of electronics group, R. Fox and B. Pollack of the computer group.

I would also like to thank Dr. S. D. Mahanti, Dr. B. Sherrill, and Dr. C. P. Yuan for reading my dissertation and also serving on my guidance committee.

Last but not least, I would like to thank my wife and my daughter for their love and belief in me.

TABLE OF CONTENTS

LIST OF TABLES

LIST OF FIGURES

CHAPTER 1

INTRODUCTION

1.1 Motivation

The study of nuclei far away from stability has been the focus of nuclear study in recent years. We want to know the extent to which the nuclear shell model theory is valid for nuclei beyond the stability limits. Such understanding is especially important since unstable nuclei are essential components in the nuclear synthesis process.

Since the discovery of the shell model, which explains many structural properties of the nuclei, transfer reactions have been used to study the configuration of the valence nucleons. Spectroscopic factors (SF) are important quantities that tell us the structure of the single nucleon orbit. In this work, we define the spectroscopic factor as the ratio of the experimental cross section from the transfer reaction to the theoretical calculation based on a reaction model that assumes the orbital fully occupied by the transferred nucleon. Since unstable nuclei cannot be made into targets, the transfer reactions must be performed in inverse kinematics using rare isotope beams.

Currently there are unanswered questions in the extraction of spectroscopic factors. In the reaction theory, which uses the Distorted-Wave Born Approximation, DWBA, a fast one-step direct process of less than 10^{-22} sec is assumed. Elastic scatterings are used to describe both the entrance and the exit channels. It is usually believed that an accurate optical-model potential, which is derived from the best fitting of the elastic scattering

data, would give the correct incoming and outgoing wave functions and hence the correct extraction of the spectroscopic factor. Unfortunately, such practice has failed to provide a consistent extraction of the spectroscopic factors in part due to the ambiguity in the parameters needed to describe the optical-model potential. In contrast, there are also arguments that superior results would be obtained if global optical-model potentials that describe a range of nuclei and incident energies are used instead. There are statements in literature that such an average optical-model potential tends to give more reasonable spectroscopic factors than individual potential [Sch67]. However, such statements have not been well quantified. One purpose of this thesis is to compare the different strategies and find a reliable method to extract consistent spectroscopic factors.

Another goal of this work is to study the structure of deformed unstable nuclei such as ^{10}Be via the (p,d) reaction. It was envisioned that this would become the starting point of a series of studies of the N=6 isotones in inverse kinematics. The valence neutron of ^{10}Be had been previously studied via the ^{9}Be(d,p)^{10}Be reaction. The extracted spectroscopic factors, however varied from 0.97 to 2.07, in some cases differing from the theoretical value of 2.35 based on the shell model. We want to know if there is new physics in ^{10}Be that makes it different from the shell model expectation. Furthermore, understanding the structure of ^{10}Be may help us to understand the structure of more neutron-rich isotopes of Beryllium such as ^{11}Be.

This is the first time that the secondary radioactive beam of ^{10}Be was used to perform the (p,d) reaction in inverse kinematics. For these experiments, we used a high-angular and high-energy resolution detector, Large Area Silicon Strip Array (LASSA), to detect

the deuterons emitted in the reactions. In addition, we also measured (p,d) reactions on another N=6 isotone ^{11}B as well as ^{13}C. This letter reaction was used to obtain energy calibrations. High quality data were obtained in this reaction and used in our systematic studies to find a strategy to extract the spectroscopic factor.

Various properties of the inverse kinematic reaction are analyzed in the next section. The theoretical background is presented in chapter 2. This latter chapter includes the description of the theoretical spectroscopic factor (Section 2.2) and of the reaction theories (Section 2.3). Specifically, the theories of distorted-wave Born approximation (DWBA) and adiabatic deuteron breakup approximation (ADBA) are introduced in Section 2.3.1 and Section 2.3.2 respectively. Detailed descriptions of the experimental setup are provided in chapter 3, which includes the descriptions of the various detectors and electronics. Chapter 4 describes the analyses of the deuteron spectra and the extraction of the angular differential cross sections. Theoretical calculations and the extraction of the spectroscopic factors are explained in chapter 5. Chapter 6 gives the summary of this thesis.

1.2 Inverse Kinematics

Nuclear reactions involving nucleon transfer between stable beams and target nuclei have been a very useful source of nuclear structure information, and many theoretical tools have been developed to extract spectroscopic information. However, for the study of radioactive nuclei far from the stable region, which has become the new focus of studies in nuclear astronomy and nuclear structure beyond the shell model in recent years,

inverse kinematics becomes necessary since the radioactive nuclear targets, especially those with a very short half-life, are usually not available. Thus, transfer reactions induced by radioactive beams on proton and deuteron targets have great potential for probing single-particle structures in new regions [For99, Win01, Reh98, Oga99].

One advantage of the inverse kinematic reaction is that it is relatively easy to cover the forward scattering angle in the center of mass. In the normal kinematic reaction, where the light projectile bombards the heavy target, the small scattering angle in the center of mass can only be covered at the most forward angle in the laboratory frame. Figure 1.1(a) shows the velocity diagram for the (p,d) reaction in normal kinematics, where $V_0{}^{cm}$ is the velocity of the center of mass in the laboratory frame; $V_d{}^{lab}$ and $V_d{}^{cm}$ are the deuteron velocity in the laboratory frame and in the center of mass; θ_{lab} and θ_{cm} are deuteron emitted angles in the laboratory and in the center of mass. In the inverse kinematic reaction, as shown in Figure 1.1(b), the deuteron scatters backward in the center of mass. Smaller θ_{cm} can be obtained at relatively large θ_{lab}. Figure 1.2 shows the relations between the deuteron emitted angles in the laboratory frame and the emitted angles in the center of mass for the reactions of p(^{13}C,d)^{12}C g.s. (solid line) and ^{13}C(p,d)^{12}C g.s. (dashed line) at the equivalent bombing energy respectively. The detector in the inverse kinematic reaction covers smaller angles in the center of mass than that in a normal kinematic reaction at the same laboratory angle.

One disadvantage of inverse kinematics is the kinematic broadening. Figure 1.3 shows the kinematic broadening vs. the emitting angle in the laboratory frame. The solid line presents the inverse kinematic reaction of p(^{13}C,d)^{12}C at bombing energy of 47.9

MeV per nucleon; the dashed line stands for the $^{13}C(p,d)^{12}C$ reaction at a proton energy of 48.3 MeV. Except for the very forward angles, the kinematic broadening is much more severe for the inverse kinematic reaction than the normal kinematic reaction. For example, the kinematic broadening increases dramatically from 650 keV at 30 degree to 1.27 MeV at 35 degree Therefore in this reaction, deuterons should not be detected beyond 35 degree in the laboratory frame. For the forward angles, detectors with high angular resolution as well as high energy resolution are required. Silicon strip detectors are widely employed to achieve high angular resolution and high energy resolution. The techniques of using these detectors will be discussed in Section 3.3.

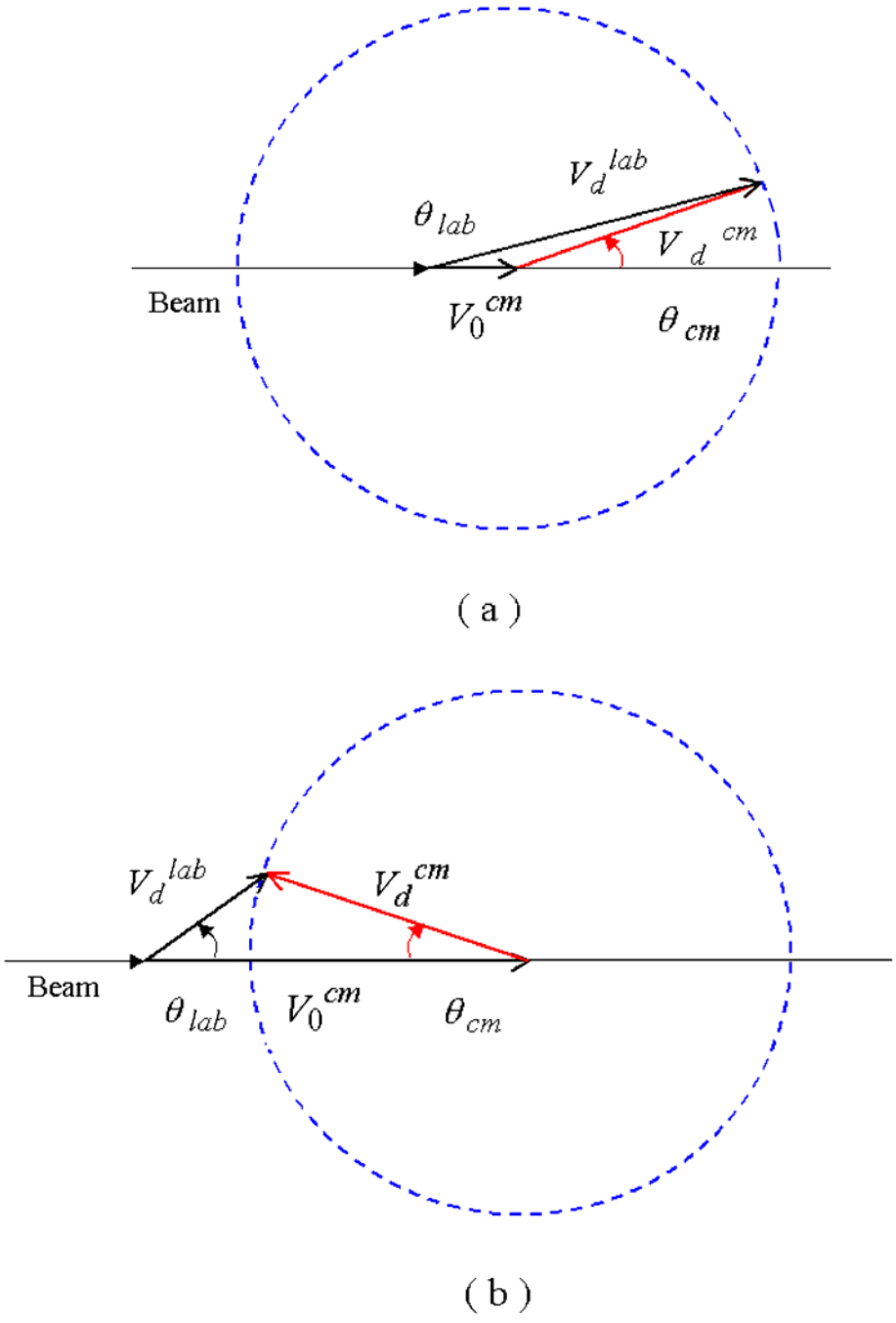

Figure 1.1: Velocity diagrams for normal kinematics (a) and inverse kinematics (b) as in (p,d) reactions. V_0^{cm} is the velocity of the center of mass in the laboratory frame; V_d^{lab} and V_d^{cm} are the deuteron velocities in the laboratory frame and the center of mass, respectively; θ_{lab} and θ_{cm} are the emitted angles in the laboratory frame and the center of mass, respectively.

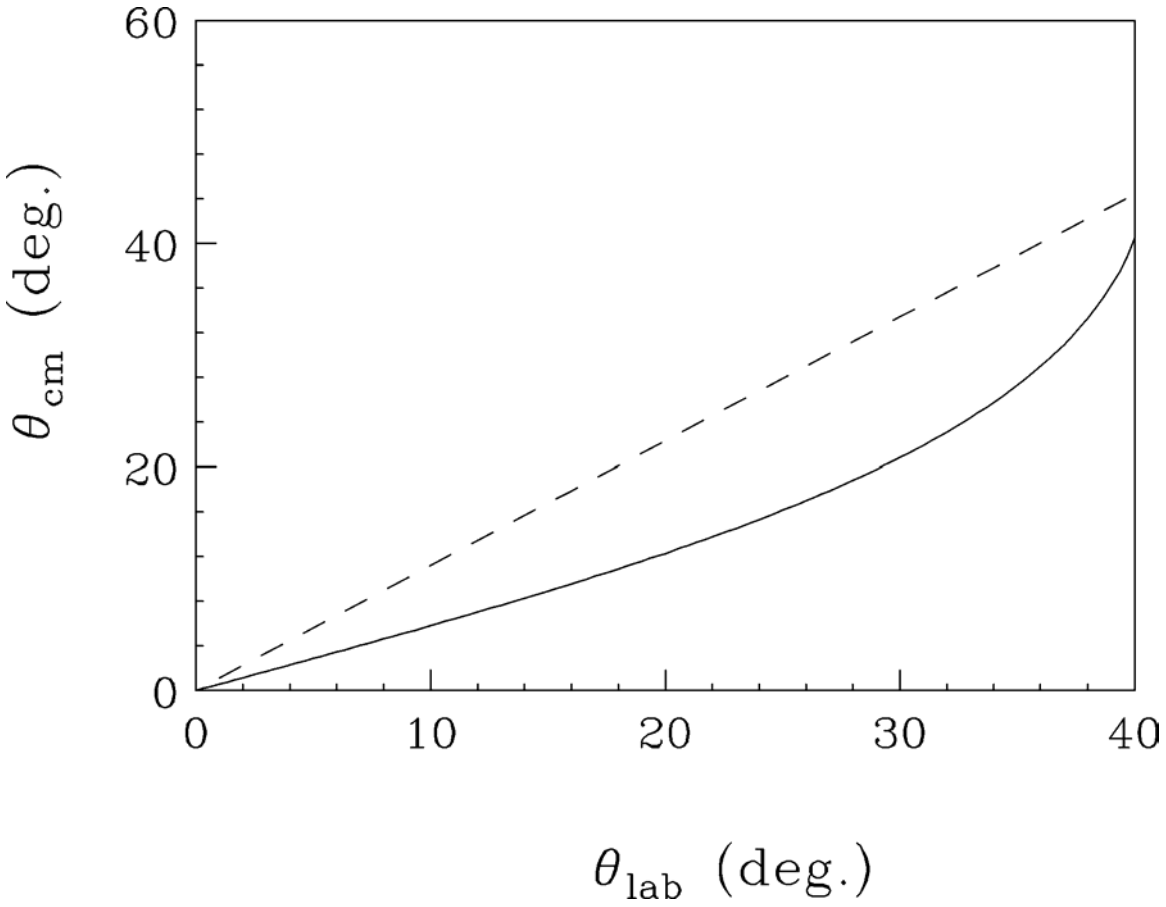

Figure 1.2: The deuteron emitted angles in the center of mass vs. emitted angles in the laboratory frame. The solid line presents the inverse kinematic reaction of $p(^{13}C,d)^{12}C$ (g.s.) at bombing energy of 47.9 MeV per nucleon; the dashed line stands for the reaction of $^{13}C(p,d)^{12}C$ (g.s.) at proton energy of 48.3 MeV.

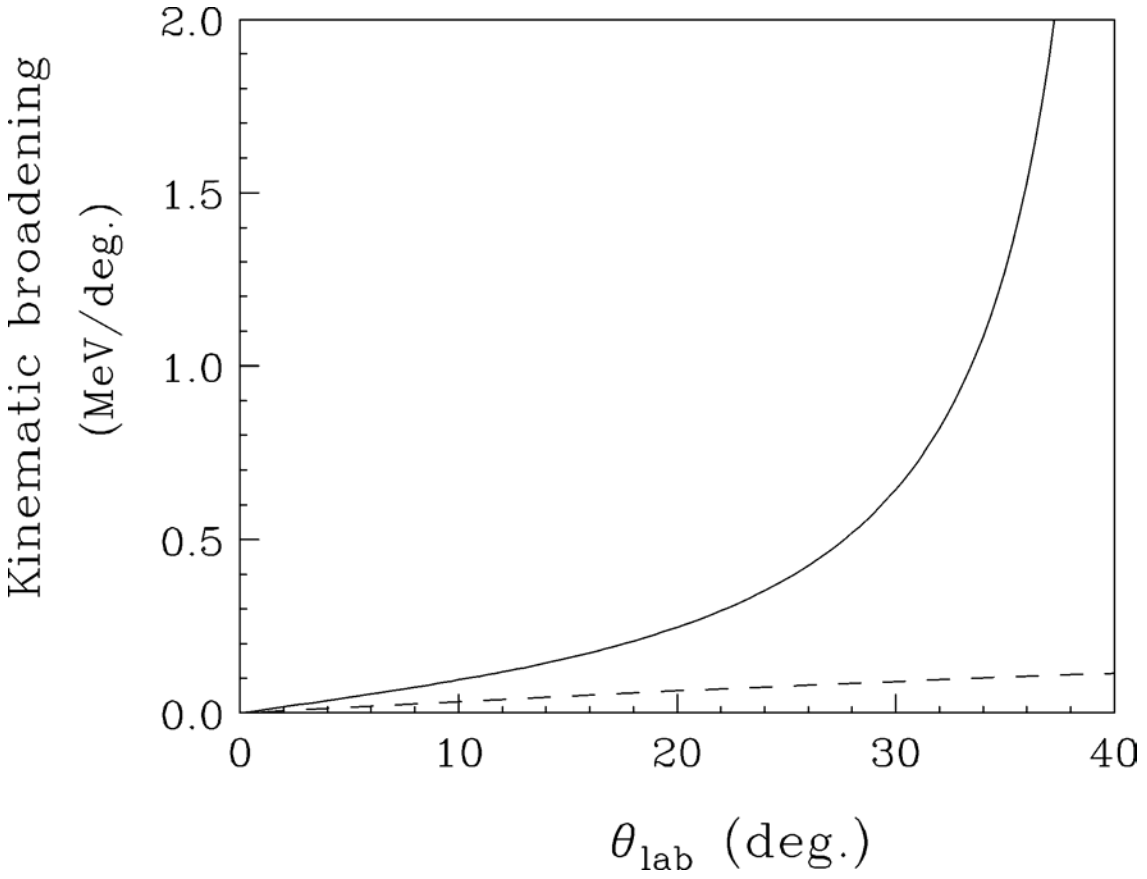

Figure 1.3: Kinematic broadening vs. angles in the laboratory frame. The solid line presents the inverse kinematic reaction of $p(^{13}C,d)^{12}C$ at bombing energy of 47.9 MeV per nucleon; the dashed line stands for the reaction of $^{13}C(p,d)^{12}C$ at proton energy of 48.3 MeV.

CHAPTER 2

THEORETICAL DESCRIPTION

2.1 Overview

The main goal of this thesis is the extraction of the neutron spectroscopic factors from measurements. The experimental spectroscopic factor is defined as the ratio of the experimental differential cross section to the calculated differential cross section based on a reaction model that assumes the relevant orbit is fully occupied. The extraction of the experimental differential cross sections measured in this thesis will be described in Chapter 4. This chapter mainly describes how the theoretical differential cross sections are calculated. The theoretical nucleon spectroscopic factor will be introduced in Section 2.2. The most widely used models, the distorted-wave Born approximation (DWBA) and the adiabatic deuteron breakup approximation (ADBA), will be discussed in Section 2.3. The effects of different input parameters including the choices of optical-model potentials in DWBA will be covered in the subsections of Section 2.3. At the end of this chapter, a list of standard input parameters for the DWBA and ADBA calculations will be proposed.

2.2 Theoretical Spectroscopic Factor

In the theory of the shell model, the valence nucleon in the nucleus is described as a single-particle state of a particular orbit. Each orbit is assigned the number n, l, and j corresponding to the node number, the orbital momentum, and the total spin momentum of the nucleon. The assumption that the nucleon occupies a pure single-particle state is an idealization, which is true only in few cases in real nuclei. Due to the interactions among other nucleons, each nucleon may occupy several single-particle states. The occupation of a nucleon in a pure single-particle state is called the *spectroscopic factor,* which contains the information of the nuclear structure and how well the shell model theory describes the real nuclei. Thus the nucleon spectroscopic factor is among the most fundamental tests of shell model theory [Ban85].

In a nucleus composed of A nucleons, the spectroscopic factor can be deduced from the expansion of the wave function $\psi(A)$ in terms of a summation over the complete set of single-particle states $\phi_{nlj}(\vec{r}_n)$ and the states $\psi(B)$ of the residual core nucleus B is composed of A-1 nucleons [Gle04]:

$$\psi_{JA}^{MA}(B,\vec{r}_n) = \sum_{B'jl} \beta_{njl}(A,B')\hat{\mathrm{A}}[\phi_{nlj}(\vec{r}_n)\psi_{JB'}(B)]_{JA}^{MA} \qquad (2.2.1)$$

where $\hat{\mathrm{A}}$ is an antisymmetrization operator, $\beta_{nlj}(A,B')$ are coefficients of fractional parentage and their values depend on the detailed structure of the nuclear wave function.

The square bracket denotes vector coupling:

$$\left[\phi_{nlj}(\vec{r}_n)\psi_{JB'}(B)\right]_{JA}^{MA} = \sum_{M'm} C_{M'mMA}^{JB'jJA}\,\phi_{nlj}^{m}(\vec{r}_n)\,\psi_{JB'}^{M'}(B) \tag{2.2.2}$$

The spectroscopic factor for a specific single particle state `(nlj)` is:

$$S_{nlj} = \beta_{nlj}{}^2(A,B') \tag{2.2.3}$$

For the pickup (p,d) reaction, the spectroscopic factor is related to the experimental angular differential cross section and the theoretical calculation by:

$$\frac{d\sigma(\theta)}{d\Omega} = S_{nlj}\cdot\left(\frac{d\sigma(\theta)}{d\Omega}\right)_{theory} \tag{2.2.4}$$

where $\left(\frac{d\sigma(\theta)}{d\Omega}\right)_{theory}$ is calculated assuming the neutron in the exact state (`nlj`). The theoretical calculations are performed either in the distorted-wave Born approximation (DWBA) theory or in the adiabatic deuteron breakup approximation (ADBA) theory. The introduction of the theories will be in Section 2.3. In this work, all the theoretical calculations for (p,d) and (d,p) reactions are performed using the code TWOFNR, which was initially developed by M. Igarashi in 1977 [Iga77]. This code is relatively easy to use since it supplies multiple options with default values for every step and component in the calculations. All the inputs, including the parameters and option choices, are converted automatically into a standard input file for TWOFNR by a partner program FRONT. The input parameters and options are listed in Table 2.1. For example, the integration ranges and the number of partial waves can be specified by the user or the default values can be adopted. The user can choose the global optical-model potentials for proton and deuteron or specify the parameters for individual potential. When the ADBA theory is employed, the Johnson-Soper adiabatic potential for deuteron can be constructed using three

different nucleon-nucleus potentials. For the application of JLM potential, users can input their own parameters for the target density and potential scaling factors following the prompts of the program. There is a switch either to zero-range approximation or to finite-range approximation. If the finite-range approximation is chosen, the finite-range factor can be the default value or be specified. The same strategy is also applied to the options of neutron binding potential, the vertex constant, and non-locality correction.

We choose to use TWOFNR because there are many default options available and it is easier to perform many calculations in a systematic study. Another popular finite-range DWBA code is DWUCK5 [Kunz], which performs finite-range calculations with deuteron wave function instead of the finite-range approximation in TWOFNR. We compared them in Section 2.3.1.3 and found that the results from these two programs are very close to each other for the same input parameters (see Figure 2.19). We believe essentially the same results will be calculated if different codes than TWOFNR are used.

Table 2.1: An overview of the input parameters and options for TWOFNR

Integration ranges	Specified or default value (30 fm in 300 steps)
Number of partial waves	Specified or default value (70)
Proton potential	Choose built-in options of global optical-model potentials: Bechetti-Greenlees; Chapel-Hill 89 (CH89); Perey & Perey; Menet; JLM; Or specified parameters for V_r, r_v, a_v, W_v, W_s, r_w, a_w, V_{so}, r_{so}, a_{so}, and R_C
Deuteron potential	Choose built-in options of global optical-model potentials: Lohr-Haeberli; Perey & Perey; Daehnick; Johnson-Soper adiabatic (ADBA); Or specified parameters for V_r, r_v, a_v, W_v, W_s, r_w, a_w, V_{so}, r_{so}, a_{so}, and R_C
Johnson-Soper adiabatic potential	Choose built-in options of global optical-model potentials: Bechetti-Greenlees; Chapel-Hill 89 (CH89); JLM;
Target density for JLM potential	Choose built-in options: Negele form; Specify rms radius; Modified Harmonic oscillator form;
JLM potential scaling λ	Specified or default values (λ_v=1.0, λ_w=0.8)
Neutron binding potential	Specified or default values (r_0=1.25 fm, a_0=0.65 fm, V_{so}=6 MeV)
Zero-range approximation	Use or not
Finite-range approximation	Use or not If use, finite range factor can be specified or choose default value of 0.7457 fm
Vertex constant ${D_0}^2$	Specified or default value of 15006.25 $MeV^2 \cdot fm^3$
Non-locality correction	Use or not. If use, non-locality range can be specified or choose default value (0.85 fm for proton; 0.54 fm for deuteron).

2.3 Reaction Theory

2.3.1 Distorted-Wave Born Approximation (DWBA)

Transfer reactions have been an important tool in the study of nuclear structure. The results obtained from the studies of the pickup A(p,d)B and stripping B(d,p)A reactions, involving single neutron transfer, help to validate the nuclear shell model by identifying the single-particle states. To a large extent, the (p,d) reaction can be understood as one in which the neutron is removed from a single particle state of the target nucleus A. In the (d,p) reaction the neutron in the deuteron is deposited to a single-particle state of the final nucleus A. Thus, the theoretical description of the (d,p) reaction is similar to that of the (p,d) reaction.

In the pickup reactions, A(p,d)B, where A=B+n, a neutron in a single-particle state in A, is picked up by the incident proton to form the deuteron. The process is illustrated in Figure 2.1. The transition amplitude for this reaction under the distorted-wave Born approximation (DWBA) theory is written as [Gle04]:

$$T(\mu_p J_A M_A \rightarrow \mu_d J_B M_B) = \sum_{lj} C^{JBjJA}_{MBmjMA} C^{(1/2)(1/2)(1)}_{\mu p \mu n \mu d} C^{l(1/2)j}_{ml\mu nmj} \cdot i^l \, (2l+1)^{1/2} B^{ml}_{l} S^{1/2}_{nlj} \tag{2.3.1}$$

where

$$B_l^{ml}(\vec{k}_p,\vec{k}_d) = i^{-l}(2l+1)^{-(1/2)}\int \chi_d^{(-)*}(\vec{k}_d,\vec{R})\phi_{nl}^{ml}(\vec{r}_n) \cdot (V_{pn}+V_{pB}-U_p)\phi_d(\vec{r})\cdot \chi_p^{(+)}(\vec{k}_p,\vec{r}_p)\,d\vec{r}_n d\vec{r}_p \tag{2.3.2}$$

$$S_{nlj}^{1/2} = \int \psi_{JA}^{MA*}(\vec{A})\hat{\mathrm{A}}\left[\psi_{JB}(\vec{B})\phi_{nlj}(\vec{r}_n,\vec{\sigma}_n)\right]_{JA}^{MA} d\vec{B}d\vec{r}_n$$

where $\vec{A}$ and $\vec{B}$ refer to the nucleon coordinates and spins of nucleus A and B; $\vec{r}_n$ and $\vec{r}_p$ are the coordinates of neutron and proton; $\vec{r}_n$ and $\vec{R}$ are the relative and center-of-mass coordinates of the deuteron; $\chi_p{}^{(+)}(\vec{k}_p,\vec{r}_p)$ is the distorted-wave function describing the elastic scattering of the incoming proton by the proton optical-model potential U_p; the distorted-wave function $\chi_d{}^{(-)*}(\vec{k}_d,\vec{R})$ describes the elastic scattering of the emitted deuteron by the deuteron optical-model potential U_d; $\psi(\vec{A})$ is the wave function of the target nucleus A; $\psi(\vec{B})$ is the wave function of the core nucleus B; and $\phi_d(\vec{r})$ is the internal wave function of the deuteron. The term $V_{pn}+V_{pB}-U_p$ is called the *residual interaction*, where V_{pn} is the interaction between the proton and neutron, and V_{pB} is the interaction between the proton and the remaining B nucleus. The term $\phi_{nlj}(\vec{r}_n,\vec{\sigma}_n)$ is the neutron wave function in specific single-particle state *(nlj)*, which is also called the *neutron form factor*:

$$\phi_{nlj}^{m}(\vec{r}_n,\vec{\sigma}_n) = \left[\phi_{nl}(\vec{r}_n)X_{1/2}(\vec{\sigma}_n)\right]_j^m \tag{2.3.3}$$

$$\phi_{nl}^{ml}(\vec{r}_n) = u_{nl}(r_n)Y_l^{ml}(\vec{r}_n) \tag{2.3.4}$$

Assuming V_{pB} and U_p approximately cancel each other in Equation 2.3.2 [Aus70, Sat71], the $B_l^{ml}(\vec{k}_p, \vec{k}_d)$ becomes

$$B_l^{ml}(\vec{k}_p, \vec{k}_d) = i^{-l}(2l+1)^{-(1/2)} \int \chi_d^{(-)*}(\vec{k}_d, \vec{R}) \phi_{nl}^{ml}(\vec{r}_n) \cdot V_{pn} \cdot \phi_d(\vec{r}) \cdot \chi_p^{(+)}(\vec{k}_p, \vec{r}_p)\, d\vec{r}_n d\vec{r}_p \tag{2.3.5}$$

The cross section is

$$\frac{d\sigma}{d\Omega}(\mu_p J_A M_A \rightarrow \mu_d J_B M_B) = \frac{m_d m_p}{(2\pi\hbar^2)^2} \frac{k_d}{k_p} |T|^2 \tag{2.3.6}$$

where m_d and m_p are the reduced masses.

In order to obtain the distorted-wave functions of $\chi_d{}^{(-)*}$ and $\chi_p{}^{(+)}$, we need the optical-model potentials for the deuteron and proton. In the next section, the choices and detailed descriptions about the optical-model potentials will be discussed.

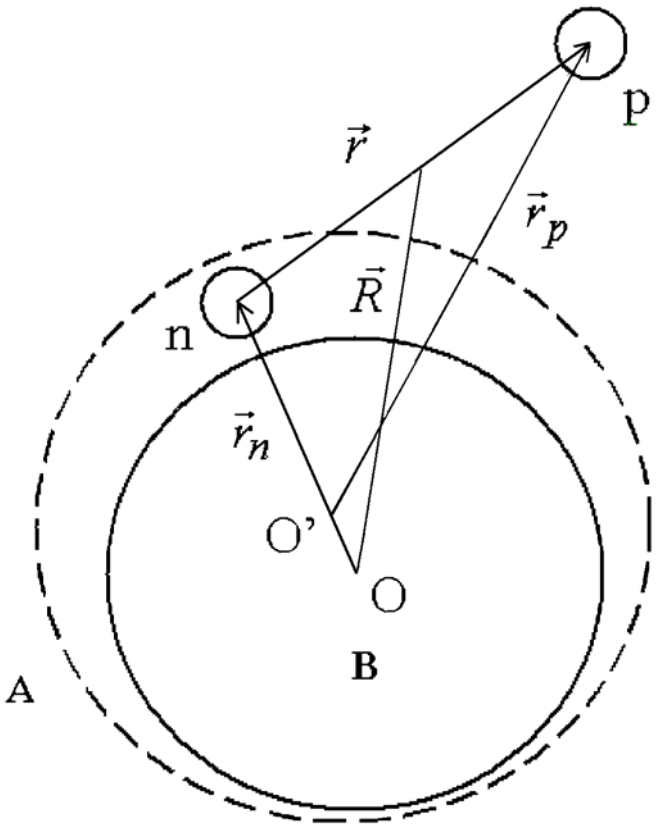

Figure 2.1. The target nucleus A is composed of the core nucleus B and one neutron n. The proton picks up a neutron to form the deuteron. O is the center of mass of nucleus B and $\vec{r}_n$ points to the neutron; O' is the center of mass of nucleus A; $\vec{r}$ and $\vec{r}_p$ are the proton coordinates relative to the neutron and the center of mass of nucleus A, respectively. $\vec{R}$ is the coordinate of the deuteron center relative to nucleus B.

2.3.1.1 Optical-Model Potentials

2.3.1.1.1 Overview

The Schrödinger equation of the collision system of $a + b$ can be written as:

$$(H - E)\Psi = 0 \tag{2.3.7}$$

where H includes the intrinsic energy H_0, the kinetic energy T, and the potential U between a and b:

$$H = H_0 + T + U \tag{2.3.8}$$

The Schrödinger equation is separable into the nuclear intrinsic coordinates and relative coordinates so that the solution ψ can be written as a product of the nuclear intrinsic wave function $\psi_a \psi_b$ and a relative wave function $\phi(\vec{r})$, which satisfies the *optical-model* Schrödinger equation:

$$(T + U - E)\,\phi(\vec{r}) = 0 \tag{2.3.9}$$

Since U depends only on the relative coordinates of the two nuclei, it produces no change in the nuclei and describes only the elastic scattering. As the nucleon force is short-ranged, and since the density ρ of nucleons in the nucleus is fairly constant in the interior and falls smoothly to zero at the nuclear surface, it is reasonable to assume that U has a radial shape that is similar to the density. Usually the optical potential is expressed in the Woods-Saxon form [Woo54]:

$$
\begin{aligned}
U(r) = & -V_v f(r, R_v, a_v) - iW_V f(r, R_w, a_w) \\
& + 4iW_s a_w \frac{d}{dr} f(r, R_w, a_w) \\
& + 2.0(V_{so} + iW_{so})(\frac{1}{r}\frac{d}{dr} f(r, R_{so}, a_{so})\vec{L}\cdot\vec{\sigma}) \\
& + V_c
\end{aligned}
\tag{2.3.10}
$$

where the Woods-Saxon shape function $f(r, R_k, a_k)$ is :

$$
f(r, R_k, a_k) = \frac{1}{1 + \exp[(r - R_k)/a_k]}, \qquad R_k = r_k \cdot A^{\frac{1}{3}} \tag{2.3.11}
$$

Here r_k is the radius parameter and a_k is the diffuseness parameter; V_v and W_v are the depths of the real and imaginary potentials, respectively; Ws is the depth of surface term of the imaginary potential. Vso and Wso are the depths of the real and imaginary parts of the spin-orbit potentials; $\vec{L}$ is the orbital angular momentum of the relative motion of the scattered particle; and $\vec{\sigma}$ is the spin operator. V_C is the Coulomb interaction, which is taken for a uniformly charged sphere of radius R_C with different expressions inside and outside the radius R_C .

$$
Vc = \begin{cases} \dfrac{Z_a Z_b e^2}{r}, & r \geq R_c \\ \dfrac{Z_a Z_b e^2}{2R_c}(3 - \dfrac{r^2}{{R_c}^2}), & r \leq R_c \end{cases} \tag{2.3.12}
$$

2.3.1.1.2 Global Optical-Model Potentials

In principle, all the parameters of the optical-model potential can be obtained by fitting them to the experimental data of the elastic scattering. For the best fit to individual

nucleus at specific energy, all parameters could be optimized. However, the parameters of the optical potential usually vary smoothly with energy and are similar for neighboring nuclei. Thus global optical potentials could be obtained by fitting a group of nuclei with a total of N points in a certain energy range by minimizing χ^2:

$$\chi^2 = \frac{1}{N}\sum_{i=1}^{N}\left(\frac{\sigma_{th}(\theta_i) - \sigma_{\exp}(\theta_i)}{\Delta\sigma_{\exp}(\theta_i)}\right)^2 \tag{2.3.13}$$

where σ_{th} and $\sigma_{\exp}$ are the calculated and experimental values of the cross sections at an angle of θ_i and $\Delta\sigma_{\exp}$ is taken to be the experimental error; N is the number of data points.

Over the years, many global optical potentials have been developed for both protons and deuterons. In the following sections, we discuss mainly those potentials which have been provided as options for TWOFNR [Iga77] that we have used to calculate the theoretical differential cross sections.

2.3.1.1.3 Proton Global Optical-Model Potentials

In this section, we introduce three sets of proton global optical-model potentials developed by Bechetti-Greenlees [Bec69], Menet [Men71], and Perey & Perey [Per76]. The Becchetti-Greenlees [Bec69] global proton potential has been developed for A>40 nuclei and proton energies up to 50 MeV. Menet [Men71] developed a global proton potential for 12<A<208 nuclei and proton energies from 30 MeV to 60 MeV. The global proton potentials developed by Perey & Perey [Per76] are good for 30<A<100, and

proton energies up to 20 MeV. The parameters of the above three global optical potentials are listed in Table 2.2.

Figure 2.2 shows the real (upper panel of figure) and imaginary (lower panel) global proton potentials on ^{13}C at proton energy of 12.5 MeV. These potentials have very similar shapes and depths in the surface regions of the real parts, which dominate the scattering at the forward angles. However, there is a lot of difference among the imaginary parts, which scatter more strongly at large angles. Figure 2.3 shows the calculations based on the above global potentials and the comparison to the proton elastic scattering data on ^{13}C at an incident energy of 12.5 MeV [Wel78]. The calculation by Menet potential gives a higher cross section, and the potentials of Perey & Perey and Bechetti-Greenlees give similar cross sections up to 56 degree in the center of mass.

Figure 2.4 shows the real (upper panel of the figure) and imaginary (lower panel) global proton potentials on ^{13}C at proton energy of 30.95 MeV. These potentials also have similar shapes and depths at the surface regions of the real parts. The imaginary parts are different. Figure 2.5 shows calculations based on the above global potentials and the comparison to the proton elastic scattering data on ^{13}C at an incident energy of 30.95 MeV [Bar88]. The calculations agree with each other rather well at the forward angles (less than 10° in the center of mass) and start to differ from each other for angles larger than 15° in the center of mass. We see that, at higher energy, the potentials of Menet and Bechetti-Greenlees give similar results up to 80° and the potential of Perey & Perey gives lower cross section compared to others.

Based on the above comparisons, we see that the proton global optical-model potentials give consistent calculations at forward angles, less than 10°. They give

relatively good fitting to the data in the region from 10° to 40°. Since the extraction of a spectroscopic factor is mostly determined by the reaction in forward angles, proton global potentials may provide a reasonable approach for describing the elastic scattering channel. In Section 2.3.1.1.5 and 2.3.1.1.6, we will introduce, respectively, potentials of CH89 and JLM, which improve the accuracy of the proton potential based on the folding model and nuclear matter approaches.

Table 2.2: The parameters of global proton potentials

Parameters \ Potentials	Bechetti-Greenlees (proton) [Bec69]	Menet (proton) [Men71]	Perey & Perey (proton) [Per76]
A	A>40	12<A<208	30<A<100
E	E<50 MeV	30<E<60 MeV	E< 20 MeV
V_v	$54.0-0.32E+24.0\frac{N-Z}{A}+0.4Z\cdot A^{-1/3}$	$49.9-0.22E+26.4\frac{N-Z}{A}+0.4Z\cdot A^{-1/3}$	$53.3-0.55E+27\frac{N-Z}{A}+0.4Z\cdot A^{-1/3}$
r_v	1.17	1.16	1.25
a_v	0.75	0.75	0.65
W_v	Max [(0.22E-2.7),0]	$4.2-0.05E+15.5\frac{N-Z}{A}$	13.5
r_w	1.32	1.37	1.25
a_w	$0.51+0.7\frac{N-Z}{A}$	$0.74-0.008E+1.0\frac{N-Z}{A}$	0.47
W_s	$\text{Max}[11.8-0.25E+12.0\frac{N-Z}{A}, 0]$	1.2+0.09E	0.0
V_{so}	6.2	6.04	7.5
r_{so}	1.01	1.064	1.25
a_{so}	0.75	0.78	0.47
R_C	1.25	1.25	1.25

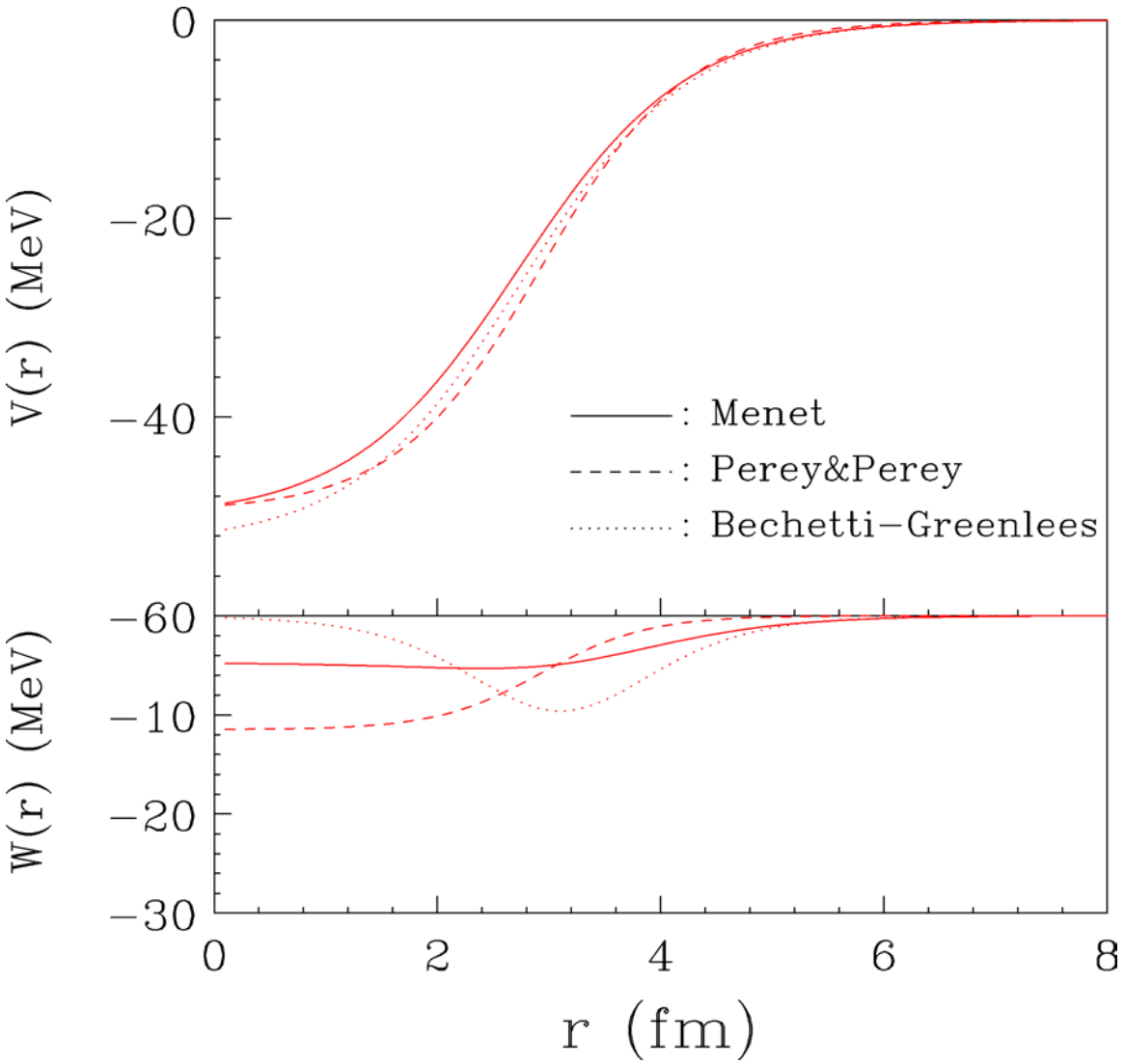

Figure 2.2: Proton global optical-model potentials of ^{13}C at incident energy of 12.5 MeV.

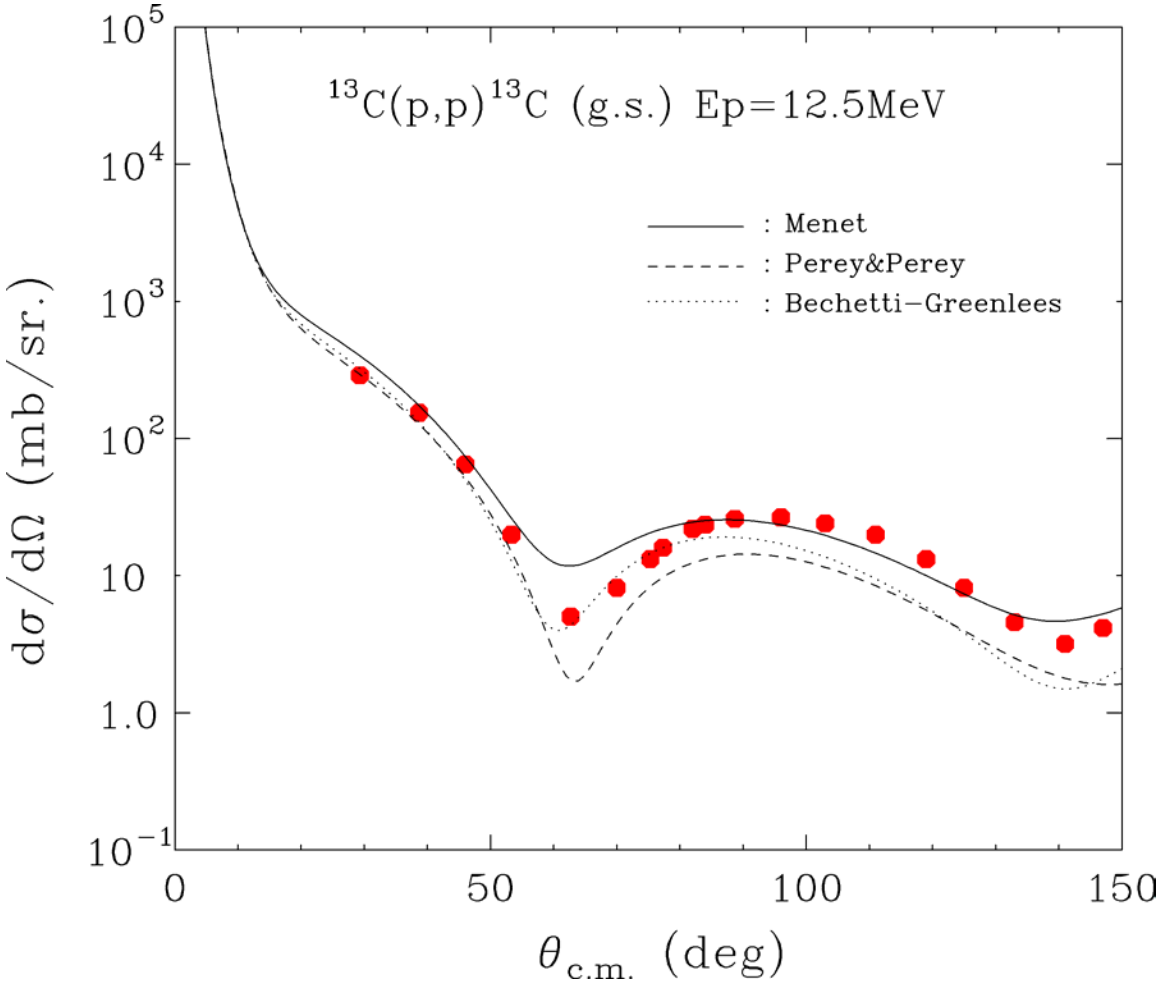

Figure 2.3: Calculations by different global optical-model potentials for the reaction of ^{13}C(p,p)^{13}C (g.s.) at incident energy of 12.5 MeV compared with the data [Wel78].

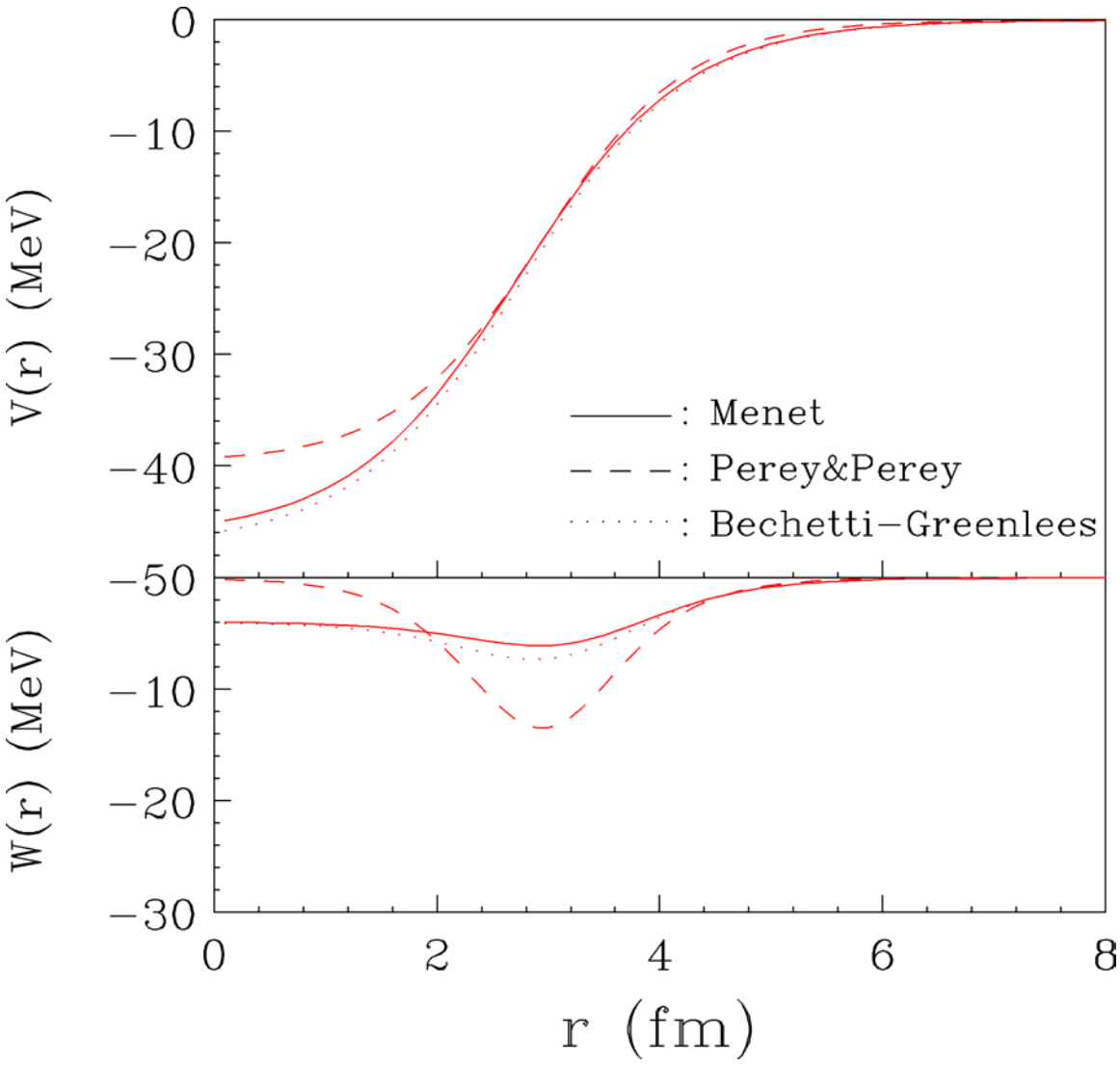

Figure 2.4: Proton global optical-model potentials of ^{13}C at incident energy of 30.95 MeV.

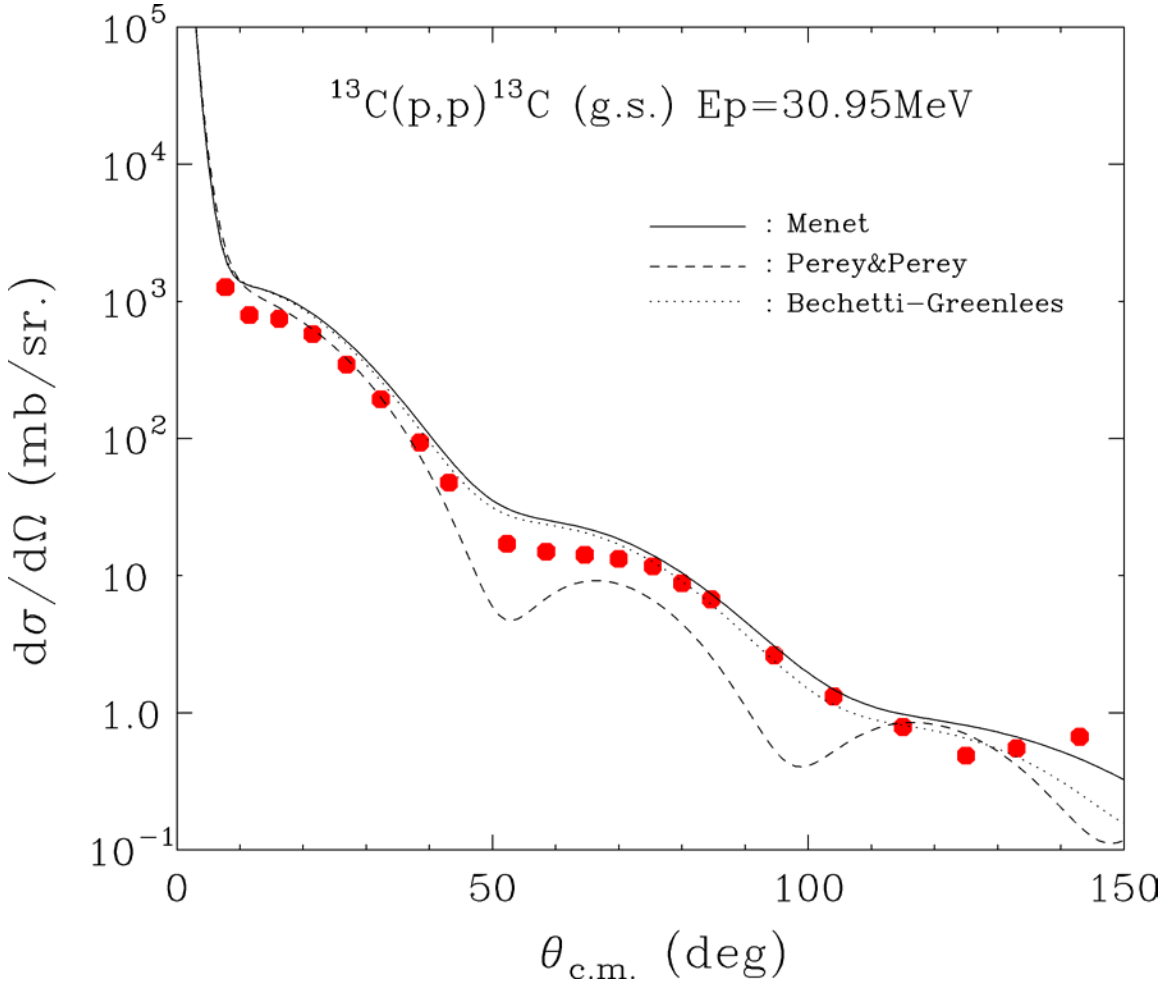

Figure 2.5: Calculations by different global optical-model potentials for the reaction of ^{13}C(p,p)^{13}C (g.s.) at incident energy of 30.95 MeV compared with the data [Bar88].

2.3.1.1.4 Deuteron Global Optical-Model Potentials

There are three widely-used deuteron global optical-model potentials: Lohr-Haeberli [Loh74], Perey & Perey [Per76], and Daehnick [Dae80]. These three potentials are available as options in the code of TWOFNR [Iga77].

The Lohr-Haeberli deuteron global potential is for nuclei with A>40 and for deuteron energies from 8 MeV to 13 MeV; the Perey & Perey deuteron global potential is for nuclei with Z≥12 and deuteron energies from 12 MeV to 25 MeV; the Daehnick deuteron potential spans the energy range from 11.8 MeV to 90 MeV and includes nuclei ranging in mass from ^{27}Al to ^{238}Th. The parameters of the above three global optical-model potentials are listed in Table 2.3.

As a comparison, Figure 2.6 shows the three global deuteron potentials of ^{12}C at incident deuteron energy of 11.8 MeV. Figure 2.7 shows the elastic scattering calculations based on the above global potentials, together with the experimental data at incident energy of 11.8 MeV [Fit67]. Unlike Figure 2.3 and Figure 2.5, Figure 2.6 plots the ratios of scattering differential cross section divided by the Rutherford differential cross section. The calculations agree with each other at the forward angles (less than 25°), but there exist slight deviations from the data.

Figure 2.8 shows the three global deuteron potentials on ^{12}C at incident deuteron energy of 34.4 MeV. Figure 2.9 shows the elastic scattering calculations with the experimental data at 34.4 MeV [New67]. The calculations agree with each other within the standard error of 5.3% at the forward angles (less than 20°), and they fit the elastic scattering well up to 36° in the center of mass.

Based on the above comparisons, we see that the present deuteron global optical-model potentials describe the deuteron elastic scattering better at higher energy than at lower energy and at smaller scattering angles better than at larger scattering angles. At higher energy, The Daehnick potential gives better fitting than others, so we choose Daehnick deuteron potential in our DWBA analyses. For the ADBA, we use the adiabatic deuteron potential that will be introduced in Section 2.3.2.

Table 2.3: Deuteron global parameters. N=neutron number, E=deuteron laboratory energy in MeV. For Daehnick potential, $\beta = -(\frac{E}{100})^2$, $\mu_i = (\frac{M_i - N}{2})^2$, where M_i = magic numbers (8,20,28,50,82,126).

Potentials / Parameters	Lohr-Haeberli (deuteron) [Loh74]	Perey & Perey (deuteron) [Per76]	Daehnick (deuteron) [Dae80]
A	A>40	Z≥12	27<A<238
E	8<E<13MeV	12MeV<E<25MeV	11.8<E<90MeV
V_v	$91.13 + 2.2Z \cdot A^{-1/3}$	$81.0\text{-}0.22E + 2.0Z \cdot A^{-1/3}$	$88.5\text{-}0.26E + 0.88Z \cdot A^{-1/3}$
r_v	1.05	1.15	1.17
a_v	0.86	0.81	0.709+0.0017E
W_v	-	0.0	$(12.2+0.026E)(1-e^{\beta})$
r_w	1.43	1.34	1.325
a_w	$0.50+0.013\ A^{2/3}$	0.68	$0.53 + 0.07A^{1/3} - 0.04\sum_i e^{-\mu i}$
W_s	$218A^{-2/3}$	14.4+0.24E	$(12.2+0.026E)\ e^{\beta}$
V_{so}	7.0	-	7.33-0.029E
r_{so}	0.75	-	1.07
a_{so}	0.5	-	0.66
R_C	1.3	1.15	1.3

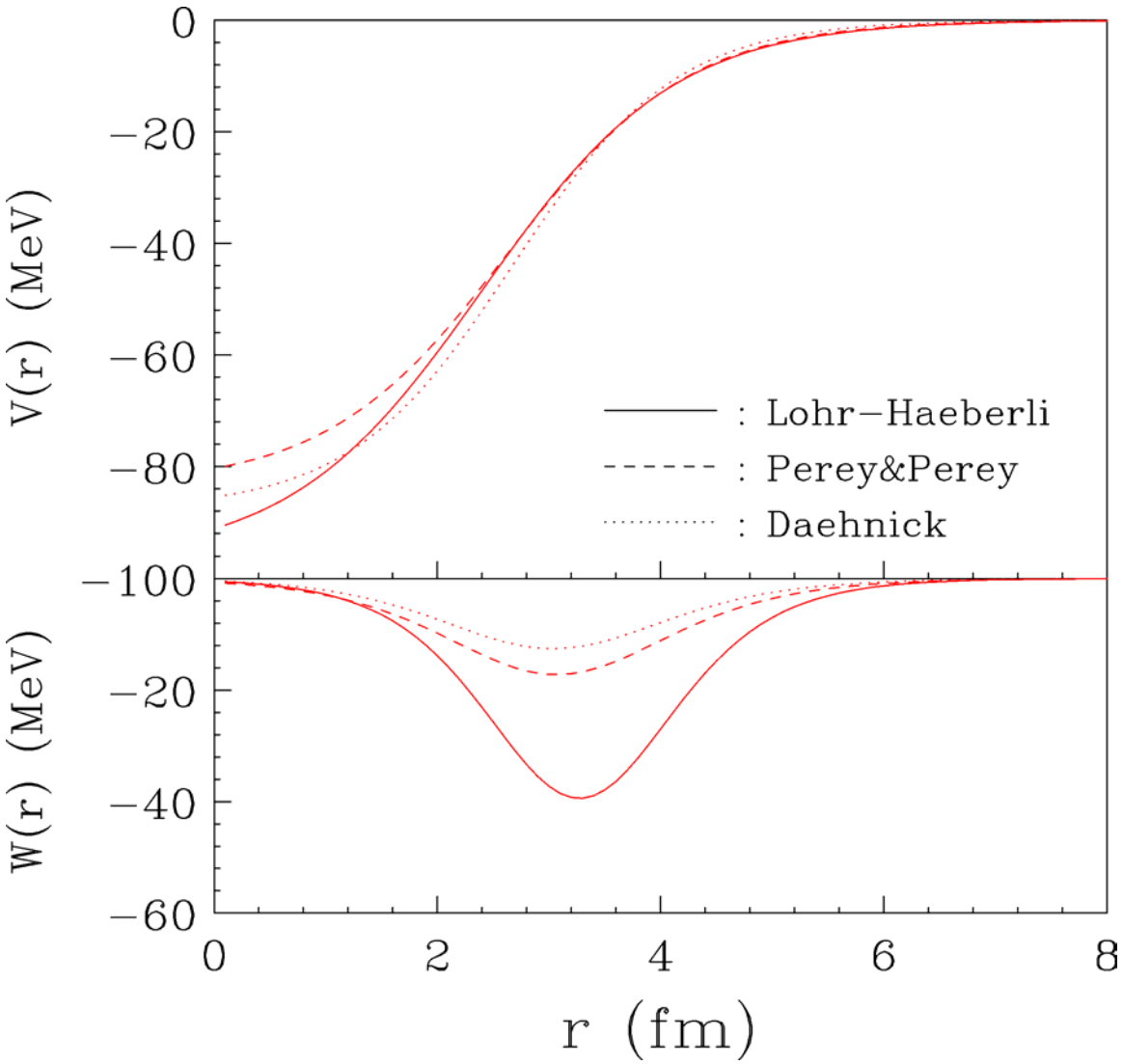

Figure 2.6: Deuteron global optical-model potentials of ^{12}C at incident deuteron energy of 11.8 MeV.

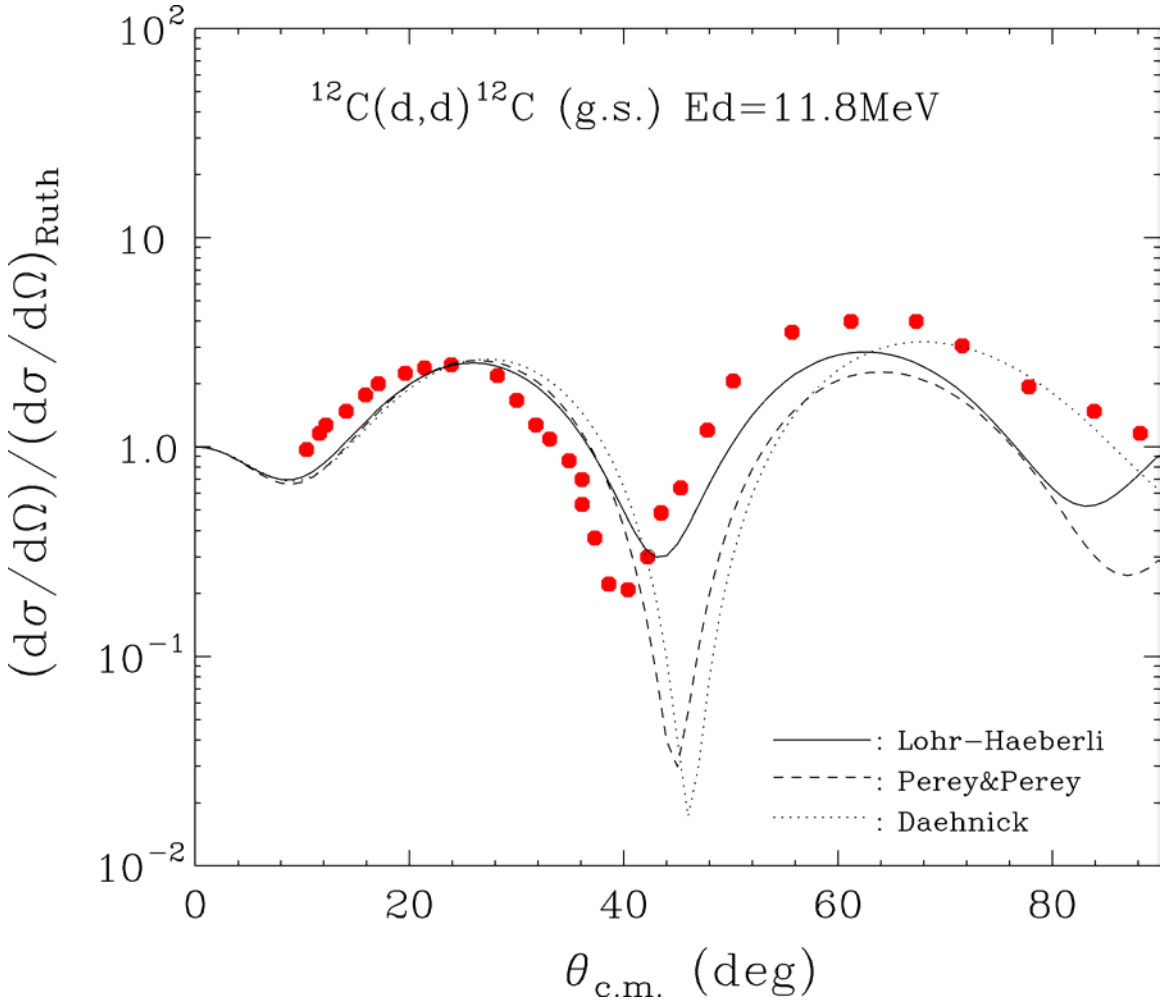

Figure 2.7: Calculations by different global optical-model potentials for the reaction of ^{12}C(d, d)^{12}C (g.s.) at incident energy of 11.8 MeV compared with the data [Fit67].

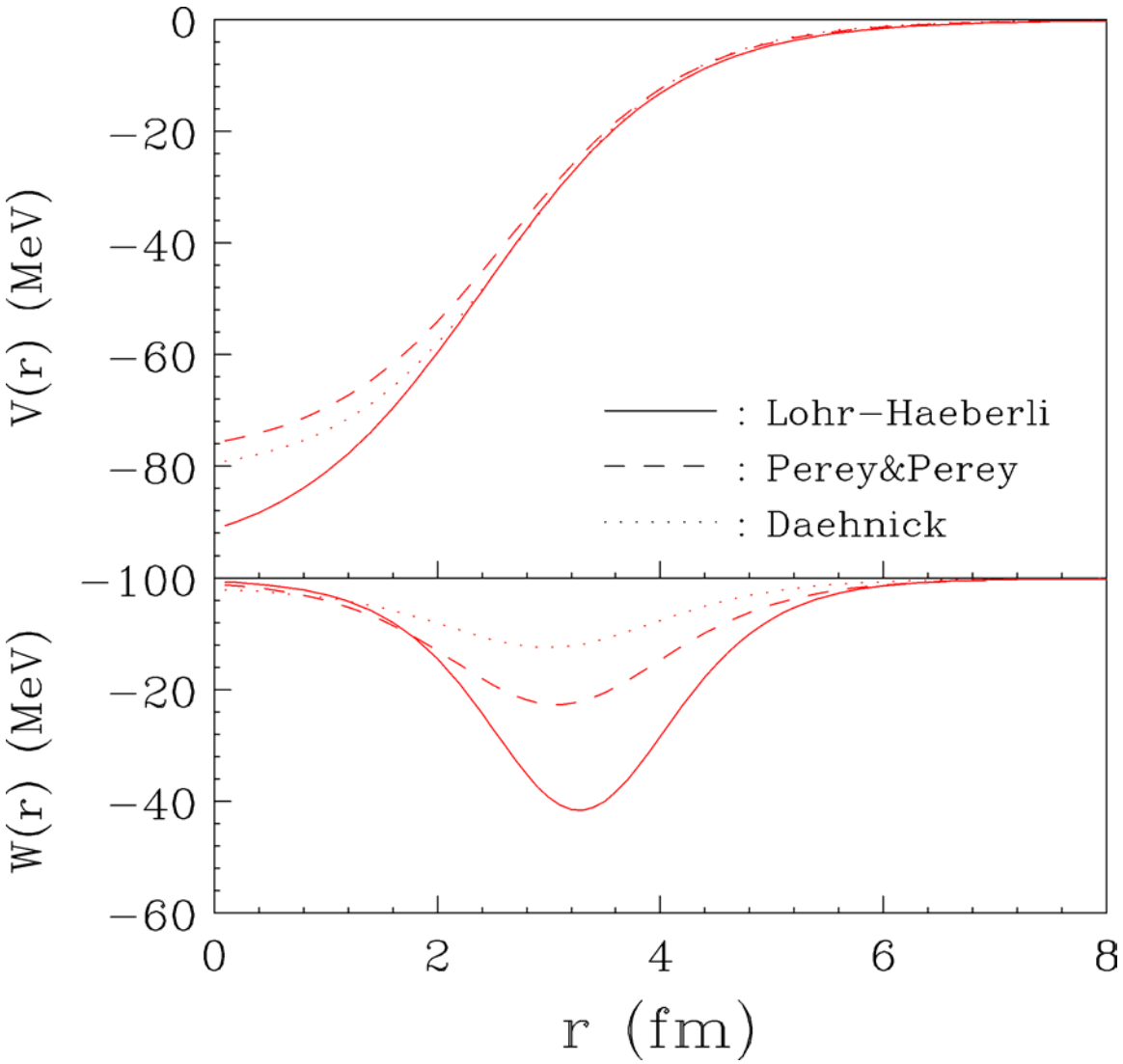

Figure 2.8: Deuteron global optical-model potentials of ^{12}C at incident deuteron energy of 34.4 MeV.

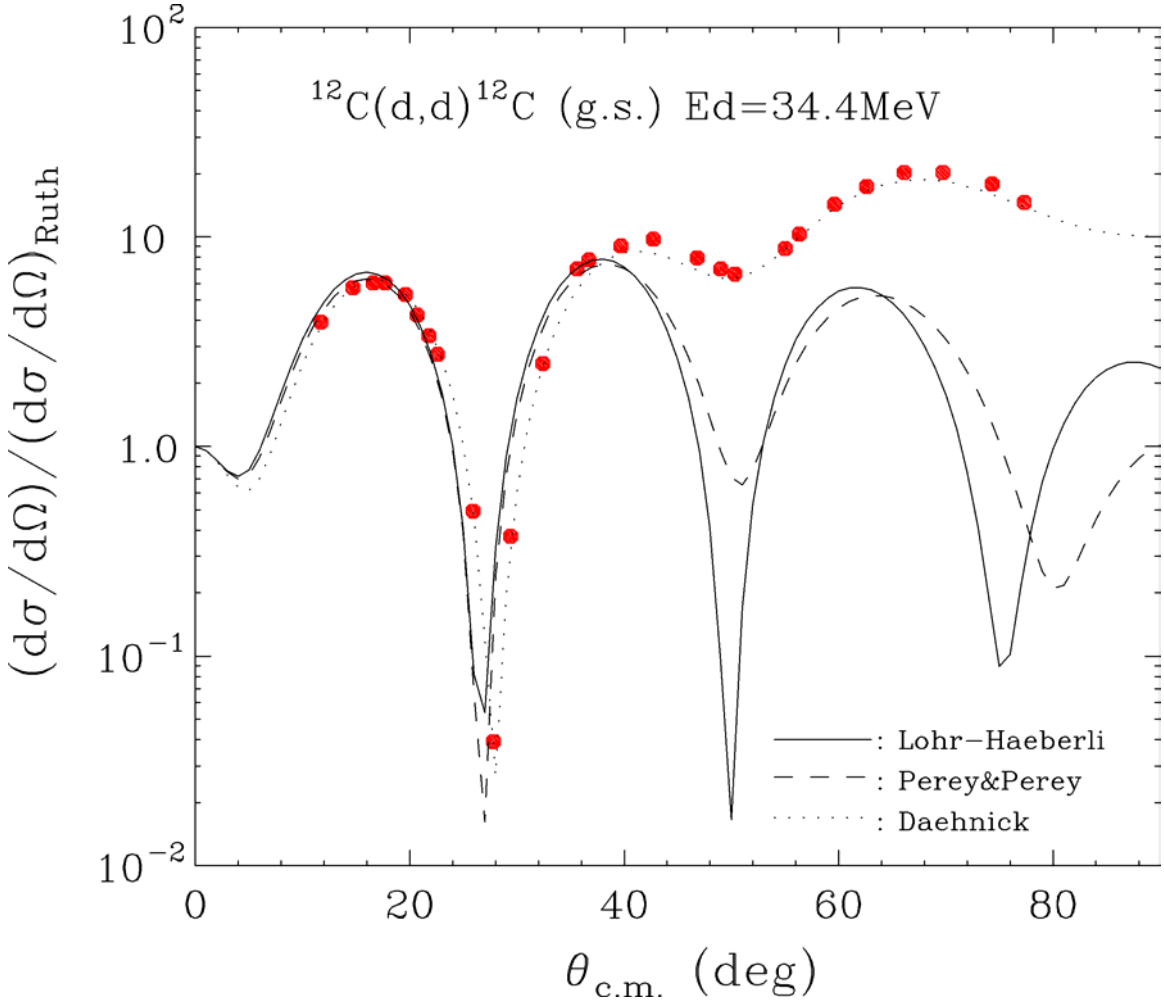

Figure 2.9: Calculations by different global optical-model potentials for the reaction of ^{12}C(d, d)^{12}C (g.s.) at incident energy of 34.4 MeV compared with the data [New67].

2.3.1.1.5 Nucleon-Nucleus Optical-Model Potential

The global optical-model potentials discussed above are derived from the fitting to the elastic scattering data in particular mass and energy regions. One consequence is that the derived global optical-model potentials cannot cover all the nuclei over a wide energy region. Thus, derivation of an optical-model potential using a much more extensive database of elastic scattering than previously used is desirable. A parameterization of the nucleon-nucleus optical-model potential based on data for A from 40 to 209, proton energies from 16 to 65 MeV and neutron energies from 10 to 26 MeV, was developed by R. L. Varner et. al. [Var91]. This parameterization, which is called Chapel-Hill 89 (CH89), is based on the current understanding of the basis of the optical potential, such as the folding model and nuclear matter approaches instead of the determination of optical-model potentials phenomenologically. The extensive database includes nearly 300 angular distributions (9000 data points) of proton and neutron differential cross sections and analyzing powers, which is significantly more accurate and complete than previous analyses [Per76, Men71, Bec69].

This parameterization adapts the basic Woods-Saxon form of Equation 2.3.10 but some parameters have slight modifications. One special feature of the parameterization of CH89 is that, based on the parameterization of nuclear charge radii [Mye73], offset values are added to the conventional radius parameters:

$$R_v = r_v A^{1/3} + r_v^{(0)}, \qquad R_w = r_w A^{1/3} + r_w^{(0)}$$

$$R_{so} = r_{so} A^{1/3} + r_{so}^{(0)}, \qquad R_c = r_c A^{1/3} + r_c^{(0)} \tag{2.3.14}$$

where $r_v^{(0)}$, $r_{so}^{(0)}$, $r_w^{(0)}$, and $r_c^{(0)}$ are offset radius of the real, imaginary, spin-orbit, and Coulomb potentials. The other special feature of CH89 is that the depths of the potential have more complex dependence on the energy and proton-neutron number.

$$V_v = V_0 \pm V_t \frac{N-Z}{A} + (E - E_c)V_e \tag{2.3.15}$$

$$E_c = \begin{cases} \dfrac{6Ze^2}{5R_c}, & \textit{for proton} \\ 0, & \textit{for neutron} \end{cases} \tag{2..3.16}$$

$$W_v = \frac{W_{v0}}{1 + \exp\left(\dfrac{W_{ve0} - (E - E_c)}{W_{vew}}\right)} \tag{2.3.17}$$

$$W_s = \frac{W_{s0} \pm W_{st} \dfrac{N-Z}{A}}{1 + \exp\left(\dfrac{(E - E_c) - W_{se0}}{W_{sew}}\right)} \tag{2.3.18}$$

where '+' is used for protons and '–' for neutrons. The parameters used in potential CH89 are listed in Table 2.4.

Figure 2.10 shows the shapes of CH89 proton potentials on ^{13}C at incident energy of 12.5 MeV. The global potentials of Menet and Perey & Perey are plotted together for the convenience of comparison. Figure 2.11 shows the calculations for proton elastic scattering on ^{13}C at incident energy of 12.5 MeV using the potentials of Menet, Perey & Perey, and CH89. The potential CH89 gives better fitting to the data.

Figure 2.12 shows the shapes of proton potentials on ^{13}C for CH89, Menet, and Perey & Perey at incident energy of 30.95 MeV. The surface regions of the real parts are close to each other. Figure 2.13 shows the calculations for proton elastic scattering on ^{13}C at

incident energy of 30.95 MeV employing the potentials of Menet, Perey & Perey, and CH89. It is obvious that the potential CH89 gives better fitting to the data. Based on the above comparisons, we adopt the potential of CH89 in our calculation in a wide energy region.

Table 2.4: Parameters for the global nucleon-nucleus optical-model potential of CH89 [Var91]

Parameters	Value	Parameters	Value
V_0	52.9 MeV	a_{so}	0.63 fm
V_t	13.1 MeV	W_{v0}	7.8 MeV
V_e	-0.299	W_{ve0}	35 MeV
r_v	1.250 fm	W_{vew}	16 MeV
$r_v^{(0)}$	-0.225 fm	W_{s0}	10.0 MeV
a_v	0.690 fm	W_{st}	18 MeV
r_c	1.24 fm	W_{se0}	36 MeV
$r_c^{(0)}$	0.12 fm	W_{sew}	37 MeV
V_{so}	5.9 MeV·fm^2	r_w	1.33 fm
r_{so}	1.34 fm	$r_w^{(0)}$	-0.42 fm
$r_{so}^{(0)}$	-1.2 fm	a_w	0.69 fm

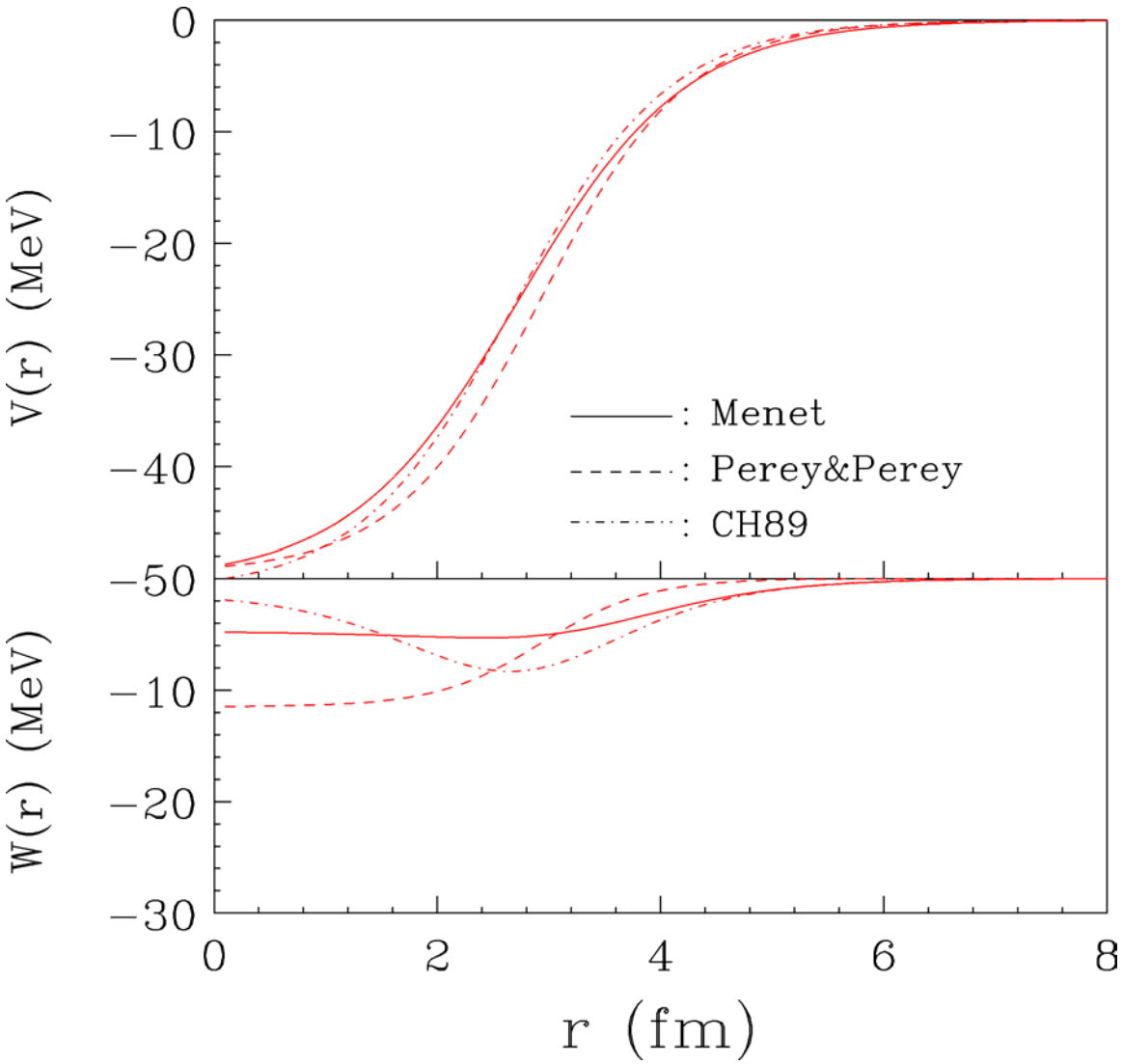

Figure 2.10: Comparison of the CH89 proton potentials of ^{13}C with the proton potentials of Menet and Perey & Perey at incident energy of 12.5 MeV.

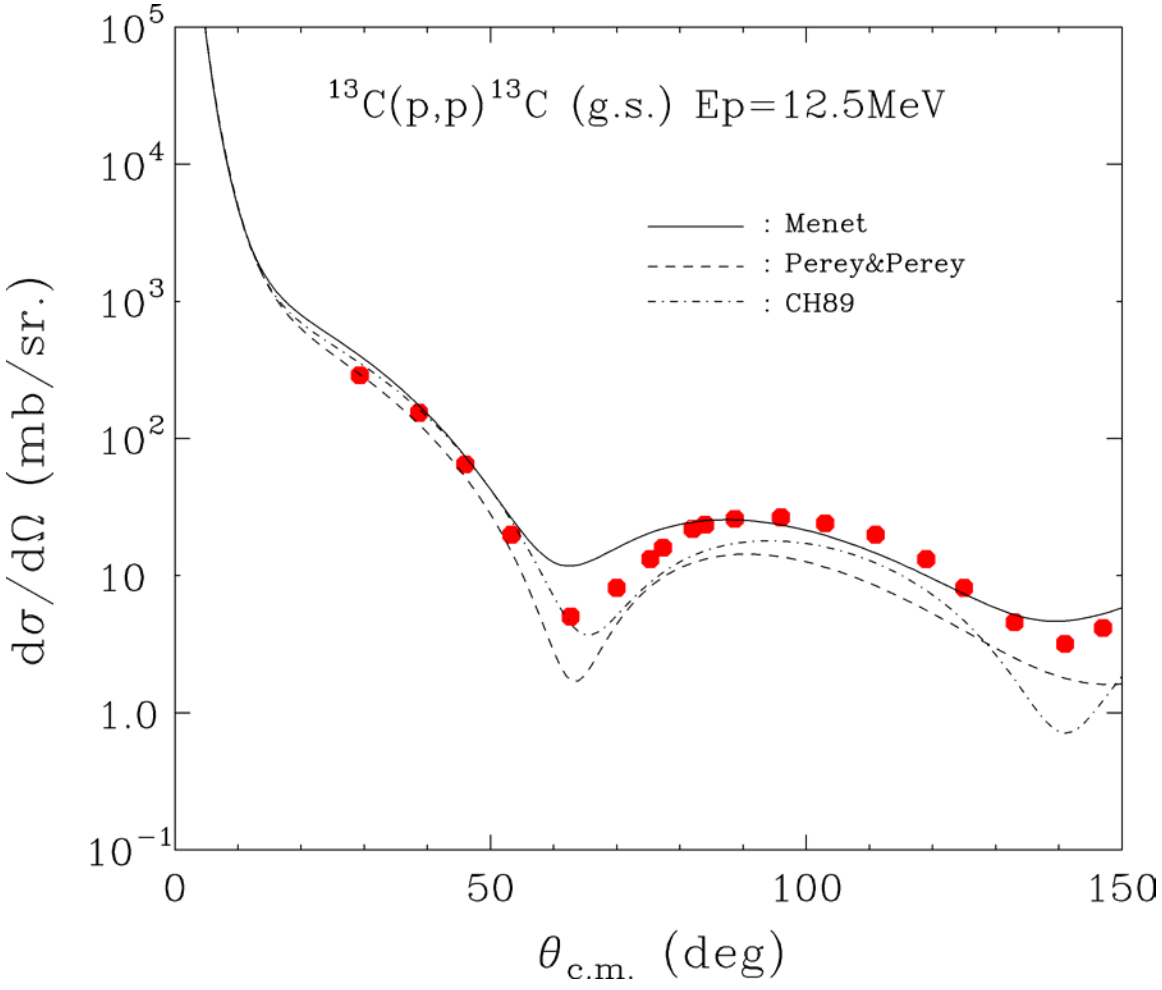

Figure 2.11: Calculations for proton elastic scattering on ^{13}C at incident energy of 12.5 MeV using the potentials of Menet, Perey & Perey, and CH89 compared with the data [Wel78].

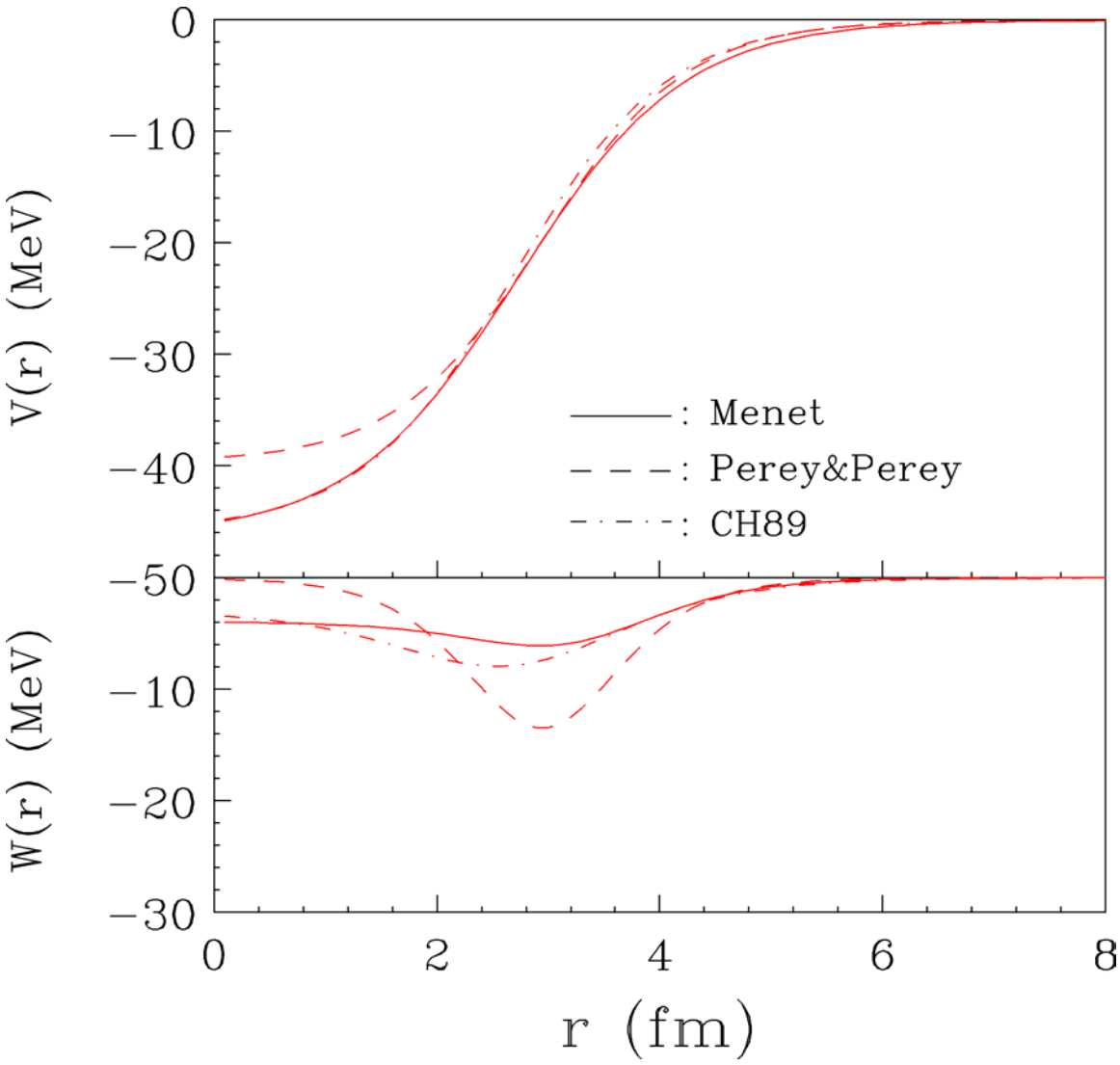

Figure 2.12: Comparison of the CH89 proton potentials of ^{13}C with the proton potentials of Menet and Perey & Perey at incident energy of 30.95 MeV.

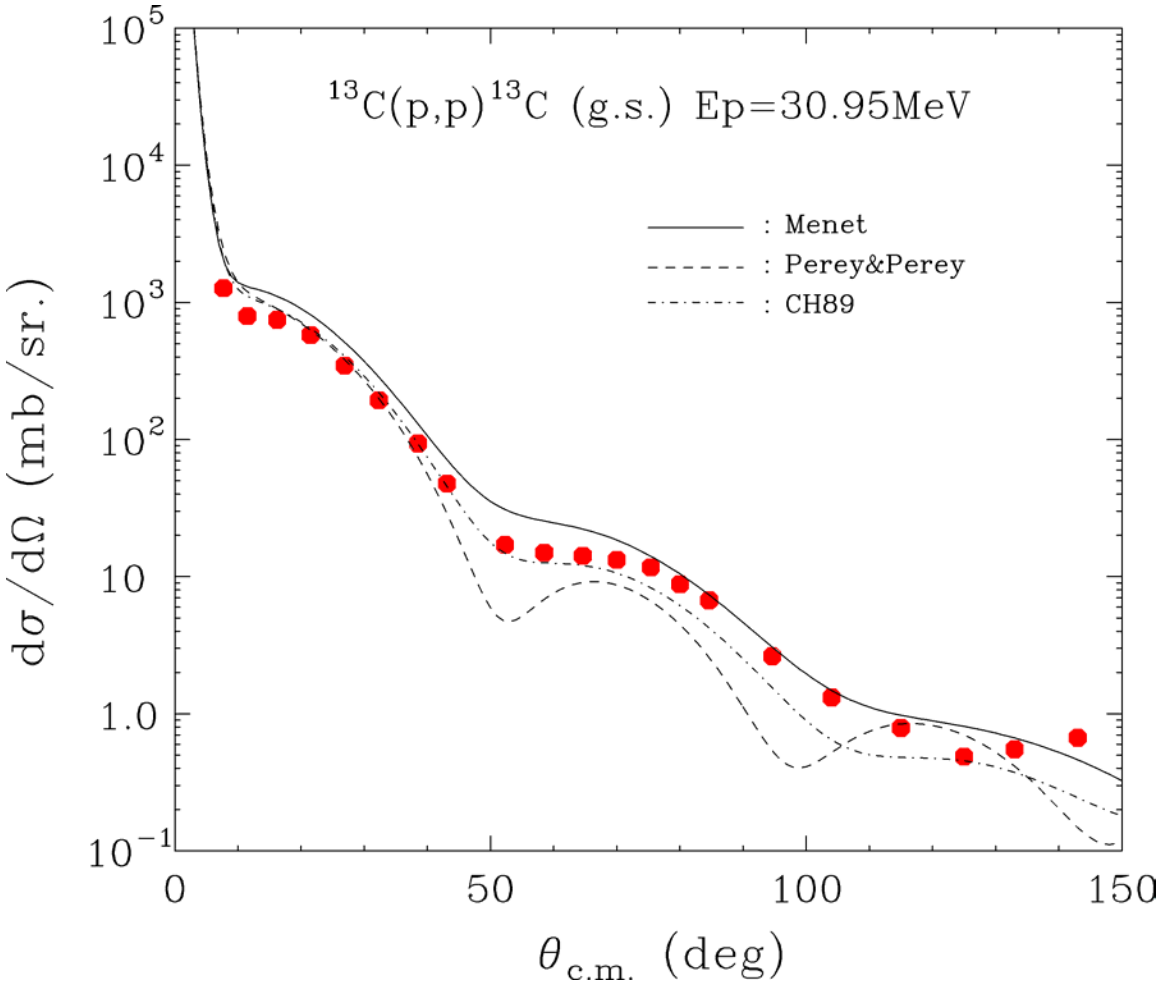

Figure 2.13: Calculations for proton elastic scattering on ^{13}C at incident energy of 30.95 MeV using the potentials of Menet, Perey & Perey, and CH89 compared with the data [Bar88].

2.3.1.1.6 JLM Optical-Model Potential

Instead of fitting elastic scattering data phenomenologically, the optical-model potential could be determined from nuclear matter theory, which may supply more microscopic understanding of the nuclear interior and overcome the uncertainties of the geometry parameters in the global optical-model potentials described previously. One such optical-model potential developed via realistic nucleon-nucleon interaction and nuclear matter density is the JLM (the initials of the three authors: Jeukenne, Lejeune, and Mahaux) potential [Jeu77].

The JLM potential started from the Brueckner-Hartree-Fock approximation and Reid's hard core nucleon-nucleon interaction, which was folded with the nuclear matter density. The complex optical-model potential in infinite nuclear matter is parameterized for nuclei with mass numbers $12 \le A \le 208$ and for energies E up to 160 MeV. For the nucleus whose nuclear matter densities are available experimentally, the JLM potentials may model the shape of the optical potentials more accurately than the phenomenological ones.

The real and imaginary JLM potentials are expressed as:

$$\overline{V}_E(r) = \lambda_v \cdot (b\sqrt{\pi})^{-3} \frac{V_E(r)}{\rho(r)} \int \rho(r') \exp\left(-\frac{|\vec{r}-\vec{r}'|^2}{b^2}\right) d^3r'$$

$$\overline{W}_E(r) = \lambda_w \cdot (b\sqrt{\pi})^{-3} \frac{W_E(r)}{\rho(r)} \int \rho(r') \exp\left(-\frac{|\vec{r}-\vec{r}'|^2}{b^2}\right) d^3r' \qquad (2.3.19)$$

where b = 1.2 fm, corresponding to the range of effective interaction [Gil71]; the scaling factors λ_v and λ_w is 1.0 and 0.8 for the real and imaginary potentials, respectively

[Pet85]; the $V_E(r)$ and $W_E(r)$ are the real and imaginary nucleon potentials derived in the local density approximation (LDA). LDA implies that the value of the potential at each point of the nucleus is the same as in a uniform medium with the same local density. In the case of a neutron with energy E, the LDA potential in uniform nuclear matter with density ρ and neutron excess δ is given by:

$$V_n(\rho, E) = V_0(\rho, E) + \delta \cdot V_1(\rho, E)$$

$$W_n(\rho, E) = W_0(\rho, E) + \delta \cdot W_1(\rho, E) \tag{2.3.20}$$

where the neutron excess is measured by the asymmetry parameter δ

$$\delta = \frac{\rho_n - \rho_p}{\rho_n + \rho_p} \tag{2.3.21}$$

There are different models to parameterize the density distributions of protons and neutrons. One that is used in this work is the modified harmonic-oscillator model [Dej74] as defined by:

$$\rho(r) = \rho_0 \left(1 + \alpha \left(\frac{r}{a}\right)^2\right) \exp\left(-\left(\frac{r}{a}\right)^2\right) \tag{2.3.22}$$

The parameters a and α can be read from Ref. [Dej74]. The density ρ_0 is [Neg70]:

$$\rho_0{}^{(k)} = \frac{3k}{4\pi C_\rho{}^3 (1 + \pi^2 a_\rho{}^2 / C_\rho{}^2)} \quad , \qquad k = N \text{ or } Z \tag{2.3.23}$$

where $a_\rho = 0.54\ fm$, and

$$C_\rho = (0.978 + 0.0206 A^{1/3}) A^{1/3} \quad (fm) \tag{2.3.24}$$

The quantity $V_0(\rho, E)$ is parameterized to

$$V_0(\rho,E)=\sum_{i,j=1}^{3}a_{ij}\rho^i E^{j-1} \tag{2.3.25}$$

The coefficients a_{ij} are listed in Table 2.5. The parametric form of the imaginary potential $W_0(\rho,E)$ is

$$W_0(\rho,E)=\frac{\sum_{i,j=1}^{4}d_{ij}\rho^i E^{j-1}}{1+\dfrac{D}{(E-\varepsilon_F)^2}} \tag{2.3.26}$$

Where $D = 600\ MeV^2$, $\varepsilon_F(\rho)=\rho(-510.8+3222\rho-6250\rho^2)$, the coefficients d_{ij} are listed in Table 2.5. The function $V_1(\rho,E)$ and $W_1(\rho,E)$ have the forms:

$$V_1(\rho,E)=\frac{\widetilde{m}(\rho,E)}{m}\operatorname{Re}N(\rho,E)$$

$$W_1(\rho,E)=\frac{m}{\overline{m}(\rho,E)}\operatorname{Im}N(\rho,E) \tag{2.3.27}$$

where $\widetilde{m}$ adapts the form:

$$\frac{\widetilde{m}(\rho,E)}{m}=1-\sum_{i,j=1}^{3}c_{ij}\rho^i E^{j-1} \tag{2.3.28}$$

The coefficients c_{ij} are listed in Table 2.5. The $\overline{m}$ is calculated by

$$\overline{m}=\frac{m\cdot m^*}{\widetilde{m}} \tag{2.3.29}$$

where the effective mass m^* is defined as

$$\frac{m^*(\rho,E)}{m}=1-\frac{d}{dE}V_0(\rho,E) \tag{2.3.30}$$

N(ρ,E) is the auxiliary function in Brueckner-Hartree-Fock approximation [Jeu77]. The real part of N is parameterized by:

$$\mathrm{Re}\,N = \sum_{i,j=1}^{3} b_{ij}\,\rho^{i} E^{j-1} \quad (MeV) \tag{2.3.31}$$

with coefficients b_{ij} listed in Table 2.5. The imaginary part of N is parameterized by

$$\mathrm{Im}\,N(\rho,E) = \frac{\sum_{i,j=1}^{4} f_{ij}\,\rho^{i} E^{j-1}}{1+\dfrac{F}{E-\varepsilon_F}} \tag{2.3.32}$$

where F=1.0 MeV. The coefficients f_{ij} are listed in Table 2.5.

In the case of a proton with energy E in the additional presence of a Coulomb field Vc, the corresponding real and imaginary potentials are given by

$$V_p(\rho,E) = V_0(\rho,E) + \Delta_C(\rho,E) - \delta\, V_1(\rho,E-V_C)$$

$$W_p(\rho,E) = W_0(\rho,E) + W_C(\rho,E) - \delta\, W_1(\rho,E-V_C) \tag{2.3.33}$$

where

$$\Delta_C(\rho,E) = V_0(\rho,E-V_C) - V_0(\rho,E)$$

$$W_C(\rho,E) = W_0(\rho,E-V_C) - W_0(\rho,E) \tag{2.3.34}$$

Figure 2.14 shows the JLM proton potentials on ^{13}C at incident energy of 12.5 MeV. For comparison, the global potentials of Menet and CH89 are plotted in the same figure. The surface regions of the real potentials are similar to each other but the interior part of the real JLM potential is deeper.

Figure 2.15 shows the elastic scattering calculations based on the above potentials. All of these calculations are quite similar at the forward angles (less than 10°). The calculated angular distribution by the JLM potential gives good fitting up to 125°.

Figure 2.16 shows the JLM proton potentials on ^{13}C at the incident energy of 30.95 MeV together with the global potentials of Menet and CH89. Again, the surface regions of the real potentials are similar to each other but the interior part of the real JLM potential is deeper. In addition, contrary to the other potentials, the imaginary JLM potential in the nuclear interior is positive.

Figure 2.17 shows the elastic scattering calculations based on these potentials. The calculated angular distribution by the JLM potential looks similar to that by the CH89 potential. All of these potentials give quite similar results at the forward angles.

Based on the above comparison, we can see that both the JLM and CH89 potentials are better than other global optical-model potentials; the JLM is even better than CH89. The disadvantage of the JLM potential is that it requires the information of nuclear density. When the nuclear density is available, we perform calculations with both the JLM and CH89 potentials; if the nuclear density is not available, only the CH89 is used.

Table 2.5: Parameters for JLM potentials

(a) a_{ij} for $V_0(\rho,E)$

i \ j	j = 1	j = 2	j = 3
i = 1	-974	11.26	-0.0425
i = 2	7097	-125.7	0.5853
i = 3	-19530	418	-2.054

(b) d_{ij} for $W_0(\rho,E)$

i \ j	j = 1	j = 2	j = 3	j = 4
i = 1	-1483	37.18	-0.3549	0.001119
i = 2	29880	-931.8	9.591	-0.0316
i = 3	-212800	7209	-77.52	0.2611
i = 4	512500	-17960	198	-0.6753

(c) c_{ij} for $\widetilde{m}(\rho,E)$

i \ j	j = 1	j = 2	j = 3
i = 1	4.557	-0.005291	0.6108E-5
i = 2	-2.051	-0.4906	0.001812
i = 3	-65.09	3.095	-0.01190

(d) f_{ij} for ImN

i \ j	j = 1	j = 2	j = 3	j = 4
i = 1	546.1	-11.2	0.1065	-3.541E-4
i = 2	-8471	230.0	-2.439	0.008544
i = 3	51720	-1520	17.17	-0.06211
i = 4	-114000	3543	-41.69	0.1537

(e) b_{ij} for ReN

i \ j	j = 1	j = 2	j = 3
i = 1	360.1	-5.224	0.02051
i = 2	-2691	51.3	-0.247
i = 3	7733	-171.7	0.8846

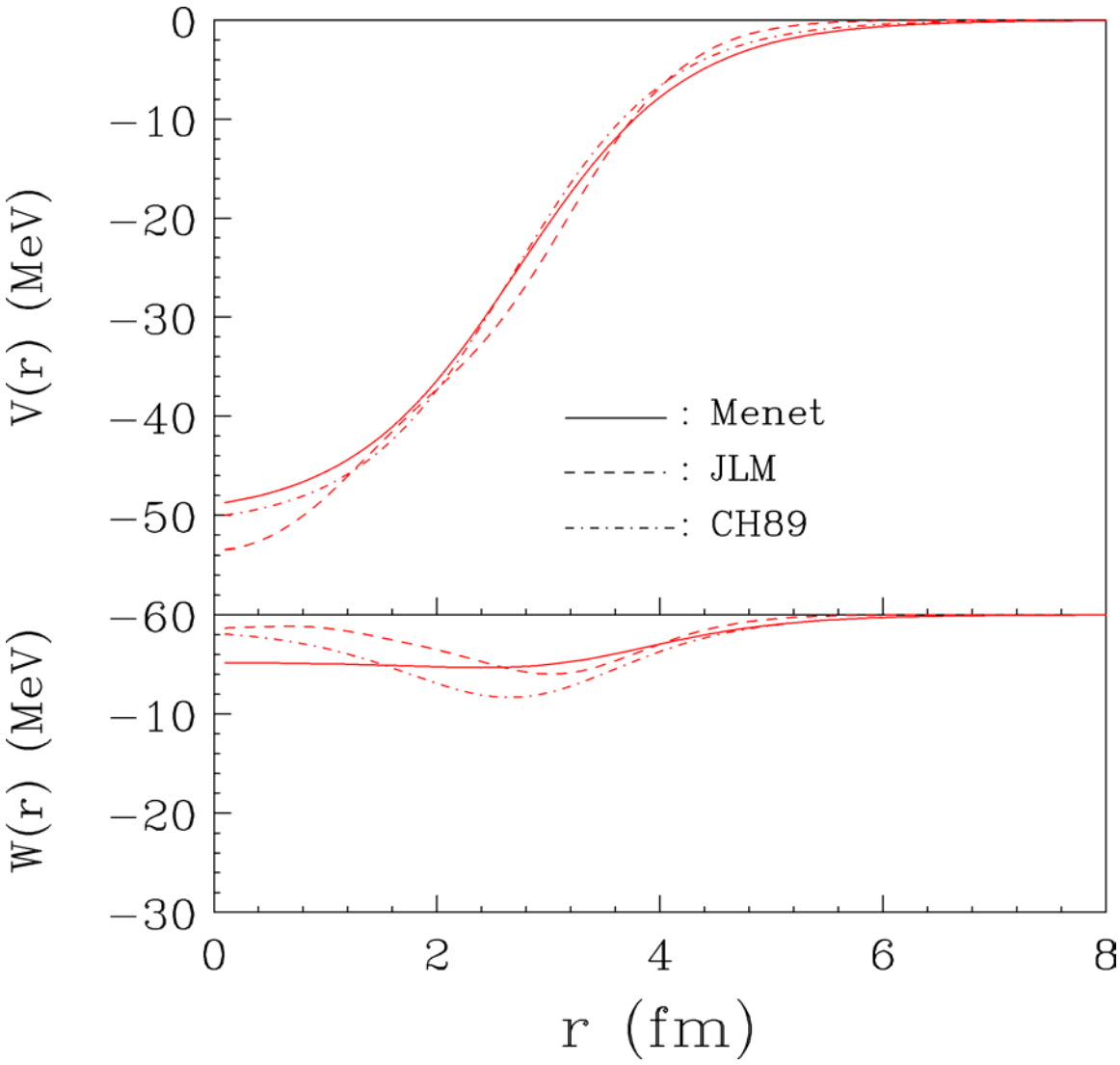

Figure 2.14: Comparison of the JLM proton potentials of ^{13}C with the proton potentials of Menet and CH89 at incident energy of 12.5 MeV.

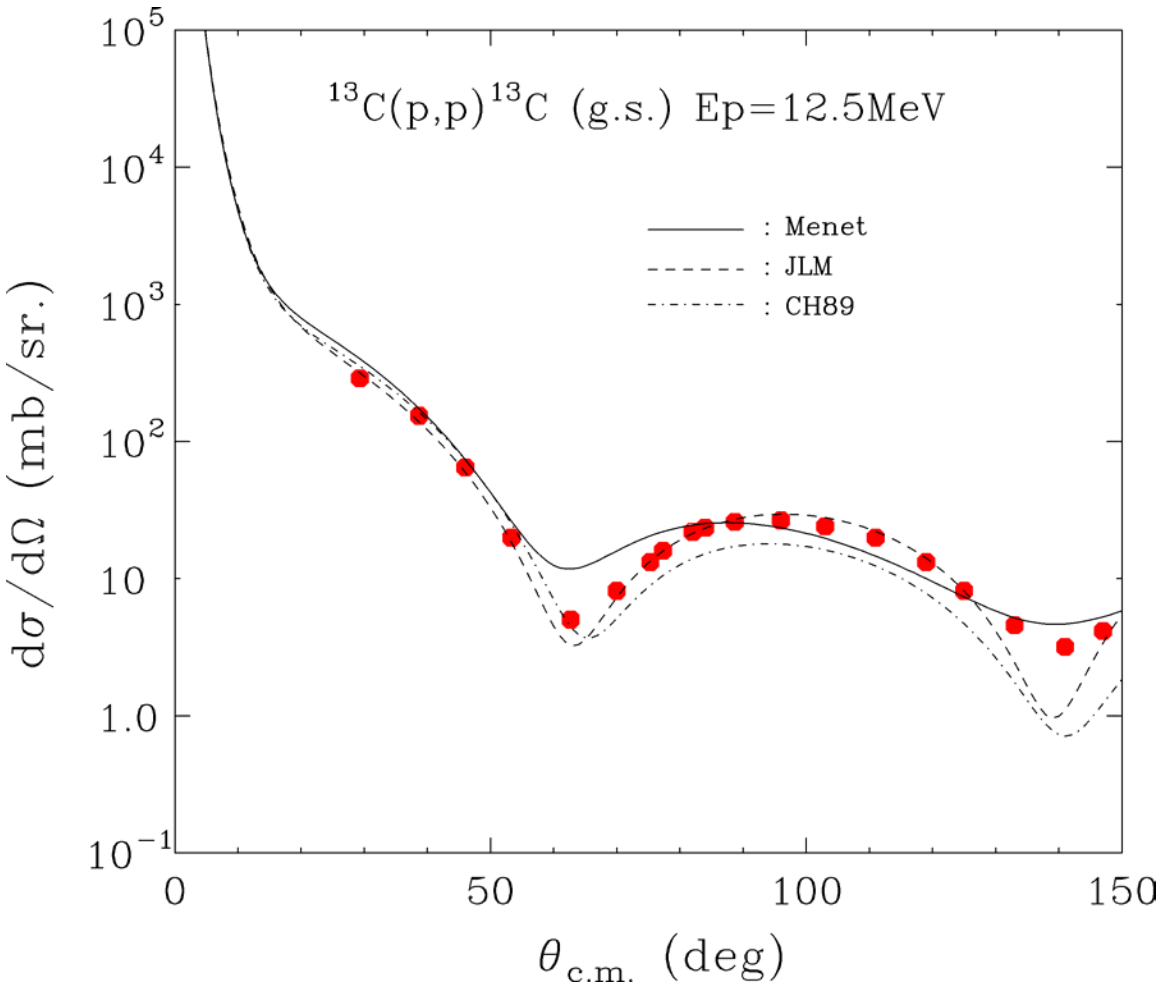

Figure 2.15: Calculations for the ^{13}C(p,p)^{13}C (g.s.) reaction by JLM, Menet and CH89 potentials at incident energy of 12.5 MeV compared with the data [Wel78].

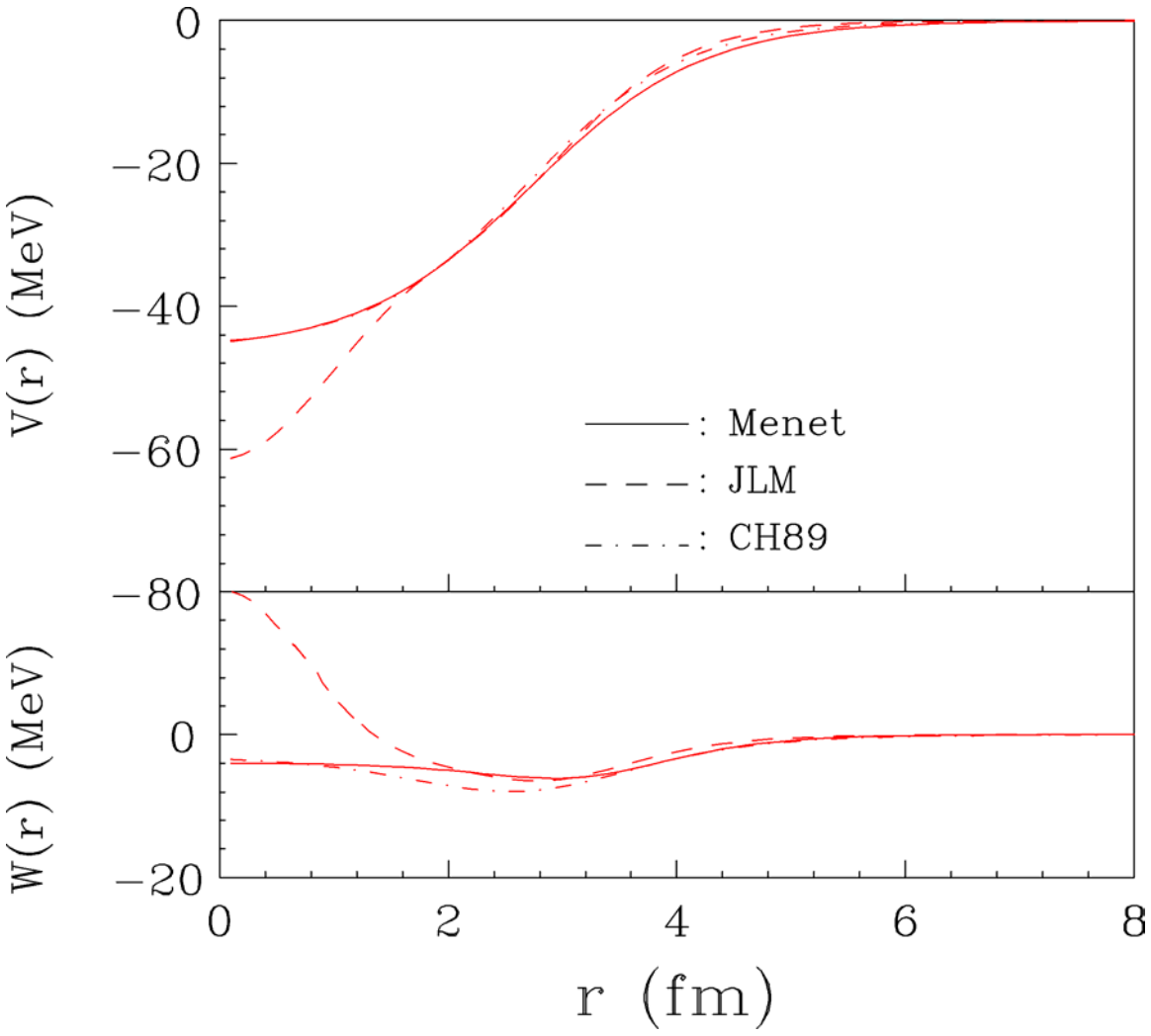

Figure 2.16: Comparison of the JLM proton potentials of ^{13}C with the proton potentials of Menet and CH89 at incident energy of 30.95 MeV.

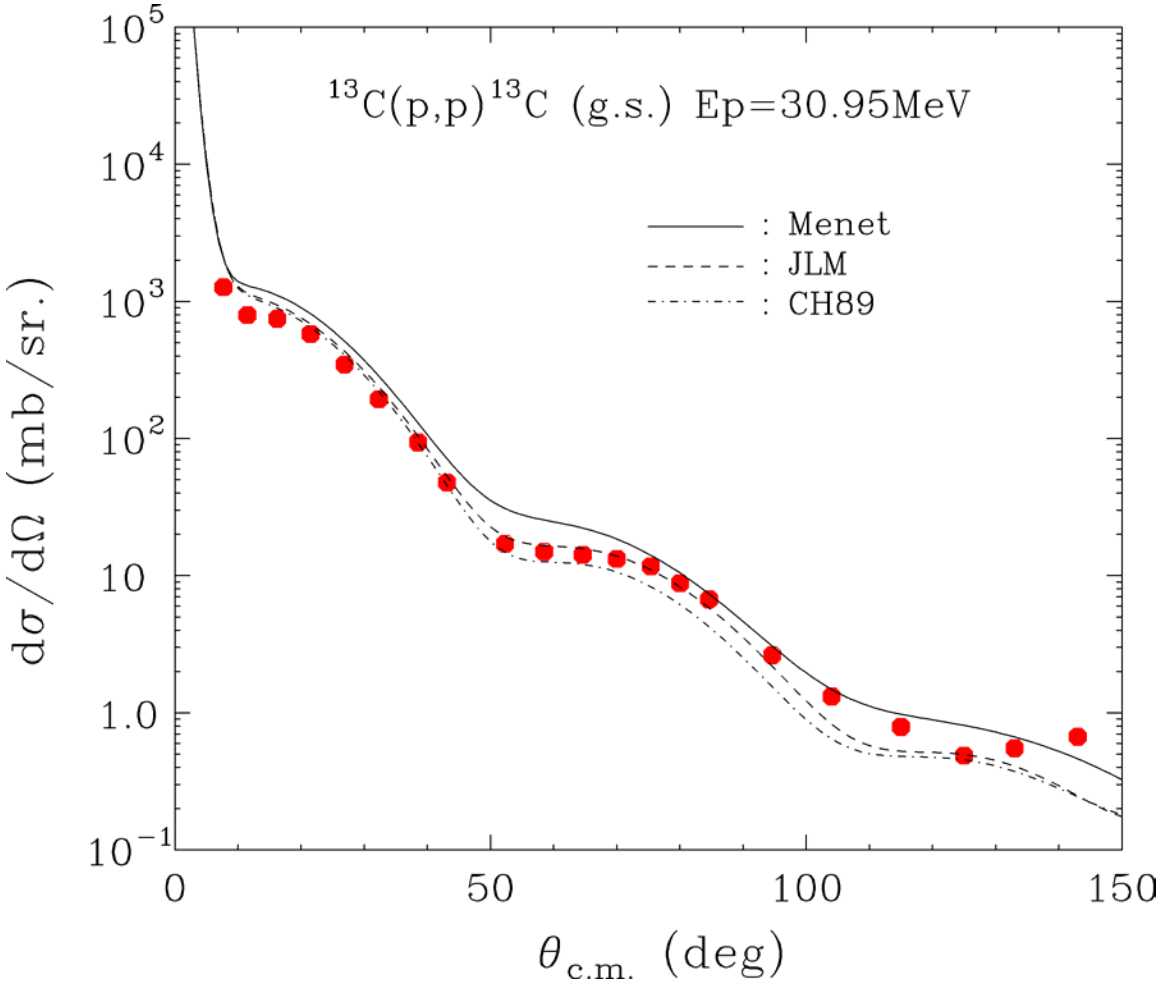

Figure 2.17: Calculations for the ^{13}C(p,p)^{13}C (g.s.) reaction by JLM, Menet and CH89 potentials at incident energy of 30.95 MeV compared with the data [Bar88].

2.3.1.2 Zero-Range Approximation

The DWBA expression for the transition amplitude in Equation 2.3.2 involves a 6-fold integration over $\vec{r}_n$ and $\vec{r}_p$ after the integration of the nuclear coordinates B. The 6-fold integration has been discussed by [Aus64] and Sawaguri [Saw67]. To simplify the integration, it is usually assumed that the transition amplitude receives contributions only from the region where the coordinates of the proton and neutron coincide so that we have the *zero-range approximation*:

$$D(\vec{r}) \equiv V_{pn}(\vec{r})\phi_d(\vec{r}) = D_0\,\delta(\vec{r}) \tag{2.3.35}$$

The value of D_0 can be obtained by integrating this equation over $\vec{r}$:

$$D_0 = \int r^2 V_{pn}(\vec{r})\phi_d(\vec{r})dr \tag{2.3.36}$$

and the vertex constant ${D_0}^2$ is [Lee64, Knu75] :

$${D_0}^2 = 15006.25\ MeV^2 \cdot fm^3 \tag{2.3.37}$$

When the zero-range approximation is made, the coordinates are transformed to:

$$\vec{r}_n \to \vec{R}\,, \qquad \vec{r}_p \to \frac{B}{B+1}\vec{r}_n \tag{2.3.38}$$

The term $B_l^{ml}(\vec{k}_p, \vec{k}_d)$ becomes

$$B_l^{ml}(\vec{k}_p, \vec{k}_d) = i^{-l}(2l+1)^{-(1/2)} D_0 \int \chi_d^{(-)*}(\vec{k}_d, \vec{R})\phi_{nl}^{ml}(\vec{R})\chi_p^{(+)}(\vec{k}_p, \frac{B}{B+1}\vec{R})\,d\vec{R} \tag{2.3.39}$$

2.3.1.3 Finite-Range Approximation

In general, deuteron has finite range of radius and the interaction between proton and neutron exists in a finite range. The zero-range approximation over-emphasizes contributions coming from the nuclear interior. A means has been found to approximate the finite-range effect so that it reduces to the form of the zero-range approximation multiplied by a radial dependent factor $\Lambda(R)$ [But64].

$$B_l^{ml}(\vec{k}_p,\vec{k}_d) = i^{-l}(2l+1)^{-(1/2)} D_0 \int \chi_d^{(-)*}(\vec{k}_d,\vec{R})\,\Lambda(R)\,\phi_{nl}^{ml}(\vec{R})\,\chi_p^{(+)}(\vec{k}_p,\frac{B}{B+1}\vec{R})\,d\vec{R} \tag{2.3.40}$$

The factor $\Lambda(R)$ is

$$\Lambda(R) = 1-(\alpha/\beta)^2(1/E_d)[U_d(R)-V_n(R)-U_p(R)-E_d] \tag{2.3.41}$$

$$\alpha = (\mu E_d/\hbar^2)^{1/2}, \qquad \mu = \frac{m_d M_B}{m_d + M_B}$$

where β is the finite range parameter with the value of 0.7457 [Knu75], E_d is the deuteron binding energy, U_d and U_p are the deuteron and proton optical potentials, and V_n is the neutron potential that binds the neutron to the core nucleus B.

Figure 2.18 shows the comparison of the DWBA calculations in this finite-range approximation (solid line) and zero-range approximation (dashed line) for the reaction of ^{13}C(p,d)^{12}C at proton energies of 15 MeV and 48.3 MeV. The calculations use CH89 as the proton potential and Daehnick global potential for the deuteron. Thus finite-range approximation increases the cross section by 4.8% at the peak region for the proton energy of 15 MeV. For incident proton energy at 48.3 MeV, the enhancement is 8.9% at

forward angles. Thus the effects, although not negligible, are not very large for the reactions that we studied.

It should be noted that results from this finite-range approximation are very close to the exact finite-range calculations with numerical solution of the deuteron wave function. The latter kind of calculation is available by another widely used finite-range DWBA code: DWUCK5 [Kunz]. Figure 2.19 shows the comparison between the calculations from two codes for the $^{13}C(p,d)^{12}C$ reaction. They are very close to each other especially at the forward angles. At proton energy of 15 MeV, the curve from TWOFNR is just 1.5% lower than that from DWUCK5 at the region of first peak. At proton energy of 48.3 MeV, the curve from TWOFNR is 2.0% higher than that from DWUCK5 at the forward angles. However, TWOFNR is more user friendly with many options to choose from.

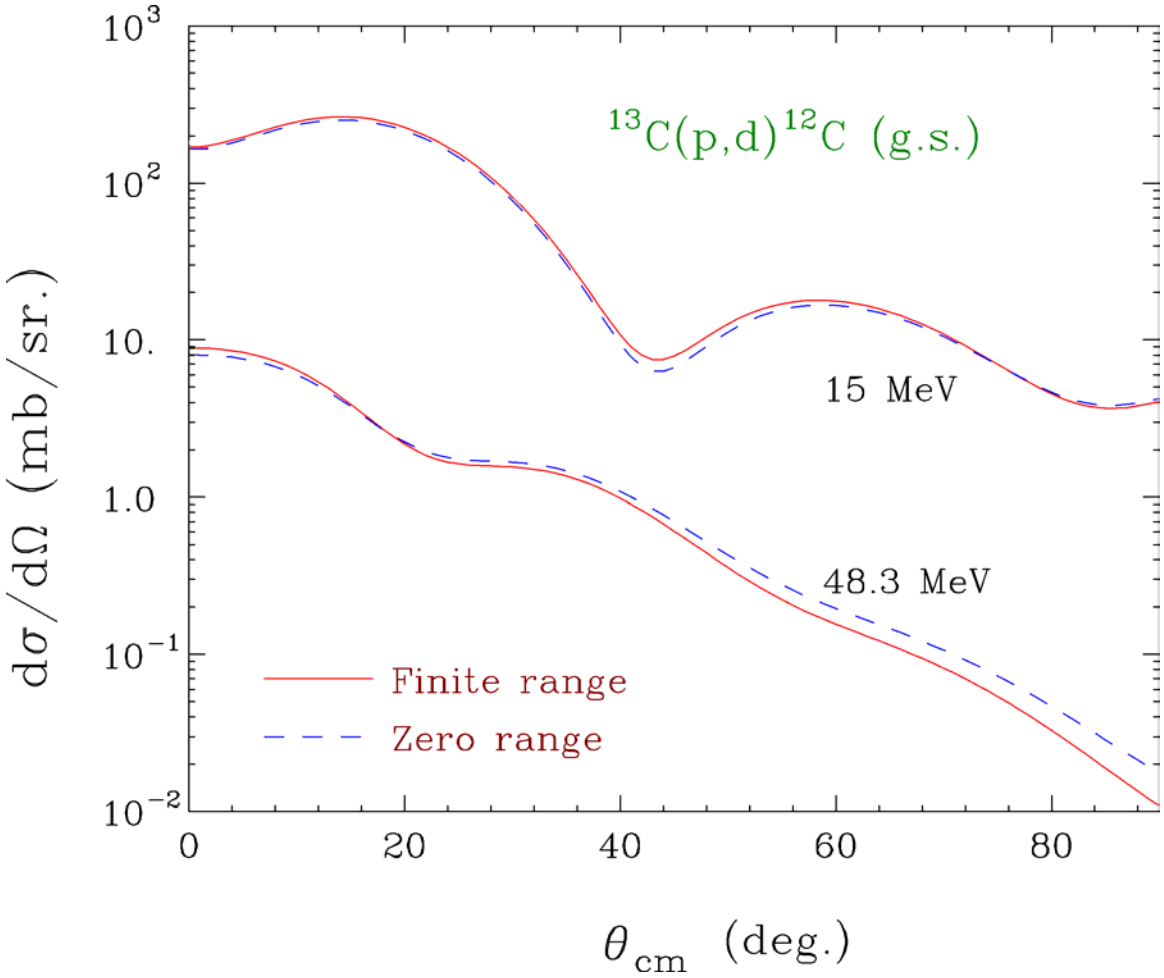

Figure 2.18: Calculations for reaction of $^{13}C(p,d)^{12}C$ (g.s.) using finite-range approximation (solid line) and zero-range approximation (dashed line) at incident energies of 15 MeV and 48.3 MeV. The cross sections at proton energy of 15 MeV have been multiplied by 10 so that the calculations at the two energies can be seen more clearly.

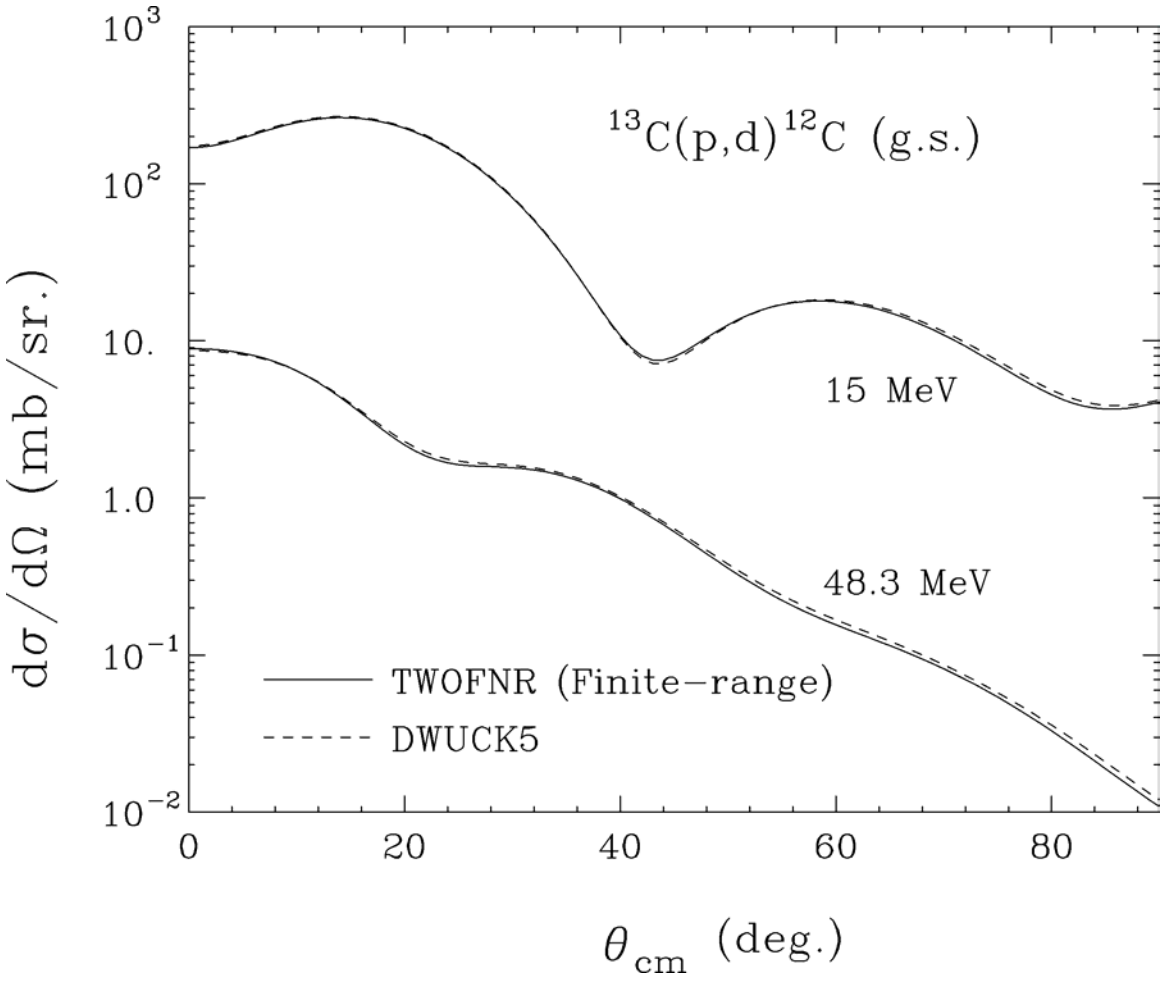

Figure 2.19: Finite-range DWBA calculations for reaction of $^{13}C(p,d)^{12}C$ (g.s.) by TWOFNR (solid line) and DWUCK5 (dashed line) at incident energies of 15 MeV and 48.3 MeV. The cross sections at proton energy of 15 MeV have been multiplied by 10.

2.3.1.4 Non-Locality Correction

The optical-model potential is usually taken to have simple local form, which means that, at the point r, the particle feels the potential only at that point. The Schrödinger equation reads

$$\left(-\frac{\hbar^2}{2\mu}\nabla^2 + U_L(\vec{r}) - E \right)\psi(\vec{r}) = 0 \tag{2.3.42}$$

The real situation is more complicated and the optical potential should be non-local, which means that the wave function at point $\vec{r}$ is affected within the range of non-local potential. $U_L(\vec{r})\psi(\vec{r})$ in Equation 2.3.42 should be replaced by

$$\int U(\vec{r},\vec{r}')\psi(\vec{r}')\,d\vec{r}' \tag{2.3.43}$$

where $U(\vec{r},\vec{r}')$ is the non-local potential. Non-locality can be expected wherever the potential is energy dependent that comes from the exchange terms required by the asymmetry of the overall wavefunction.

This effect has been studied by Perey and Buck [Per62]. They separated the non-local kernel $U(\vec{r},\vec{r}')$ into a potential form U times a Gaussian non-locality function.

$$U(\vec{r},\vec{r}') = U\left(\left|\frac{\vec{r}+\vec{r}'}{2}\right|\right)H\left(\vec{r}-\vec{r}'\right) \tag{2.3.44}$$

where $H\left(\vec{r}-\vec{r}'\right)$ was chosen to be a Gaussian function:

$$H\left(\vec{r}-\vec{r}'\right) = \frac{\exp\left(-\left((\vec{r}-\vec{r}')/\beta_{NL}\right)^2\right)}{\left(\pi^{\frac{3}{2}}\beta_{NL}^{\,3}\right)} \tag{2.3.45}$$

where β_{NL} is the range of non-locality. The value of β_{NL} that Perey and Buck found to yield the best fit to the data of neutron scattering on Pb over an energy range from 4.1 MeV to 24.0 MeV is 0.85 fm [Per62]. For the deuteron, β_{NL} is 0.54 fm [Per74].

Figure 2.20 shows the comparison between the local and non-local proton potential from CH89. The local potentials are generally weaker than the non-local potentials, $|V_L| < |V_{NL}|$ and $|W_L| < |W_{NL}|$, especially within the interior of the nuclei. Thus, non-locality reduces contributions to transfer reaction from the interior of the nucleus. The main change produced in the cross section is the reduction of the large angle scattering while increasing the forward or peak cross section [Phi68]. Figure 2.21 shows the calculations for the reaction of ^{13}C(p,d)^{12}C at incident energy of 48.3 MeV, where proton potential chooses the global potential of CH89 and the deuteron potential adapts the global potential of Daehnick [Dae80]. Finite-range approximation is employed in these calculations. The dashed line shows the result from the local proton potential; the solid line shows the result when non-locality correction is applied to the proton potential. We can see that the cross section by the non-local proton potential increases 12% at forward angles, where the spectroscopic factors are extracted. Similar effect is obtained when the non-locality correction is applied to the deuteron potential. The total effects are cumulative when the non-locality correction is applied to the proton and the deuteron simultaneously. Thus it is important to include non-locality corrections in transfer reaction calculations.

The non-locality correction at lower energy is also examined. Figure 2.22 shows the calculations for the same reaction at incident proton energy of 15 MeV. The calculations with and without non-locality correction are very close at the region of first peak.

Therefore, the extracted SF are not strongly affected by the non-locality correction at low energy.

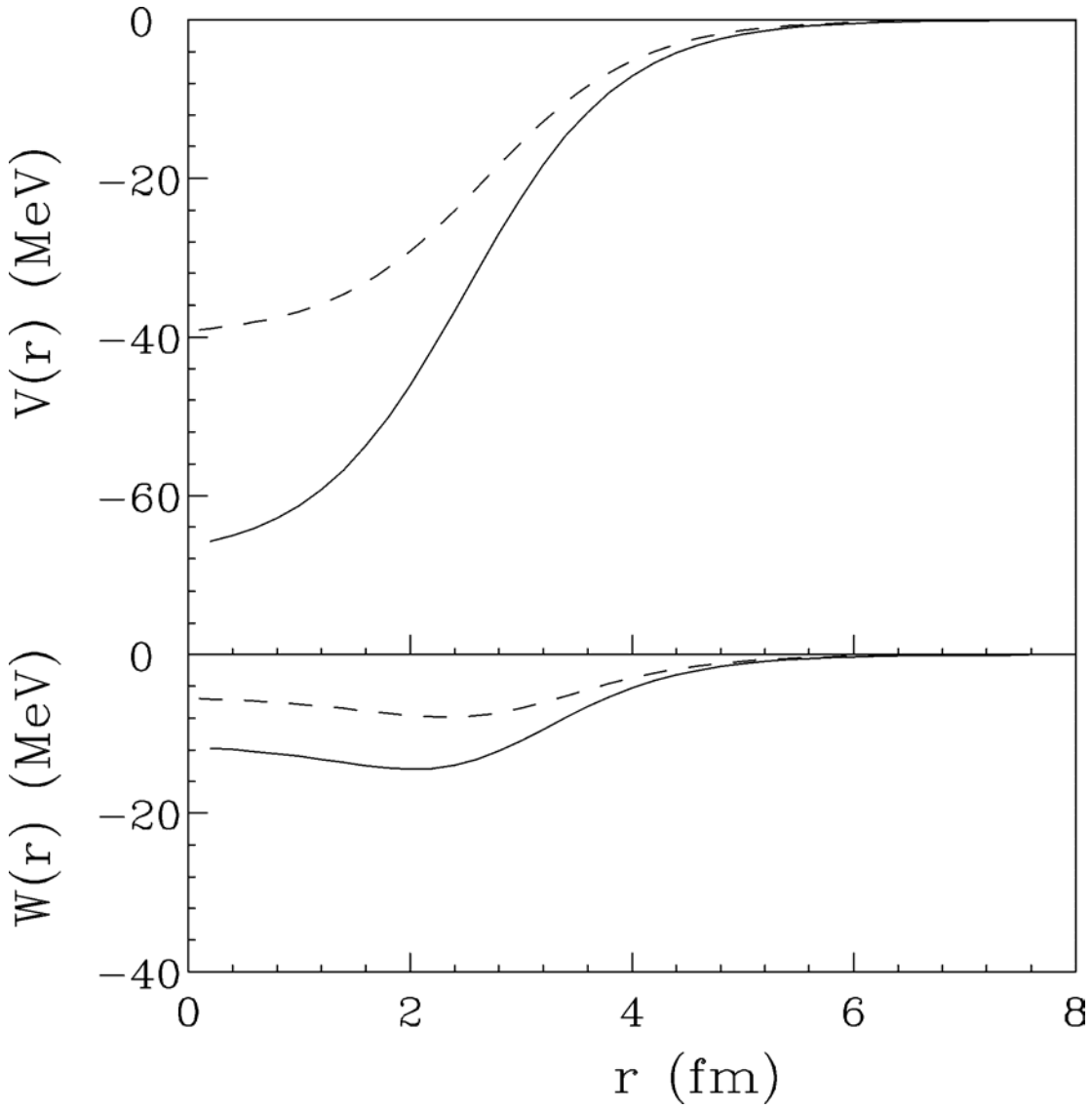

Figure 2.20: Comparison of the local (dashed line) and non-local (solid line) proton potentials (CH89) of ^{13}C at incident proton energy of 48.3 MeV.

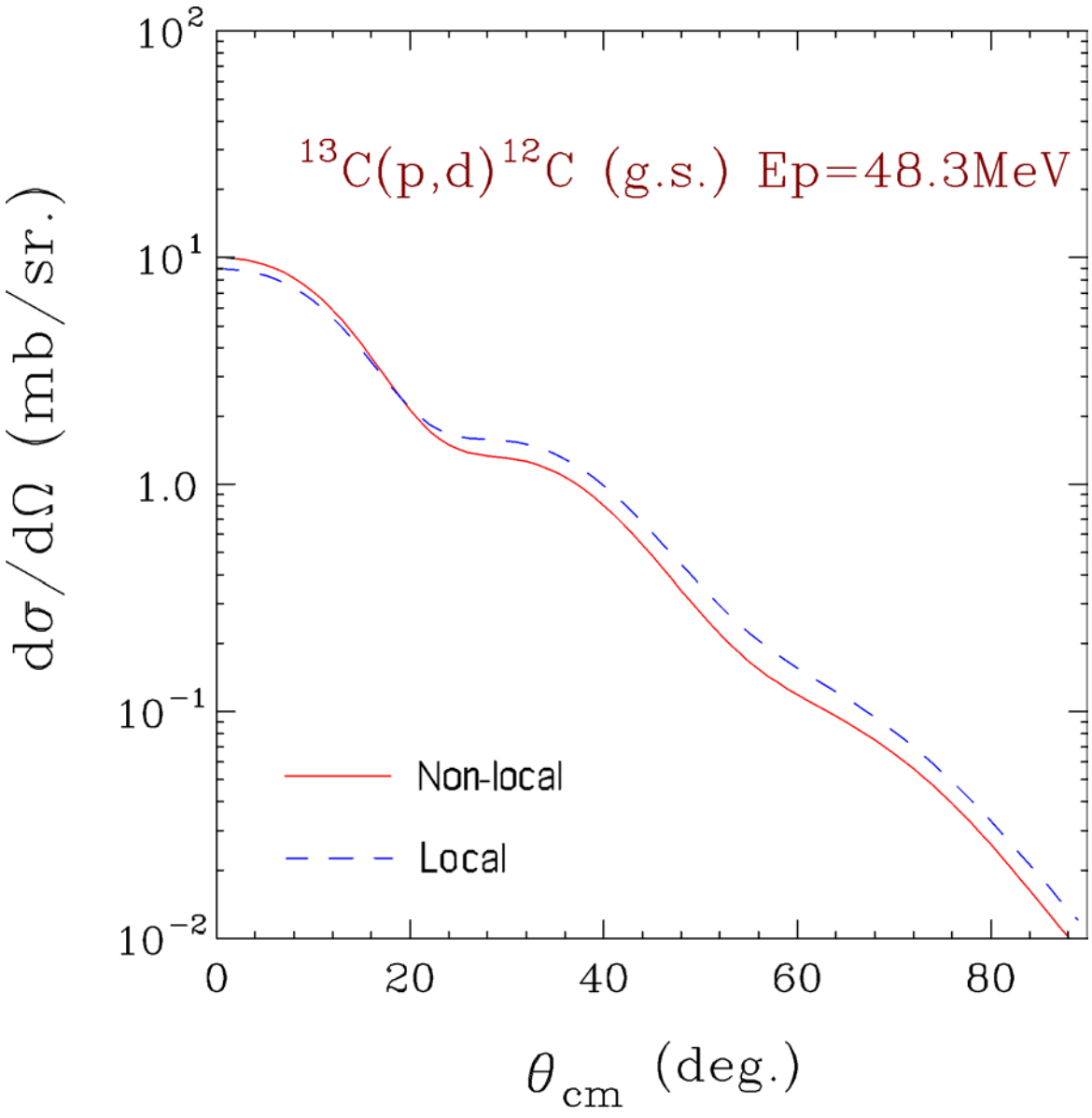

Figure 2.21: Calculated differential cross section for ^{13}C(p,d)^{12}C at incident proton energy of 48.3 MeV by non-local proton potential (solid line) increased 12% at the forward angles compared to that by local proton potential (dashed line).

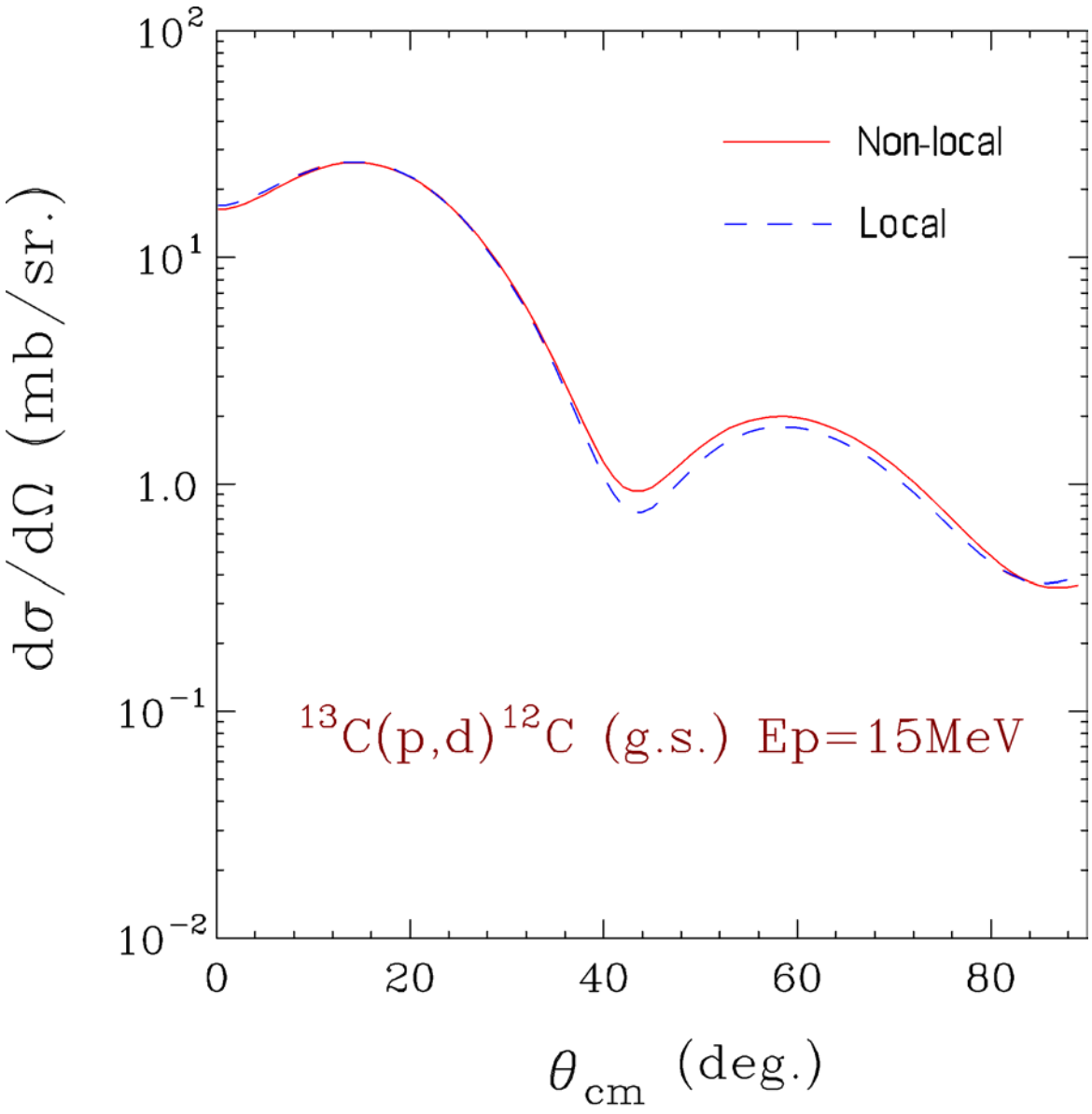

Figure 2.22: Calculated differential cross sections for ^{13}C(p,d)^{12}C at incident energy of 15 MeV using non-local proton potential (solid line) and local proton potential (dashed line).

2.3.1.5 Neutron Form Factor

In most analyses of single neutron transfer reactions, it is assumed that the neutron is picked up or deposited into a shell model single-particle state. In the standard energy separation procedure, the corresponding single-particle wave function $\phi_{nlj}(\vec{r}_n)$, called the *neutron form factor*, is usually taken to be an eigenfunction of a Woods-Saxon potential whose geometry is fixed (r_0=1.25 fm, a_0=0.65 fm, $R = r_0 \cdot A^{1/3}$ fm) and depth is adjusted so that the eigenvalue is equal to the experimental neutron separation energy [Pin65, Ber65].

Table 2.6 lists the information of the neutron form factors for the four reactions we studied in this thesis. Figure 2.23(a) shows $\phi_{nlj}(r)$ in the $1p_{1/2}$ orbit for the reaction of p(^{13}C,d)^{12}C (g.s.). The depth V_n is adjusted to be –39.779 MeV corresponding to the neutron binding energy of –4.946 MeV. The neutron form factor for the reaction of p(^{13}C,d)^{12}C (2^+, 4.439 MeV) is shown in Figure 2.23(b). In this case, the neutron orbit is $1p_{3/2}$ and the neutron separation energy is –9.385 MeV. Similarly, Figure 2.6 (c) and (d) show the neutron form factors for the reaction of p(^{11}B,d)^{10}B (g.s.) and p(^{10}Be,d)^{9}Be (g.s.), separately. The well-depths and the binding energies are listed in Table 2.6

It is important to examine the sensitivity of the calculations to the parameters r_0 and a_0 of neutron potential. Figure 2.24 shows the dependence on the neutron radius parameter for the reaction of ^{13}C(p,d)^{12}C (g.s.) at proton energies of 15 MeV and 48.3 MeV. CH89 and Daehnick potentials are used for proton and deuteron respectively. (Finite-range approximation and non-locality correction are employed in all following

calculations). The neutron radius parameter r_0 is changed from 1.2 fm to 1.3 fm while the spin-orbit strength is fixed to zero and the neutron diffuseness is fixed to 0.65 fm. The change of 0.1 fm (corresponding to 8% change) changes the cross sections at forward angles by 16% at higher incident energy and 11% at lower incident energy. Figure 2.25 shows the dependence on the neutron diffuseness parameter, where the neutron diffuseness changes from 0.6 fm to 0.7 fm with the r_0 fixed to 1.25 fm and V_{so} fixed to zero. The increase of 0.1 fm (corresponding to 16% change) in the neutron diffuseness increases the cross sections at forward angles 20% at higher energy and 17% at lower incident energy.

Figure 2.26 shows the dependence on the spin-orbit strength. When the spin-orbit strength of the neutron potential changes from 0.0 MeV to 6.0 MeV, the cross sections at forward angles decrease by 6-8%. Since this effect is small, the spin-orbit strength is set to zero in all of the following analyses.

Table 2.6 The neutron potentials and the binding energies of the neutron form factors in the reactions of this experiment

Reaction	Neutron orbit	Binding energy (MeV)	V_n (MeV)	r_0 (fm)	a_0 (fm)
p(^{13}C,d)^{12}C g.s.	$1p_{1/2}$	-4.946	-39.779	1.25	0.65
p(^{13}C,d)^{12}C 2^+	$1p_{3/2}$	-9.385	-48.257	1.25	0.65
p(^{11}B,d)^{10}B g.s.	$1p_{3/2}$	-11.455	-56.853	1.25	0.65
p(^{10}Be,d)^{9}Be g.s.	$1p_{3/2}$	-6.811	-50.905	1.25	0.65

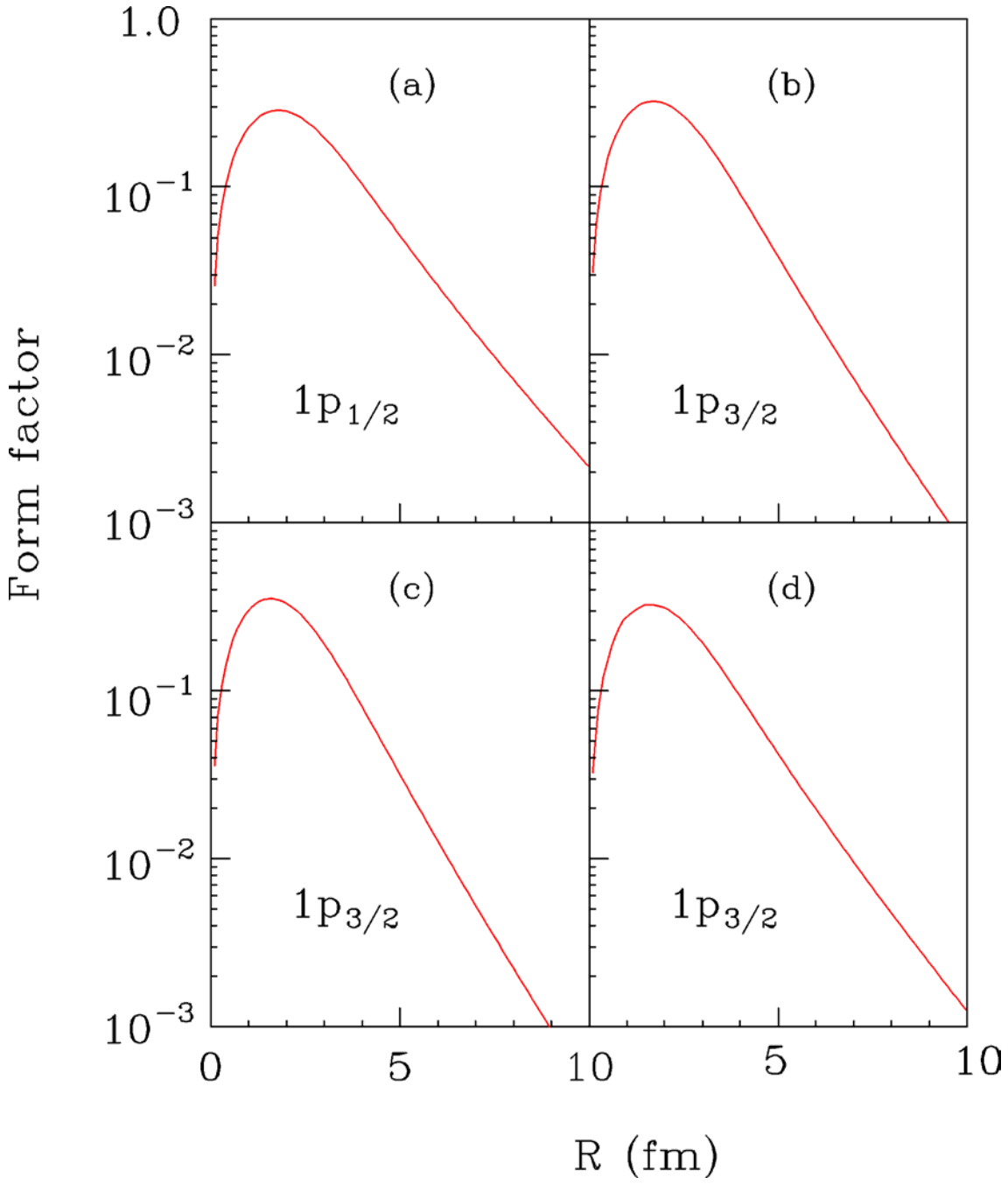

Figure 2.23: Neutron form factors for the reactions of (a) p(^{13}C,d)^{12}C (g.s.), (b) p(^{13}C,d)^{12}C (2^+), (c) p(^{11}B,d)^{10}B (g.s.), and (d) p(^{10}Be,d)^{9}Be (g.s.).

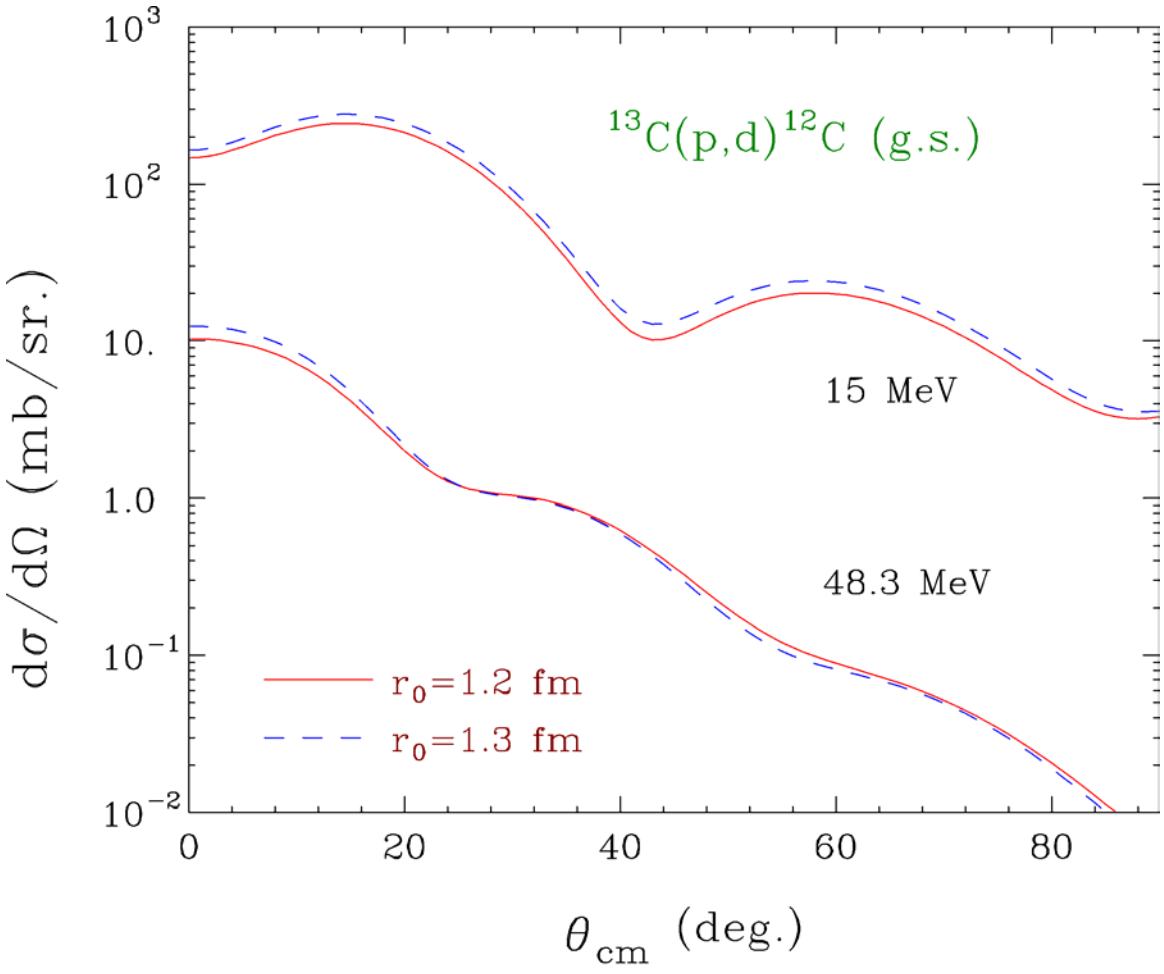

Figure 2.24: Calculations on the variation of neutron radius parameter r_0, where the neutron diffuseness a_0 is fixed to 0.65 fm and the spin-orbit strength V_{so} is 0.0 MeV. The cross sections at proton energy of 15 MeV are multiplied by 10.

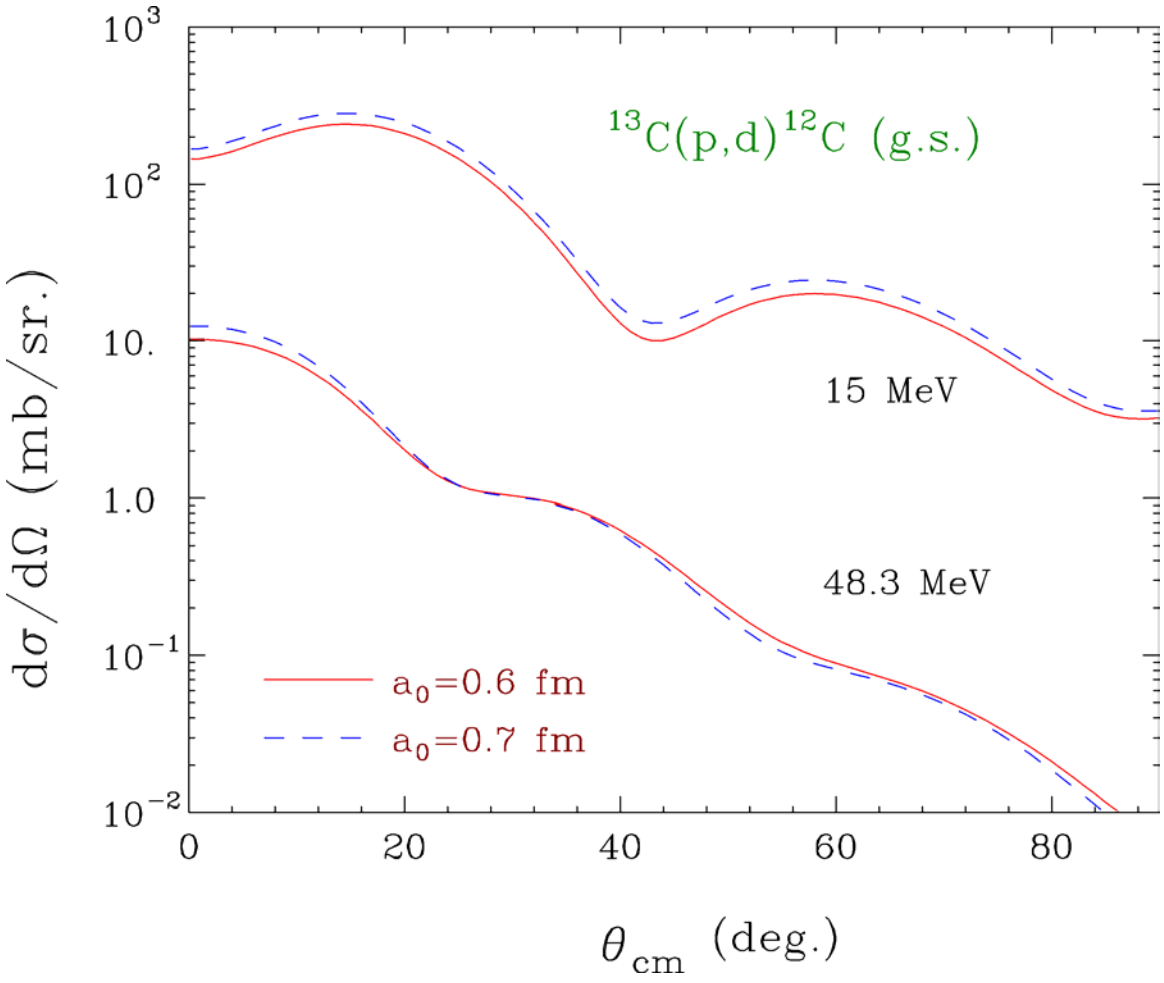

Figure 2.25: Calculations on the variation of neutron diffuseness a_0, where the neutron radius parameter r_0 is fixed to 1.25 fm and the spin-orbit strength V_{so} is 0.0 MeV. The cross sections at proton energy of 15 MeV are multiplied by 10.

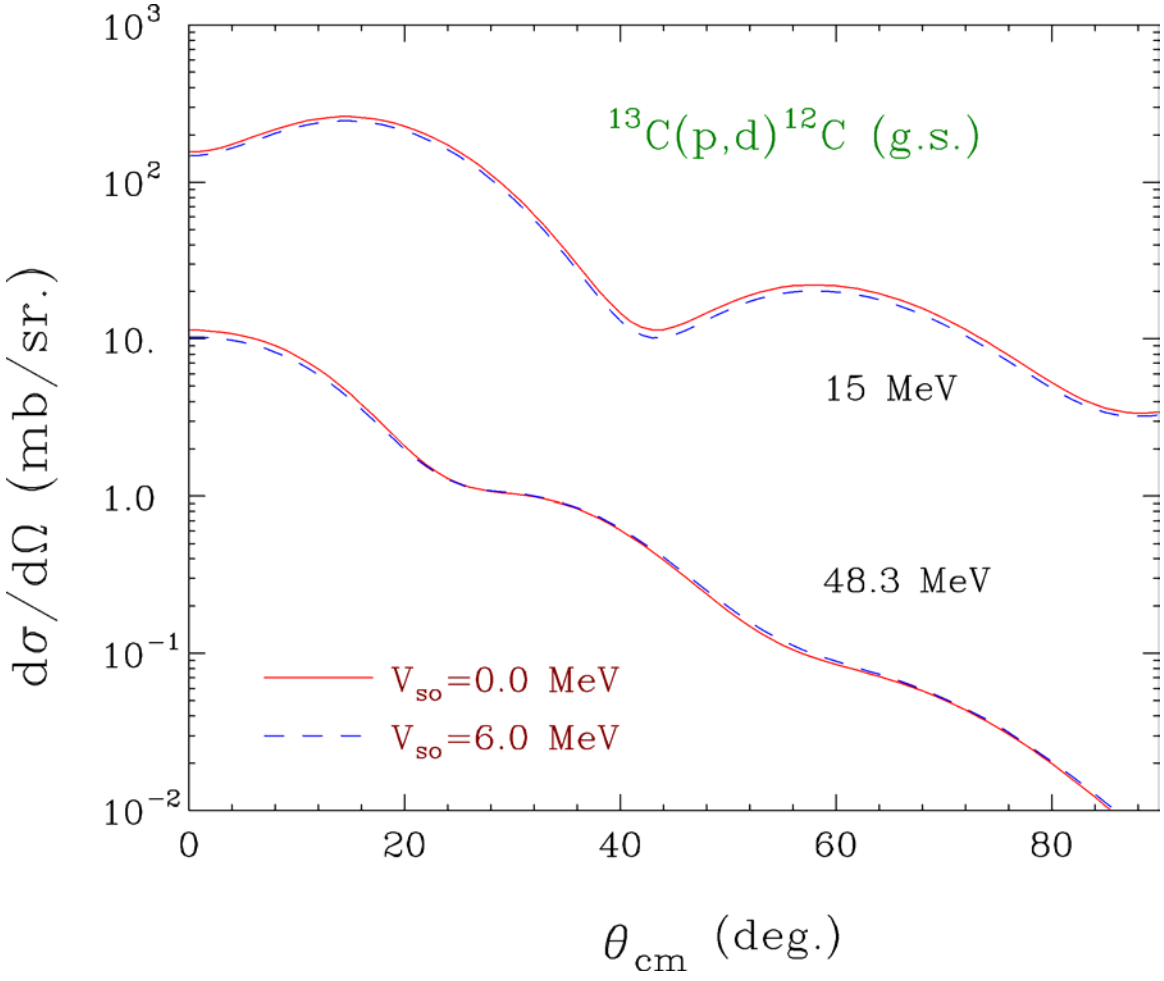

Figure 2.26: Calculations on the variation of neutron spin-orbit strength V_{so}, where the neutron radius r_0 and diffuseness a_0 are fixed to 1.25 fm and 0.65 fm separately. The cross sections at proton energy of 15 MeV are multiplied by 10.

2.3.2 Adiabatic Deuteron Breakup Approximation (ADBA)

Deuteron is composed of two loosely bound nucleons, a proton and a neutron. Since the separation energy between the proton and neutron is 2.224 MeV, deuteron breaks up easily in the field of core nucleus. Thus the extraction of the spectroscopic factors from (p,d) and (d,p) reactions using the DWBA calculations is usually not very reliable especially at high incident energy because of inadequate treatment of the breakup effect of deuteron [Pea66, But67].

Johnson and Soper [Joh70] extended the DWBA theory involving deuterons to adiabatic deuteron breakup approximation (ADBA), which requires only a specification of the nucleon-target interactions. In this approximation, the effective two-nucleon-nucleus interaction is assumed to be the sum of the nucleon optical-model potentials evaluated at one-half the incident deuteron kinetic energy. The deuteron adiabatic potential is defined as:

$$U_d(\vec{R}) = \frac{1}{D_0}\int\left\{U_n(\vec{R}+\frac{1}{2}\vec{r}) + U_p(\vec{R}-\frac{1}{2}\vec{r})\right\} V_{pn}(\vec{r})\,\phi_d(\vec{r})\,d\vec{r} \qquad (2.3.46)$$

where U_n and U_p are the neutron and proton optical potentials at one half the deuteron bombarding energy, $\vec{R}$ is the coordinate of the deuteron center of mass and $\vec{r}$ is the relative coordinate between proton and neutron, $V_{pn}(\vec{r})$ is the interaction between proton and neutron, $\phi_d(\vec{r})$ is the deuteron wave function, and D_0 is defined in Equation 2.3.36.

The exact (d,p) and (p,d) transfer reaction amplitudes require knowledge of the adiabatic three-body wave function only at small neutron-proton separations. There, the adiabatic distorting potential governing the center of mass motion of the deuteron is well

described by the sum of the neutron- and proton- target optical potentials. It is important to stress that this adiabatic distorting potential generates the three-body wave function in that limited region of configuration space needed to evaluate the transfer amplitude, and it does not describe deuteron elastic scattering at the beam energy.

Figure 2.27 shows the comparison of two deuteron potentials of ^{12}C at E_d = 49.2 MeV. The dashed line presents the Daehnick global deuteron potential and the solid line represents the adiabatic deuteron potential constructed by the CH89 nucleon potentials. The adiabatic potential based on CH89 is deeper in the interior and is shallower at the surface. The effect on the stripping or pickup cross section is to cause a faster fall off with angle and to create stronger oscillations at higher incident energy. Figure 2.28 shows the calculations of ADBA (solid line) and DWBA (dashed line) for reaction of $^{13}C(p,d)^{12}C$. At the forward peak, the ADBA calculation is 29% larger than that of the DWBA calculation.

The situation is different at lower incident energy. Figure 2.29 shows the calculations for the same reaction at proton energy of 15 MeV. The ADBA (solid line) has similar peak value as the DWBA (dashed line) and thus has little effect on the extraction of spectroscopic factors. However, to be consistent in the use of deuteron potentials throughout the range of energy, we choose ADBA calculations.

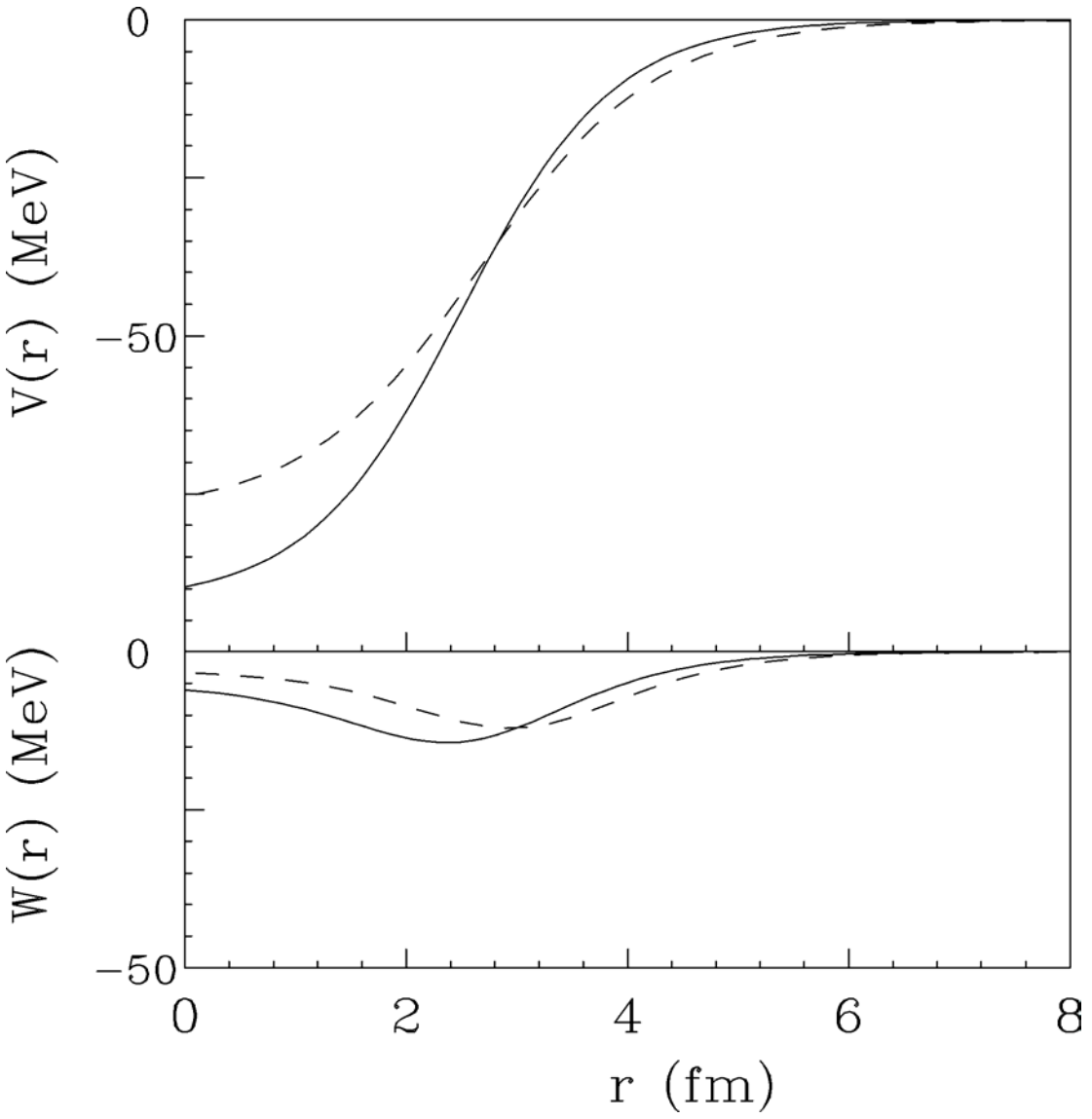

Figure 2.27: Comparison of Daehnick global deuteron potential (dashed line) with the adiabatic deuteron potential (solid line) constructed by CH89 potentials, for ^{12}C at E_d = 49.2 MeV.

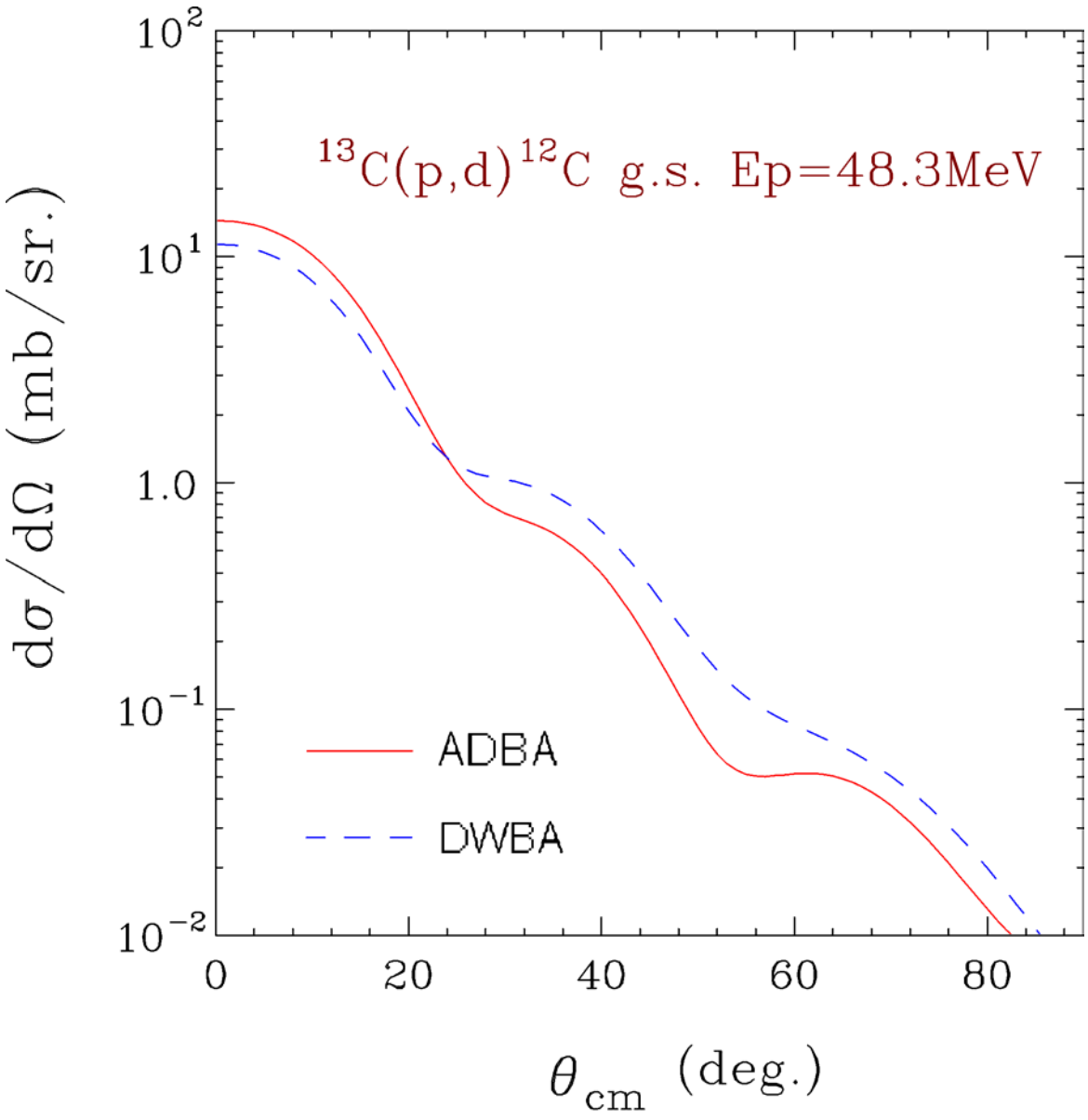

Figure 2.28: Comparison of ADBA (solid line) and DWBA (dashed line) calculations for reaction of ^{13}C(p,d)^{12}C at proton energy of 48.3 MeV. The ADBA increases the cross section at the forward angles and faster fall off than DWBA.

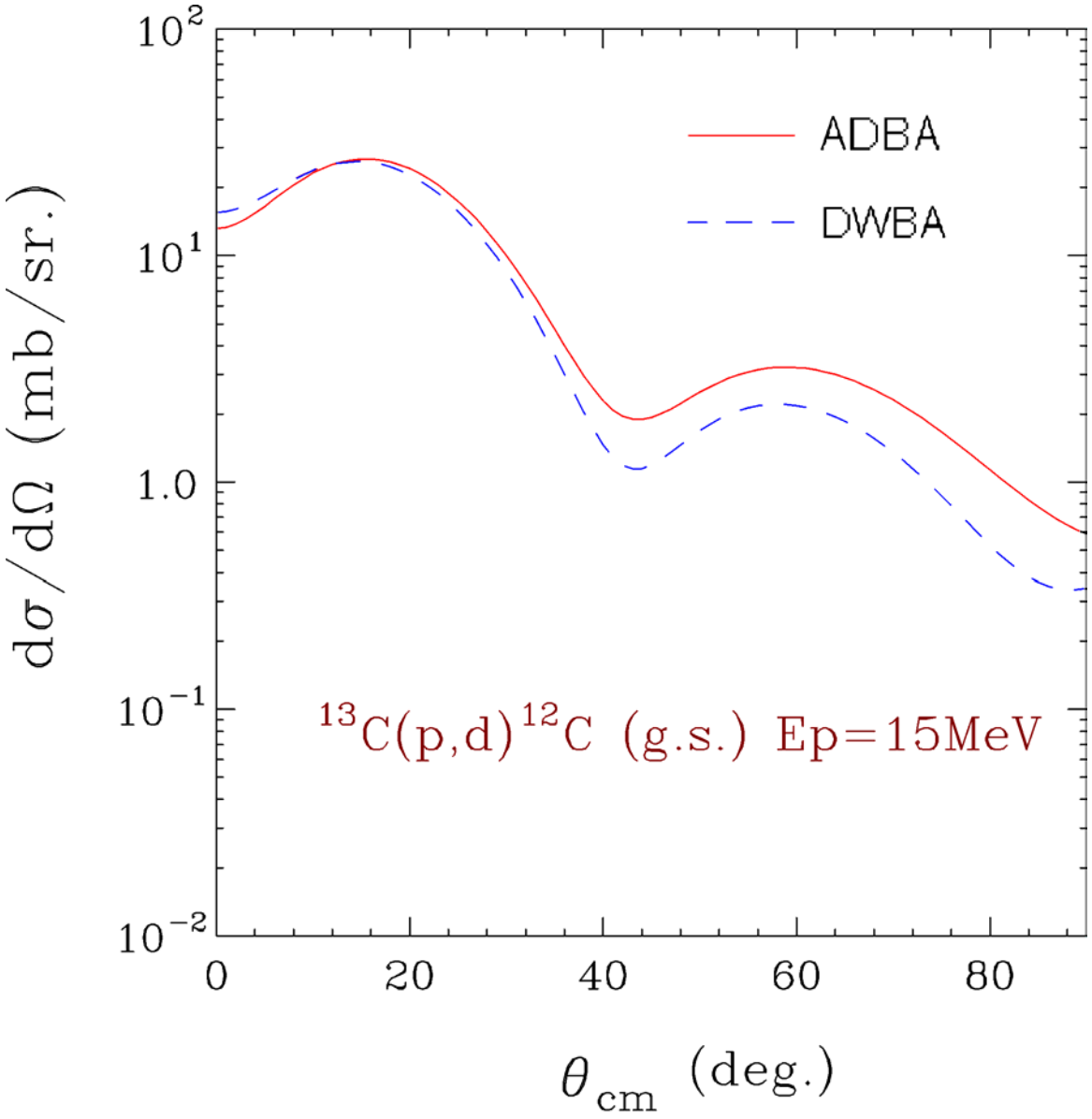

Figure 2.29: Comparison of ADBA (solid line) and DWBA (dashed line) calculations for reaction of ^{13}C(p,d)^{12}C at proton energy of 15 MeV.

2.4 Momentum Matching

Assuming P_p is the incident proton momentum and P_d is the momentum of the deuteron, the transferred momentum P_t of the neutron is given by conservation of momentum [Fes92]:

$$P_t = P_d - P_p \tag{2.4.1}$$

From this equation one can immediately determine the magnitude of P_t:

$$P_t^{\,2} = P_p^{\,2} + P_d^{\,2} - 2P_pP_d\cos\theta \tag{2.4.2}$$

Where θ is the angle between the direction of the final deuteron and the direction of the incident proton. The angular momentum transferred, $\hbar l_t$, must be less than $P_t R$, where R is the projectile-target separation at which the reaction occurs. Hence

$$\hbar^2(l_t + \frac{1}{2})^2 \le p_t^{\,2}R^2 \tag{2.4.3}$$

So that

$$\cos\theta \le \frac{(k_dR)^2 + (k_pR)^2 - (l_t + \frac{1}{2})^2}{2(k_dR)(k_pR)} \tag{2.4.4}$$

where $\hbar k$ as usual equals p. This equation expresses the approximate relation between the angular position of the first peak in the angular differential cross section and the transferred orbital momentum so that the angular position of the first peak in the measured angular differential cross section will tell us the value of the transferred orbital momentum.

The transferred momentum is bounded by the momentum of the transferred neutron by [Fes92]:

$$\left| \frac{A}{A+1} k_p - k_d \right| < \sqrt{\frac{2m|\varepsilon|}{\hbar^2}} \tag{2.4.5}$$

where ε is the binding energy of the neutron. Good momentum matching that satisfies the Equation 2.4.5 gives slow radial oscillations and large overlaps in the nuclear surface region [Aus87]. Based on the neutron binding energy listed in Table 2.6, the upward limits of the proton incident energies in ^{13}C(p,d)^{12}C reaction to the ground state and the first excited state are 32 MeV and 66 MeV respectively; for reactions of ^{11}B(p,d)^{10}B (g.s.) and ^{10}Be(p,d)^{9}Be (g.s.), the upward limits of the proton incident energies are 82 MeV and 46 MeV respectively.

2.5 Summary

As one of the fundamental tests of the shell-model theory, the spectroscopic factor measures the occupancy of a nucleon in a pure single-particle state. It can be derived from the ratio of the measured cross section to the calculated cross section assuming pure single-particle state. The theoretical cross sections are calculated via DWBA and ADBA models.

The proton and deuteron global optical-model potentials have been discussed. The nucleon-nucleus potentials of CH89 and JLM usually give better descriptions to the proton elastic scatterings than other global potentials. An adiabatic deuteron potential can be constructed based on the nucleon-nucleus potentials such as CH89 and JLM. ADBA

calculations give better predictions than the regular DWBA calculations especially at higher incident energy where deuteron break-up effect is significant.

The wave function of the transferred neutron (neutron form factor) is obtained by adjusting the depth of the neutron potential to match the neutron separation energy to the experimental value. The radius parameter and the diffuseness of the neutron potential are usually fixed to 1.25 fm and 0.65 fm respectively. The sensitivities of the calculations to the geometry parameters of neutron potential have been examined.

We chose target densities to have the form of modified Harmonic oscillator [Dej74] for the JLM potentials. The scaling factor λ of the JLM potentials were chosen to be 1.0 and 0.8 for the real and imaginary parts respectively [Pet85].

The momentum matching is discussed in Section 2.4. All the standard input parameters used in TWOFNR for our calculations are listed in Table 2.7. We adopted the value of 15006.25 $MeV^2 \cdot fm^3$ [Knu75] for the vertex constant ${D_0}^2$. Finite-range approximation is employed in the calculations with the Hulthen finite-range factor of 0.7457 fm [Knu75]. Non-locality correction is also employed with the non-locality range β_{NL} to be 0.85 fm [Per62] and 0.54 fm [Per74] for the proton and deuteron potential respectively.

Table 2.7: Summary of the input parameters used in TWOFNR

	DWBA	Adiabatic CH	Adiabatic JLM
Proton potential	Chapel-Hill [Var91]	Chapel-Hill [Var91]	JLM [Jeu77]
Deuteron potential	Daehnick [Dae80]	Adiabatic [Joh70] from CH	Adiabatic [Joh70] from JLM
Target densities			Modified Harmonic oscillator density [Dej74]
n-binding potential	Woods-Saxon, r_0=1.25 fm, a_0=0.65 fm, depth adjusted, no spin-orbit	Woods-Saxon, r_0=1.25 fm, a_0=0.65 fm, depth adjusted, no spin-orbit	Woods-Saxon, r_0=1.25 fm, a_0=0.65 fm, depth adjusted, no spin-orbit
Hulthen finite range factor (fm) [Knu75]	0.7457	0.7457	0.7457
Vertex constant D_0^2 $(MeV^2 \cdot fm^3)$ [Knu75]	15006.25	15006.25	15006.25
JLM potential scaling λ	N/A	N/A	λ_v=1.0 and λ_w=0.8 [Pet85]
Non-Locality range	p: 0.85 fm; d: 0.54 fm; n: N/A;	p: 0.85 fm; d: 0.54 fm; n: N/A;	p: 0.85 fm; d: 0.54 fm; n: N/A;

CHAPTER 3

EXPERIMENTAL SETUP AND DETECTOR CALIBRATION

3.1 Overview

This experiment was performed at the National Superconducting Cyclotron Laboratory (NSCL) at Michigan State University. One experimental objective is to study the nuclei with neutron number, N=6, such as ^{11}B and ^{10}Be which can be produced by bombarding the production target of ^{9}Be with a primary beam of ^{13}C (E=80.4 ·A MeV) produced from the K1200 cyclotron. In addition to ^{11}B and ^{10}Be beams, a secondary beam ^{13}C was also produced and the reaction p(^{13}C,d)^{12}C was used for energy calibration of the CsI detectors as explained in Section 3.3. The schematic diagram of the beam fragment separator A1200 is shown in Figure 3.1. Fragmentations from the collision of the primary beam with the production target of ^{9}Be are bent by the two dipoles. A momentum slit at dispersive image #1 selects the desired particles according to their mass and momentum. A wedge at dispersive image #2 could be used to further disperse the particles according to their energy loss. There is another momentum slit at the final achromatic image that select the desired secondary beam. The thickness of the production target (^{9}Be) and the beam intensity are listed in Table 3.1.

The experiment was carried out in the S800 vault at NSCL. Figure 3.2 shows the schematic of the facilities in the S800 vault. The secondary beam particles produced after

the A1200 were transported to the S800 line. They were bent through the analysis line consisting of Sextupoles, an Intermediate Image, Dipoles, and a Quadrupole Triplet before the target chamber. The (p,d) reactions took place inside the target chamber which contains the reaction targets of polyethylene $(CH_2)_n$ foils. The thickness of the $(CH_2)_n$ targets are listed in Table 3.1. The total detection system includes the Multi Wires Drift Counter (MWDC) detectors, the Large Area Silicon Strip Array (LASSA) [Wag01, Dav01], and the S800 spectrometer. The following sections will describe each of these detectors separately.

Table 3.1: The properties of the secondary beams and the targets

Secondary beam	Thickness of mid-target of ^{9}Be (mg/cm^2)	Secondary beam energy before target (MeV·A)	Total energy (MeV)	Equivalent proton energy (MeV)	Beam density before target (pps)	Thickness of CH_2 target (mg/cm^2)
^{11}B	837	43.8	481.8	44.1	2.5×10^{5}	2.3
^{10}Be	837	49.5	495.0	49.8	2.5×10^{5}	3.7
^{13}C	837	47.9	622.7	48.3	2.8×10^{6}	3.7
^{13}C	0.94	75.8	985.4	76.4	2.8×10^{6}	3.7

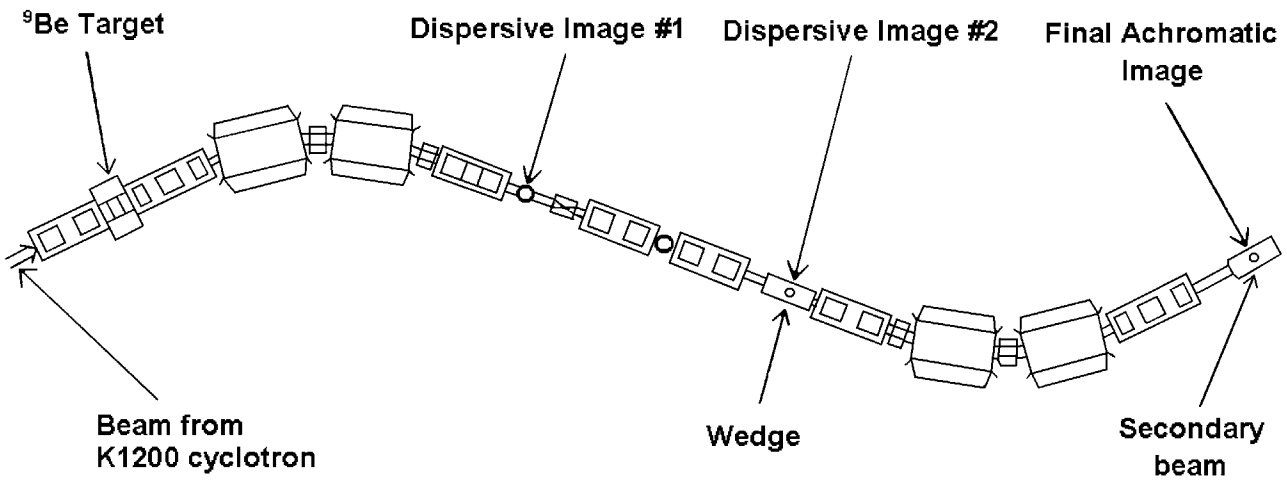

Figure 3.1: Schematic diagram of A1200.

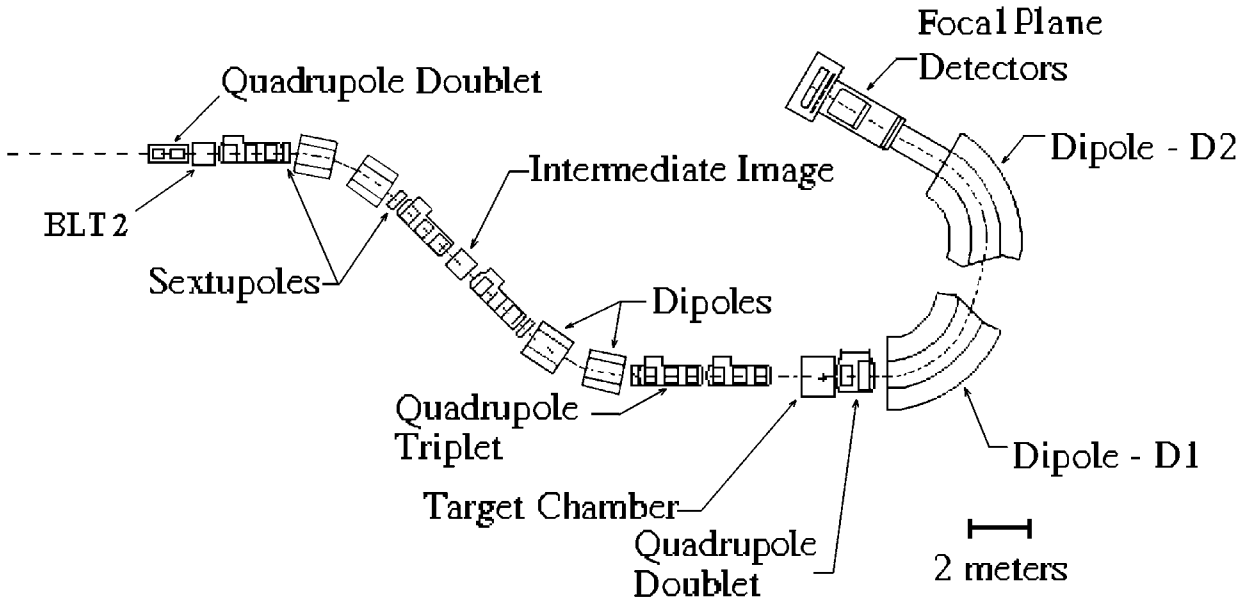

Figure 3.2: Schematic diagram of the facilities in S800 vault

3.1 MWDC Detectors

3.2.1 Principle of MWDC Detector

The Multi Wire Drift Counters (MWDC) are used to measure the beam positions and angles at the intermediate image chamber of the S800 vault. Each MWDC detector has an active area of 11.2×11.2 cm^2 covered by PPTA (p-Phenylene Terephthalamide) [Fuj89] foil of 50 μm thick at the front and back windows. It is filled with P30 gas (70% Ar and 30% CH_4) at a pressure of 500 torr. Beam particles transversing through the production targets and the MWDC detectors lose energy due to interactions of the beam with the target and other materials used to construct the counters. Taking into account the energy loss which could be substantial with thick Be targets, the beam energies before the $(CH_2)_n$ targets are calculated and listed in Table 3.1.

Each MWDC detector has two orthogonal wire planes for the X direction and the Y direction, respectively. The front and back of these two wire planes are covered by 12 μm thick mylar foil at front and back. Another mylar foil with the same thickness is placed between the two wire planes. A schematic drawing of one wire plane is shown in Figure 3.3. In each plane, there are 14 anode wires and 15 field wires. The working voltage of the anode wires is 580 Volts. The separation of the adjacent anode wires is 8.0 mm, and all the anode wires are connected to a micro-strip delay line. This delay line has two timing outputs T_1 and T_2. The field wires are separated into two groups. Every other field

wire is connected together and gives the left-right position signals E_1 and E_2, respectively.

An enlarged drawing for the ions drifting between the wires is shown in Figure 3.4. The positive ions drift towards the field wires and the negative electrons drift towards the anode wire. The time signals T_1 and T_2 are expressed as:

$$T_1 = dt_1 + (k-1)\cdot Z_0 + dt \tag{3.2.1}$$

$$T_2 = dt_2 + (14-k)\cdot Z_0 + dt \tag{3.2.2}$$

where Z_0 is the delay time between adjacent anode wires, dt_1 and dt_2 are the delay times from the left and right wire ends to the preamplifier respectively, dt is the drift time of the negative electrons from the hit point to the anode wire, and k is the wire sequential number. Subtracting T_2 from T_1 yields :

$$T_1 - T_2 = dt_1 - dt_2 + (2k-15)\cdot Z_0 \tag{3.2.3}$$

Then the wire sequential number k is

$$k = \frac{(T_1 - T_2 - dt_1 + dt_2)}{2Z_0} + \frac{15}{2} \tag{3.2.4}$$

A spectrum of the wire sequential number k is shown in Figure 3.5. By adding T_1 and T_2, we get

$$T_1 + T_2 = dt_1 + dt_2 + 13Z_0 + 2dt \tag{3.2.5}$$

Then the drift time dt is

$$dt = \frac{T_1 + T_2 - dt_1 - dt_2 - 13Z_0}{2} \tag{3.2.6}$$

A spectrum of the drift time dt is shown in Figure 3.6, where the time is scaled in units of microseconds (μ sec). The sharp peak near the zero drift time and the tail at the drift

time around 80 μs correspond to the nonlinear electron drifting. Analysis indicated that 5% of the total particles are affected by this nonlinear behavior.

The left-right ambiguity is resolved by comparing the amplitudes of the two signals E_1 and E_2 from the field wires. When the negative ions move close to the anode wires, they produce a significant multiplicative effect and produce lots of positive ions around the anode wire. Some of the positive ions will drift to the field wires. Since more positive ions are produced on the side that the negative ions drift from, the particles hitting at one side of anode wire produce larger signals on field wire in this side than the other. Figure 3.7 depicts a typical spectrum of the signals from one side of field wires versus the signals from the other side.

Since alternate field wires are connected together, the particle position is calculated as following in units of millimeters (mm).

$$p = 8.0k + (-1)^k \cdot \Theta \cdot \frac{dt}{20.0} - D, \quad \Theta = \begin{cases} 1, & E_1 < E_2 \\ -1, & E_1 > E_2 \end{cases} \tag{3.2.7}$$

where k is the wire sequential number, dt is the drift time, D is the alignment center in value of 60.0 mm, and Θ is the left-right ambiguity function of E_1 and E_2.

3.2.2 Position Calibration

To ensure that all the equations used in the position determination of MWDC detectors are correct, a mask made of a 3.1 mm-thick brass plate is used to calibrate the position. Figure 3.8(a) shows the pattern on the mask. The distance between adjacent big holes is 10.2 mm; the distance between adjacent small holes is 2.54 mm. There is one L-

shaped slit with the width of 2.0 mm. The area in the middle surrounded by a dotted rectangle is the area that detected the passing beam particles. Figure 3.8(b) is the reconstructed two-dimensional position spectrum of the mask using the ^{11}B beam, where the beam was focused on the middle position between the first and second MWDC detectors. A position resolution of 0.4 mm was achieved.

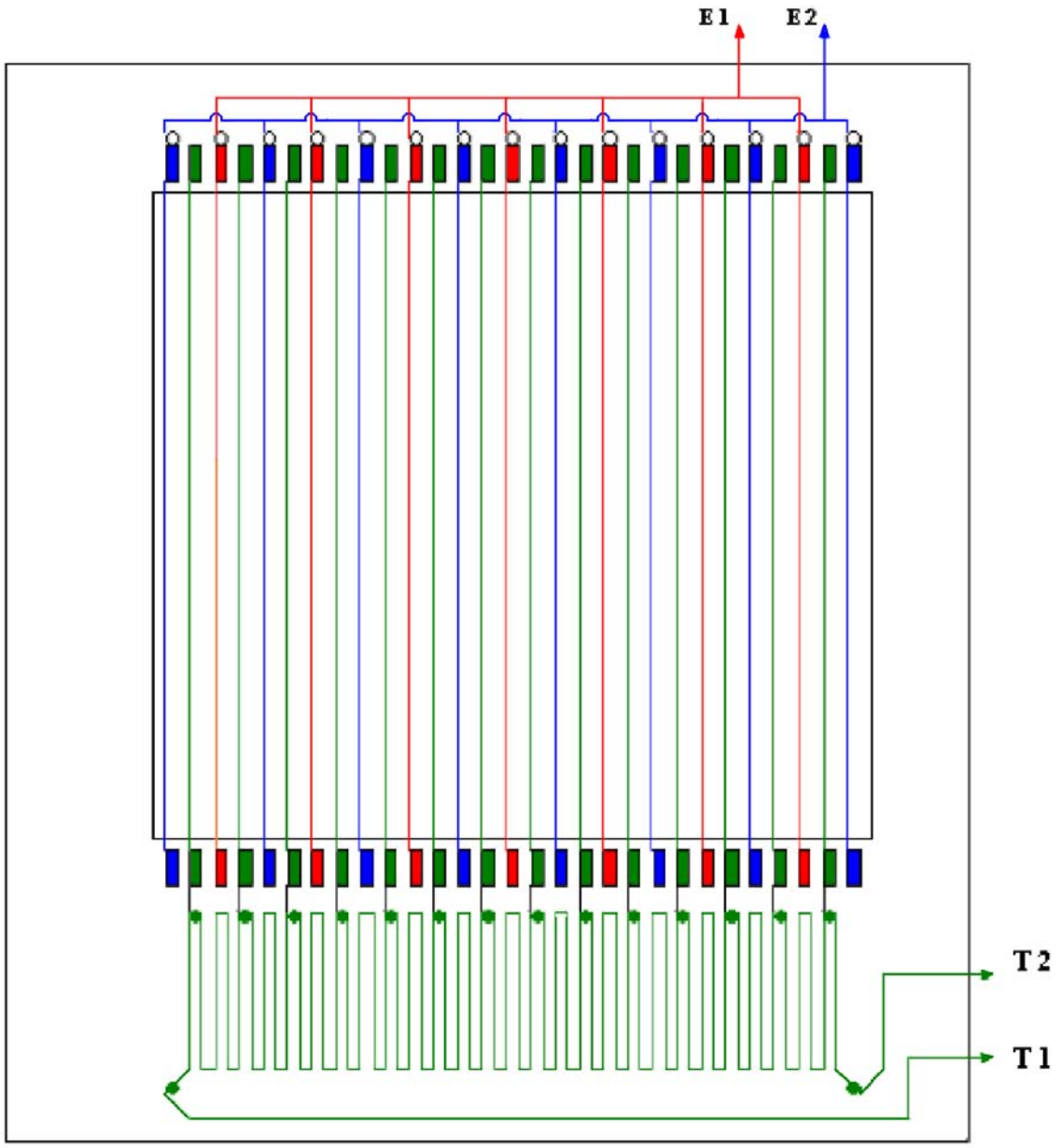

Figure 3.3: Schematic drawing of wire plane of MWDC detector. All the anode wires are connected to a micro-strip delay line, which has two timing outputs T_1 and T_2. Every other field wire is connected together to form two groups and gives the left-right ambiguity signals E_1 and E_2, respectively.

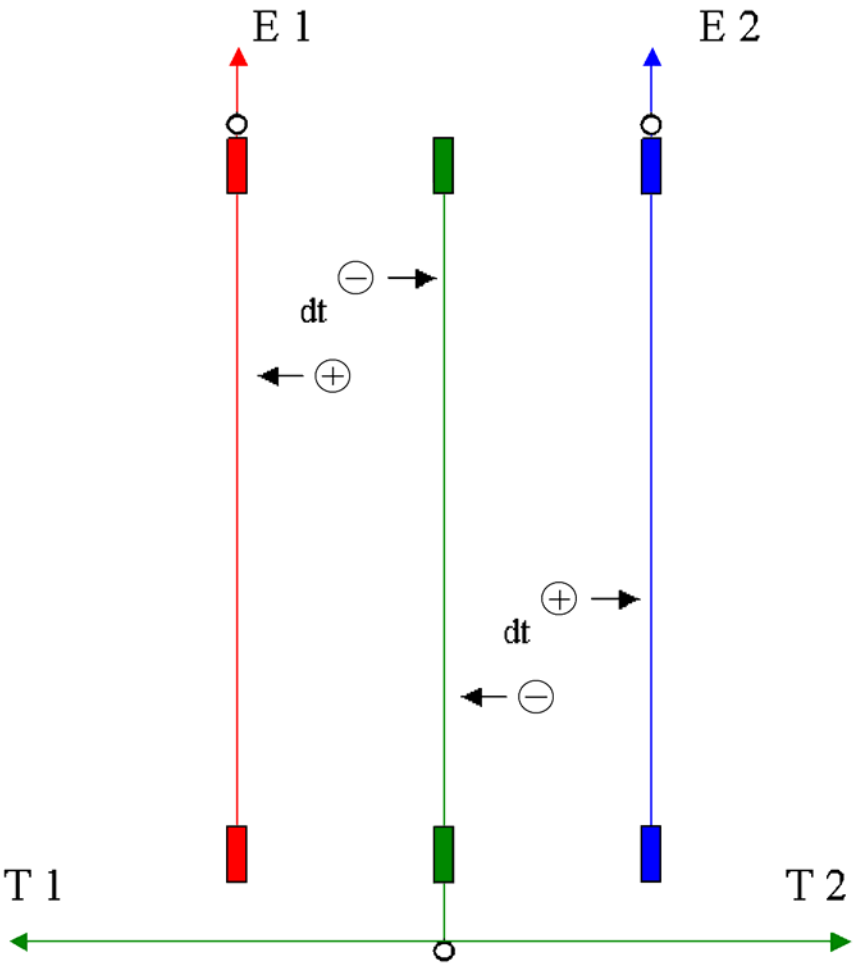

Figure 3.4: An enlarged drawing of the ions drifting between the wires. The positive ions drift toward the field wires and the negative ions drift toward the anode wire. The term dt is the drift time of the negative ions from the hit point to the anode wire.

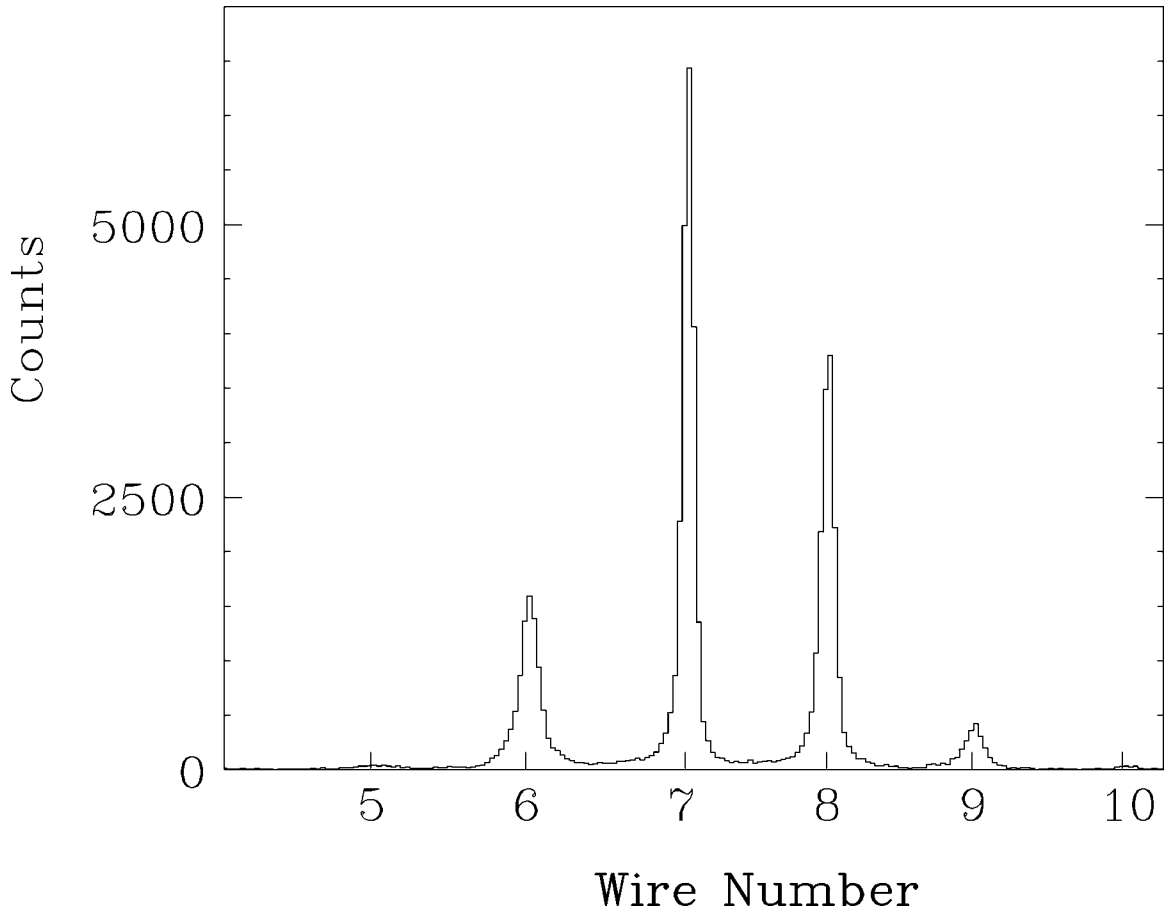

Figure 3.5: Spectrum of the wire sequential number k. Each individual sharp peak indicates the wire with its sequential number.

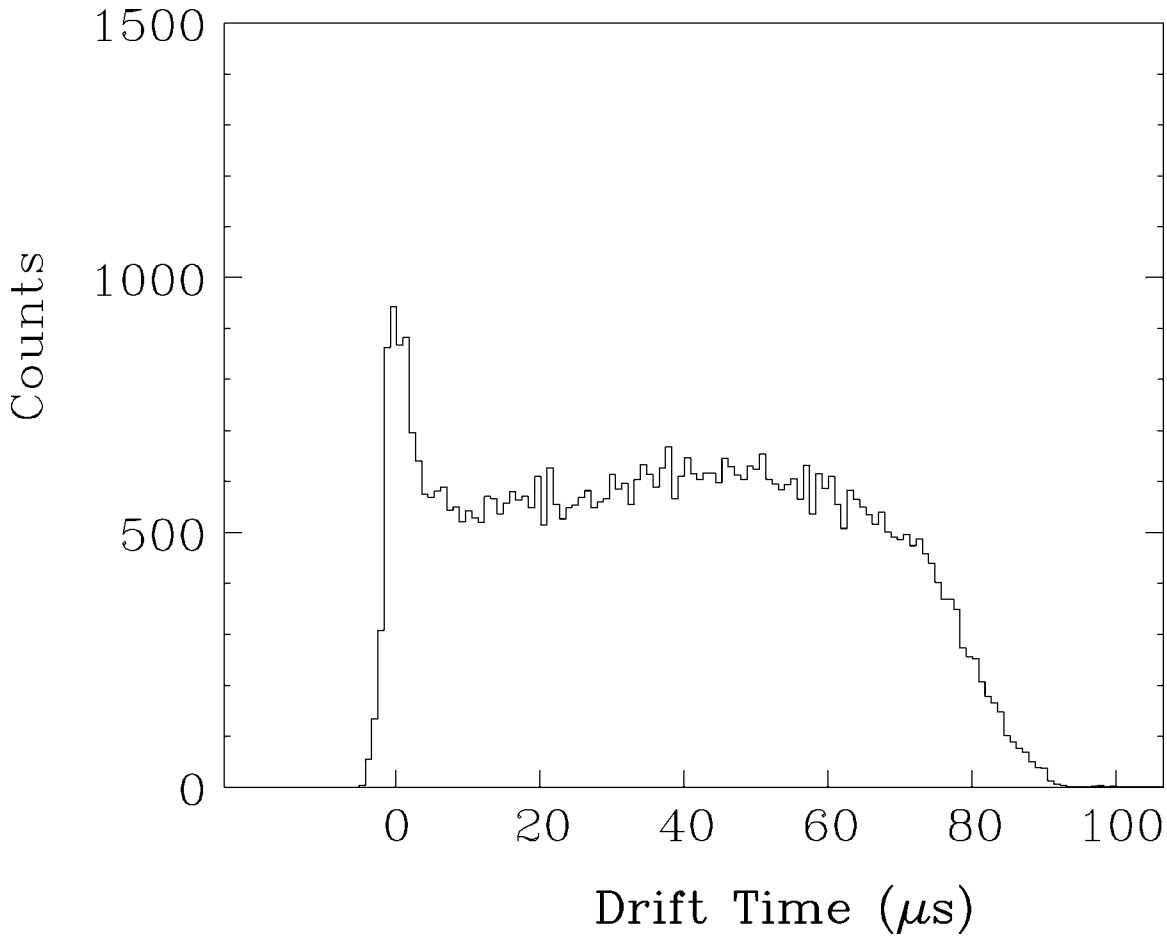

Figure 3.6: Spectrum of drift time dt, where the time is scaled in units of microseconds.

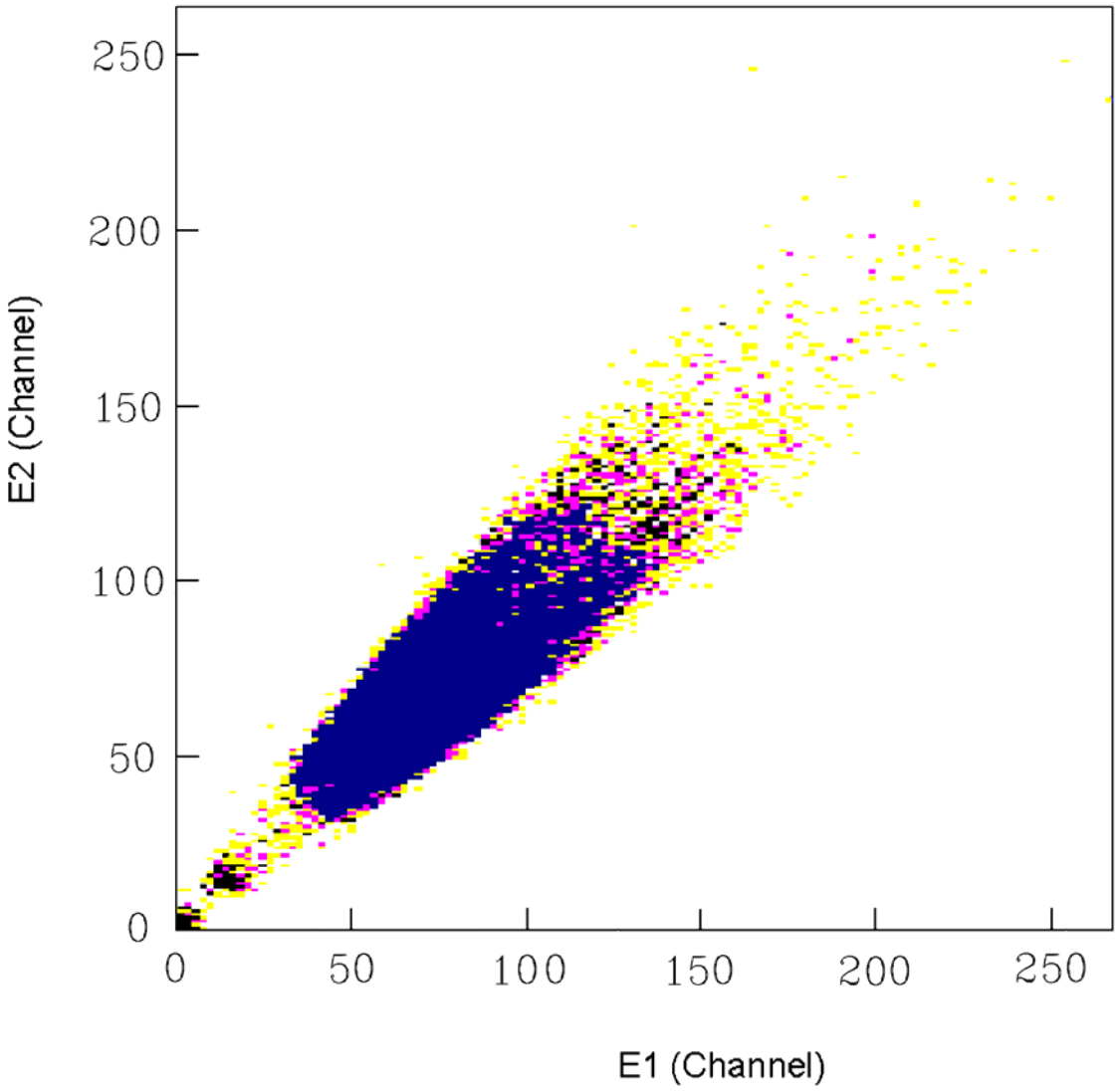

Figure 3.7: Spectrum of E_2 versus E_1. There are two groups of particles. The left-right ambiguity can be clarified by which side yields a larger signal than the other.

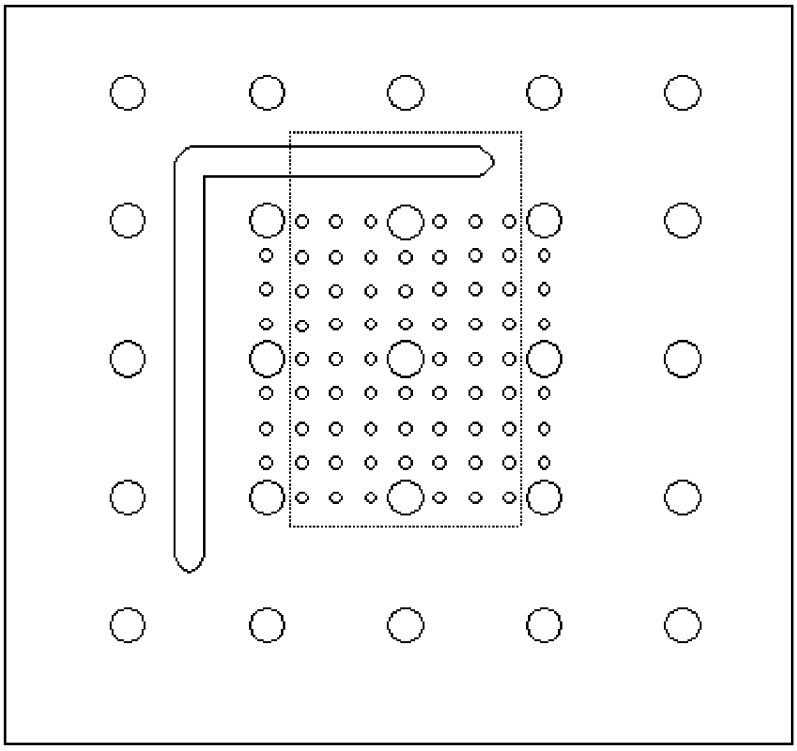

(a)

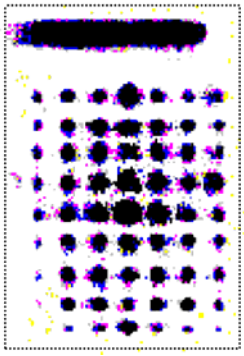

(b)

Figure 3.8: (a) Patterns on the mask used to calibrate the MWDC detector. The distance between adjacent small holes is 2.54 mm; the distance between adjacent big holes is 10.2 mm; (b) The two-dimensional position spectrum of the mask. The corresponding areas are surrounded by the dotted rectangle in (a) and (b).

3.3 LASSA Detector Array

3.3.1 Overview

The Large Area Strip Silicon Array (LASSA) was designed and constructed to provide excellent energy, angular, and isotope resolution for the detection of charged particles. It has been used successfully to study the isospin degree of freedom in heavy ion multifragmentation experiments at NSCL [Tan02, Liu05]. It consists of 9 individual telescopes, which can be arranged into various configurations. Each LASSA telescope consists of two silicon strip detectors and a cluster of four CsI(Tl) scintillators. The side view of the telescope assembly is shown in Figure 3.9. A 5 mg/cm^2 SnPb foil covers the top window and provides a dark environment to the Si detectors. In addition, the foil also protects the Si detectors from electrons produced in nuclear collisions. The two silicon strip detectors are mounted inside the top frame below the SnPb foil. Right behind the two silicon detectors are four CsI crystals with light guides and photodiodes mounted on the back. The preamplifiers, and their motherboards, for the CsI detectors are placed directly behind the photodiodes. A cooling bar is mounted at the back of each telescope to keep the telescope at constant temperature.

3.3.2 Geometric Setup

In this experiment, LASSA is used to detect the deuteron particles emitted from the (p,d) reactions. The 9 telescopes were separated into three groups and mounted on three independent frames. A schematic drawing of the detector setup is shown in Figure 3.10.

The following coordination in the laboratory frame has been adopted: the beam direction is defined as the z axis and the upward direction is the x axis; the polar angle θ defined the angle of the particle direction with respect to the beam axis; the angle α is the angle between the particle projection on the z-y plane and the z axis; the angle β is the angle of the particle direction with respect to its projection on the z-y plane. For reference, each telescope is assigned a number as labeled in Figure 3.10. The geometry of the centoid of each telescope is specified in Table 3.2. The detectors cover the angular range of $3.6° < \theta < 36.9°$ in the laboratory frame, which covers mainly the first peaks of the transfer reactions. Beyond this region, the kinematic broadenings increase dramatically in inverse kinematics.

3.3.3 Silicon Strip Detector Array

3.3.3.1 Overview

Silicon strip detectors are widely used in nuclear experiments because of their excellent energy resolution and linear response for charged particles. Both layers of silicon strip detectors used in LASSA are ion-implanted, passivated devices, Si(IP),

obtained from Micron Semiconductor [Micr]. For all the strip detectors used in our experiment, the width of each strip is 3 mm, and there is a 0.1 mm wide gap between adjacent strips. The active area on each surface is about 50×50 mm^2.

The front silicon detector, which is labeled as DE, is about 65 μm thick. It has 16 strips on the front surface. There are two different types of silicon strip detectors for the second Si detector. One is double-sided and about 500 μm thick, and the other type is single-sided and about 1000 μm thick. In the double-sided detector, the strips on the front are perpendicular to the strips on the back. For convenience, we refer the front strips and the back strips of the double-sided detector as EF and EB respectively. For the single-sided second detector, only the label EF is used. The close-packed design of the telescopes right next to each other with a minimum dead area required the development of a highly flexible flat printed circuit board cable connecting the silicon strip detectors with the pre-amplifier housings. Figure 3.11 shows the picture of a double-sided silicon strip detector with the flat printed circuit board cables. The combinations of the silicon strip detectors are listed in Table 3.2. The reason for choosing 1.0 mm silicon detector for telescope 2, 4, 5, and 9 is that the deuterons emitted at smaller angles have lower energies and will be stopped inside the 1.0 mm silicon detectors. The deuterons emitted at larger angles with higher energies (E>10.8 MeV) would punch through the 500 μm silicon detectors and be stopped in the CsI(Tl) crystals.

One advantage of silicon-strip detectors is their position resolution. For the double-sided detectors, we can use the orthogonal strips on EF and EB to obtain each particle's (x, y) pixelwise position. When the 1.0 mm detector is used, its strips are oriented orthogonally to the strips in the DE silicon detector to provide a two-dimensional

position. As the strips are 3.1 mm apart, the 50mm×50mm lateral dimensions of each telescope are divided into 256 (16×16) square pixels with a resolution of 3×3 mm^2. At a distance of 205.3 mm, the angular resolution of the pixel is 0.43 deg. Telescopes 4, 5, and 7 were placed at a greater distance of 392.6 mm and their angular resolution is 0.22 deg. All the position and angular information is summarized in Table 3.2.

3.3.3.2 Energy Calibration

One advantage of silicon detectors is their linear and largely particle independent energy response. In this experiment, the relevant deuteron energies range from 9.0 MeV to 20 MeV. The silicon energy response in this range is very linear. However, due to the nonlinearity of electronic system including preamplifiers, shapers, and ADCs, energy calibration must be performed.

A BNC (Berkeley Nuclear Co.) precision pulser generator was used to calibrate the silicon detectors. The pulser has a group of attenuation switches to change the amplitude of the output signal. Three attenuation settings were chosen corresponding to three different dynamic ranges. An absolute calibration was obtained from the measurements of ^{228}Th α source for these three settings. The linear relation between the pulser dial value and its equivalent energy was obtained:

$$E = a \cdot W + b \tag{3.3.1}$$

where E is the equivalent energy of the pulser signal in the units of MeV, and W is the dial value in the Volts. The values of a and b for the three different settings, as listed in

Table 3.3, show that the output of the pulser is not strictly proportional to the dial voltage and the offsets are not zero.

Right after the experiment was finished with all the electronics setup intact, the calibrated pulser signals were sent as inputs into the preamps of each strip. Then one-by-one, the pulser-calibration was carried out for all 352 silicon channels. The signals were read by the DAQ program and analyzed with the analysis program SMAUG. A linear fitting was performed to the channel reading C and the energy E converted from the pulser dial value W by Equation 3.3.1. The relation between C and E was obtained for each strip:

$$E = g_i \cdot C + h_i \tag{3.3.2}$$

where i stands for each strip. Equation 3.3.2 was used to convert the channel readout from each strip into particle energy in units of MeV. There is a total of 352 calibration curves for the Si-strips. As an example, Figure 3.12 shows the calibration curve for the No.6 strip of the EF detector in telescope 3.

3.3.3.3 Particle Identification

In a heavy ion collision, many kinds of particles like protons, deuterons, tritons, and other fragments from the projectiles are detected in LASSA detectors. Since we are only interested in the deuterons, a particle identification (PID) must be performed to distinguish the other particles. The PID can be performed by a combination of ΔE and E detectors.

For particles passing through a detector, the energy loss is approximated by the Bethe formula [Bar96]:

$$\Delta E \approx \frac{k A Z^2}{E} dx \tag{3.3.3}$$

where dx is the detector thickness, k is a proportional constant, A is the mass number, and Z is the atomic number of the particles. For a fixed dx, a plot of ΔE versus E yield a family of contours with $\Delta E \propto 1/E$. Each line corresponds to an integer value of Z and A.

Figure 3.13 shows the ΔE-E spectrum of telescope 7. The x axis is the particle energy deposited in the EF strip detector; the y axis is the energy loss deposited in the DE strip detector. By vetoing the particles stopped in CsI(Tl) crystals, we were able to separate the deuterons and protons as well as tritons.

3.3.3.4 Position Calibration

The position determination of the emitted deuterons is critical in this experiment. To determine the position of each pixel of the telescope accurately, we need to perform the position calibration. The angular position (α, β) of the center of each telescope was determined optically by using a system composed of a optical telescope and a mirror as shown in Figure 3.14. The mirror was mounted on a turntable which can be rotated in both horizontal and vertical planes and the rotation angles can be read from the turntable. The center of the mirror was placed at the center of the target in the experiment. The optical telescope was mounted in the beam line. The mirror was rotated until the center of each detector is visible and aligned with the optical telescope, then the angular positions

(α, β) of the detector center are:

$$\alpha = 2 \cdot \alpha_0$$

$$\beta = 2 \cdot \beta_0 \tag{3.3.4}$$

where α_0 and β_0 are the angles of the mirror rotated in the horizontal and vertical planes. The rotation angles can be read to the accuracy of 0.01 degree so the accuracy of the measurement is 0.02 degree. The angular position of the center of each detector is listed in Table 3.2. The coordinates $\vec{r}(x, y, z)$ of each pixel of the LASSA telescopes are obtained by:

$$\vec{r}(x, y, z) = R_x(\alpha) \cdot R_y(\beta) \cdot \vec{r}_0(x_0, y_0, z_0) \tag{3.3.5}$$

where z_0 is the distance between the target and the center of the detector; x_0 and y_0 are the vertical and horizontal distances between the pixel and the center of the detector, respectively; $R_x(\alpha)$ and $R_y(\beta)$ are the rotation matrices along the x axis and y axis. They are defined as:

$$R_x(\alpha) = \begin{pmatrix} 0 & 0 & 0 \\ 0 & \cos\alpha & \sin\alpha \\ 0 & -\sin\alpha & \cos\alpha \end{pmatrix}$$

$$R_y(\beta) = \begin{pmatrix} \cos\beta & 0 & -\sin\beta \\ 0 & 0 & 0 \\ \sin\beta & 0 & \cos\beta \end{pmatrix} \tag{3.3.6}$$

We performed the calibration before and after the experiment. The positions did not change during the experiment.

3.3.4 CsI(Tl) Crystals

3.3.4.1 Detectors

The CsI(Tl) crystals are produced by Scionix [Scio]. A non-uniformity in light output of CsI(Tl) crystals better than 1% was obtained via crystal selection and a quality control procedure [Mic99, Tan02]. Each crystal is trapezoidal in shape as shown in Figure 3.15, and the length of the crystal is 6.0 cm. The front and back areas are 2.64×2.64 cm^2 and 3.38×3.38 cm^2, respectively. To allow compact packing, the sides between adjacent crystals are at right angles to each other while the sides next to the frame are cut at an angle of 7.09 degrees. Each crystal is wrapped with two layers of cellulose nitrate on the outer surfaces (next to the frame) and one layer on the inner surfaces. One layer of aluminized mylar foil (0.15 mg/cm^2 mylar + 0.02 mg/cm^2 Al) is inserted between adjacent crystals to ensure optical isolation.

Each crystal is optically coupled to a clear 1.0×3.5×3.5 cm^3 acrylic light guide with optical epoxy BC600 [Bicr]. This light guide is in turn optically connected to a 2.0×2.0 cm^2 Hamamatsu S3204 photodiode [Hama] with clear silicone rubber compound RTV615 [Gene]. To prevent light leak and cross-talks between adjacent crystals, the outer sides of the light guide and the photodiode are painted with a reflective white paint BC620 [Bicr].

To reduce the noise level, the charge-sensitive preamplifiers are mounted right behind the crystals to reduce the length of the input cables and minimize the capacity input to the

preamplifiers. There are two motherboards in one telescope. Each one hosts two preamplifiers.

Fig 3.9 shows the internal mounting structure, the outside of the detector box is open and the two silicon strip detectors are placed on the side. An aluminum mylar foil covers the top of the wrapped crystals to maximize light reflection and improve the energy resolution. One motherboard of the preamplifiers can be seen under the crystals.

Three major precautions are taken to reduce the cross-talks between the preamplifiers of the CsI detectors. The first is to place a grounded copper shielding between the two motherboards to minimize broadcasting; the second is to put a 110 Ω resistor on the test input line connecting the two preamplifiers on the same motherboard to terminate each amplifier; the third is to use shielded coaxial cables instead of twisted-pair cables to reduce the broadcasting between cables. With this set up, the cross-talks are reduced to the level of 0.1% [Mar98].

3.3.4.2 Energy Calibration

The fluorescence emitted by the CsI(Tl) scintillator has two major components of a fast (500 ns) and a slow (7 μs) decay time constants. The relationship of light output and energy is mass and charge dependent. Therefore the CsI calibration cannot be performed by different kind of particle, neither by pulsers. In addition, the light output of a CsI crystal also depends on the Tl doping of CsI crystals. Since every CsI crystal may have different doping during manufactory, it is necessary to perform calibration for each CsI crystal individually.

For heavy ions at low energy, the light output of a CsI crystal shows non-linear response to the deposited energy [Lar94, Bir51]. However, for the isotopes of hydrogen, Tan [Tan02] and Handzy [Han95] found that linear functions result in good fitting. However, previous calibrations did not extend deuteron calibration below 20 MeV, so the deuteron response function for the CsI crystals was not known in our energy region of interest.

Calibration of the CsI(Tl) crystals was achieved by the reaction of $p(^{13}C,d)^{12}C$. ^{13}C is the primary beam with high beam density. The emitted deuterons corresponding to the ground state and the first excited state of ^{12}C can be identified clearly in the energy spectrum. As the deuteron scattering angle is known from position calibration of the pixels, the deuteron energy is obtained by kinematic calculation. As shown in Figure 3.16, the emitted deuteron goes through target, SnPb foil on the window of telescope, DE silicon strip detector, and EF(EB) silicon strip detector before being stopped in CsI detector. The deuteron energy deposited into the CsI detector is:

$$E_{CsI} = E_d - \Delta E_{tar} - \Delta E_{SnPb} - \Delta E_{DE} - \Delta E_{EF} \tag{3.3.7}$$

where E_d is the emitted energy of the deuteron from the target determined from kinematics, ΔE_{tar} and ΔE_{SnPb} are the deuteron energy losses in target and SnPb foil respectively. These energy losses are obtained using the program ENLOSS [Enlo] according to the material components and thickness. ΔE_{DE} and ΔE_{EF} are the energies deposited into DE and EF(EB) silicon strip detectors. Then the channel readout C_{CsI} from CsI detector can be calibrated to E_{CsI} by a linear fitting:

$$E_{CsI} = \lambda_i \cdot C_{CsI} + \rho_i \tag{3.3.8}$$

where i stands for each CsI crystal. This equation was used to convert the readout of the CsI detectors into particle energy in units of MeV. Figure 3.17 shows the calibration curve for the No. 3 crystal in telescope 3. Clearly, the linear fitting works very well for the deuteron calibration from 1 MeV to 14 MeV. This result is consistent with the observations of Tan [Tan02] and Handzy [Han95]. Our fitting results in a precision of the calibration better than 2%.

3.3.4.3 Particle Identification

For the particles that stopped in CsI(Tl) crystals, the particle identification can be performed by the combination of silicon strip detectors and CsI(Tl) detector. Figure 3.18 shows the ΔE-E spectrum of telescope 3. The x axis is the particle total energy, including the energies deposited in DE, EF(EB) silicon strip detectors and CsI detector; the y axis is the sum of 4 times the energy loss in DE detector and the energy loss in EF(EB) detector. The deuterons and protons are well separated.

Table 3.2: Geometric setup of the telescopes and the configurations of the silicon strip detectors.

Telescope No.	θ (deg.)	α (deg.)	β (deg.)	Dist. (mm)	Angular resolution	Thickness of DE silicon strip detector (μm)	Thickness of EF/EB silicon strip detector (μm)
1	21.5	-14.2	-16.3	205.3	±0.43°	67	480
2	14.2	-14.2	0	205.3	±0.43°	68	978
3	21.5	-14.2	16.3	205.3	±0.43°	64	500
4	7.0	0	-7.0	392.6	±0.22°	64	913
5	7.0	0	7.0	392.6	±0.22°	65	982
6	27.9	23.0	-16.3	205.3	±0.43°	67	481
7	16.7	0	16.7	392.6	±0.22°	66	476
8	27.9	23.0	16.3	205.3	±0.43°	70	482
9	23.0	23.0	0	205.3	±0.43°	66	993

Table 3.3: The calibrated parameters in Equation 3.3.1

Attenuating setting	Maximum energy range	a	b
× 2	30 MeV	5.0592	-0.1081
× 5	16 MeV	2.0347	-0.0933
× 20	3 MeV	0.5115	-0.1223

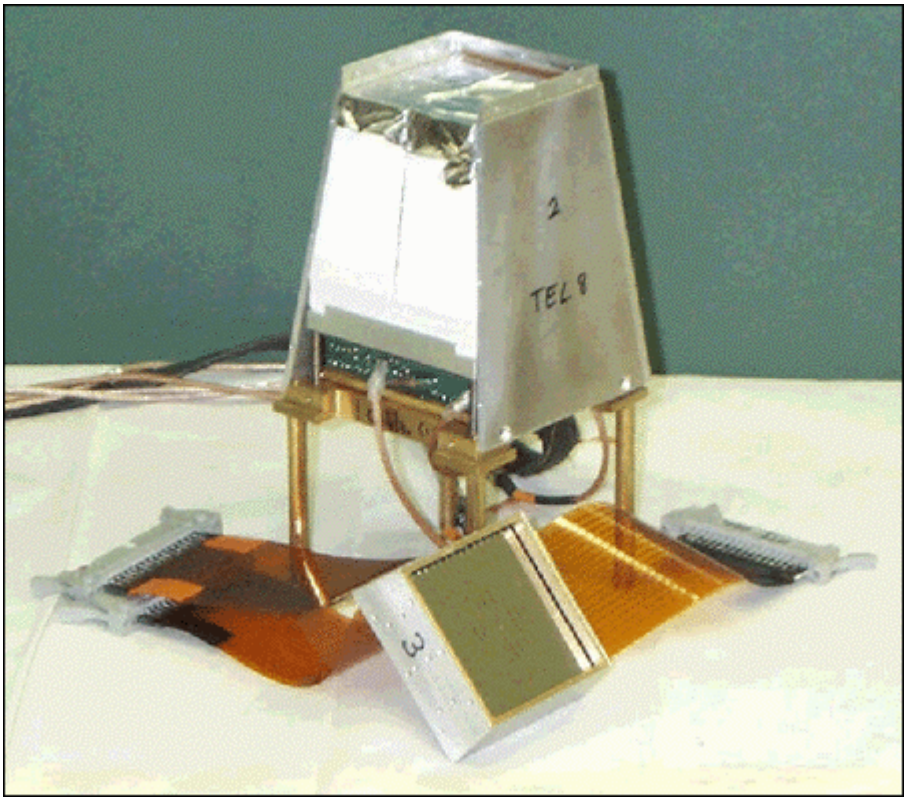

Figure 3.9: Structure of LASSA telescope.

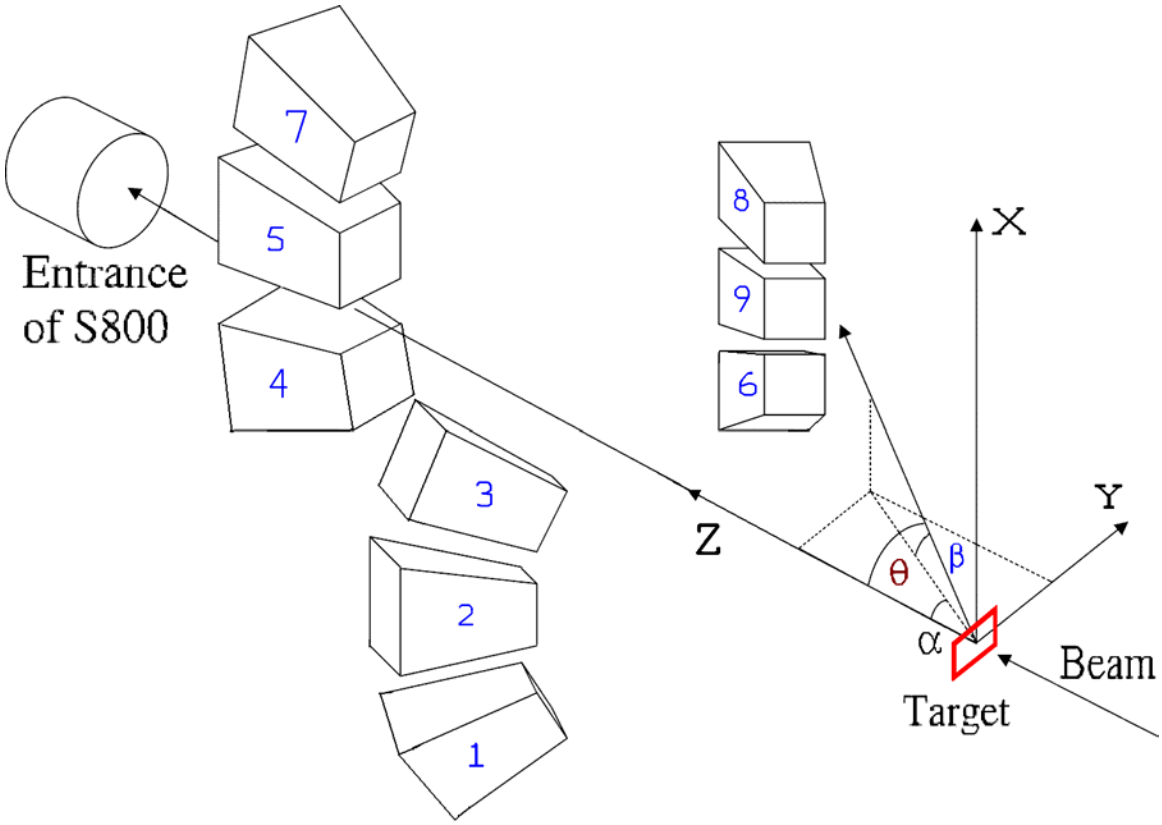

Figure 3.10: Schematic of the geometric setup.

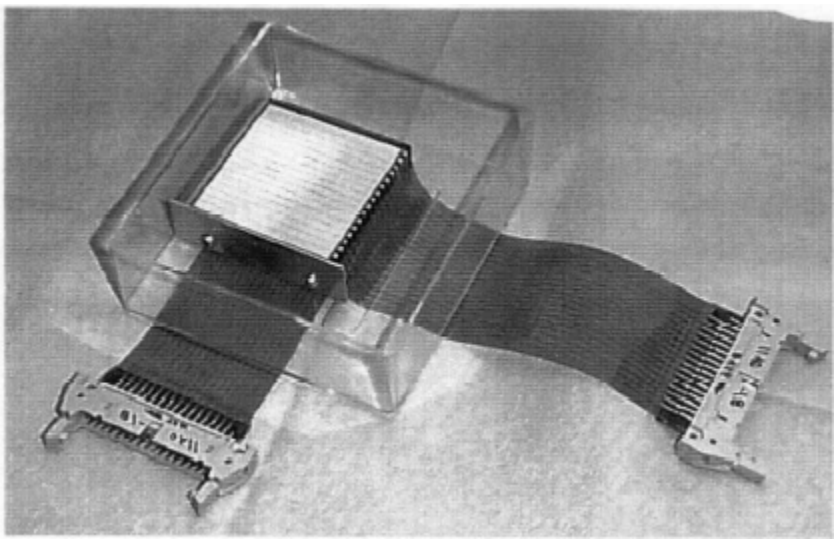

Figure 3.11: One double-sided silicon strip detector with the flat printed circuit board cables.

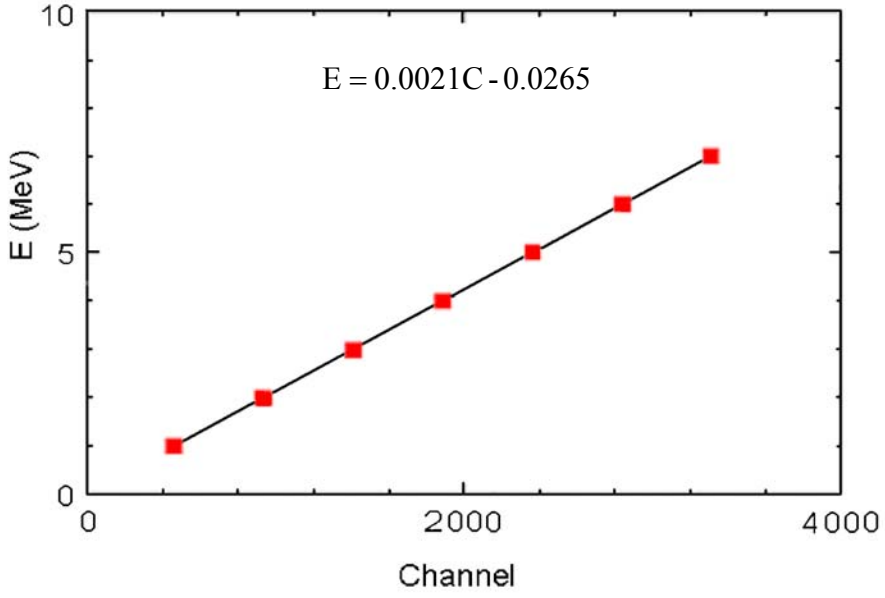

Figure 3.12: Calibration curve for silicon strip detector, by which the channel readout of the silicon strip detector is converted to particle energy in units of MeV. This curve stands for the No. 6 strip of EF detector in telescope 3.

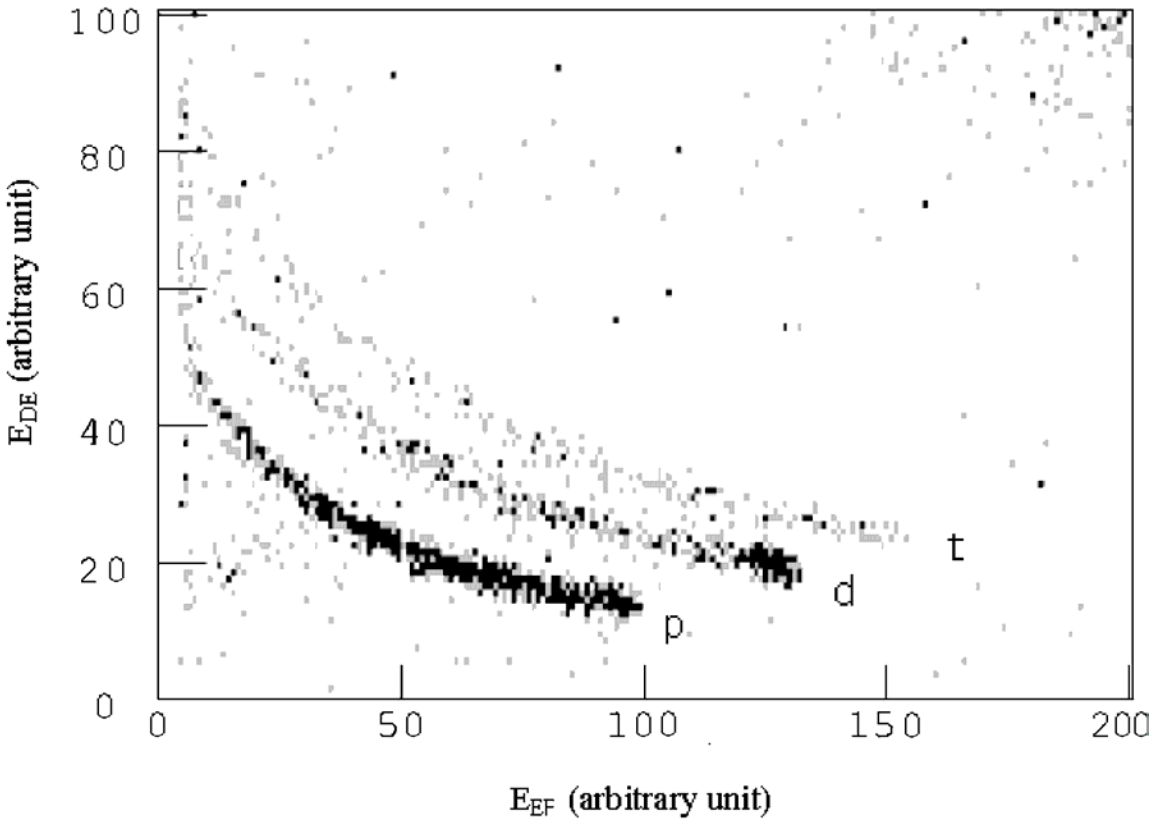

Figure 3.13: Particle identification using the energy spectrum of E_{DE} vs. E_{EF} for telescope 7.

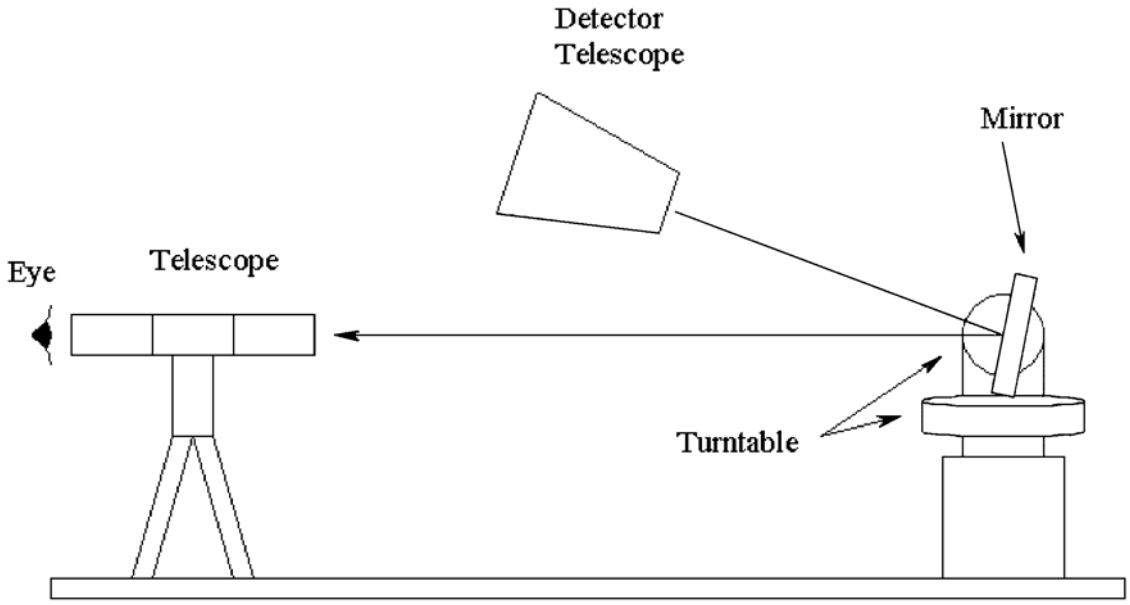

Figure 3.14: Geometry calibration system composed of one optical telescope and a mirror mounted on a turntable with two orthogonal axes that rotate in horizontal and vertical planes. The center of the mirror is the position of the target in the experiment and the optical telescope is mounted in the beam line.

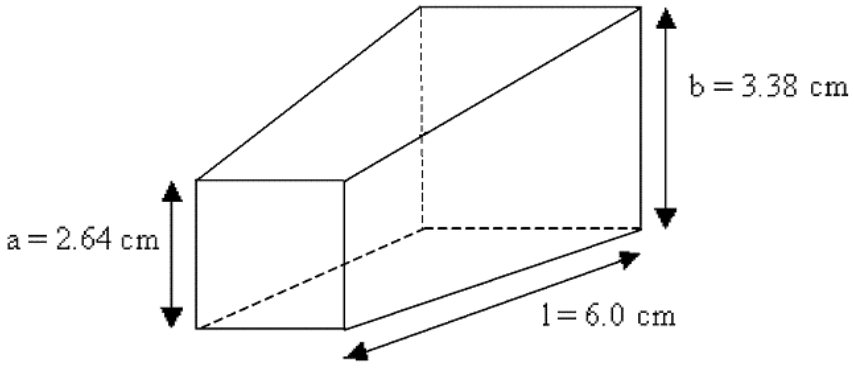

Figure 3.15: The shape of CsI(Tl) crystal.

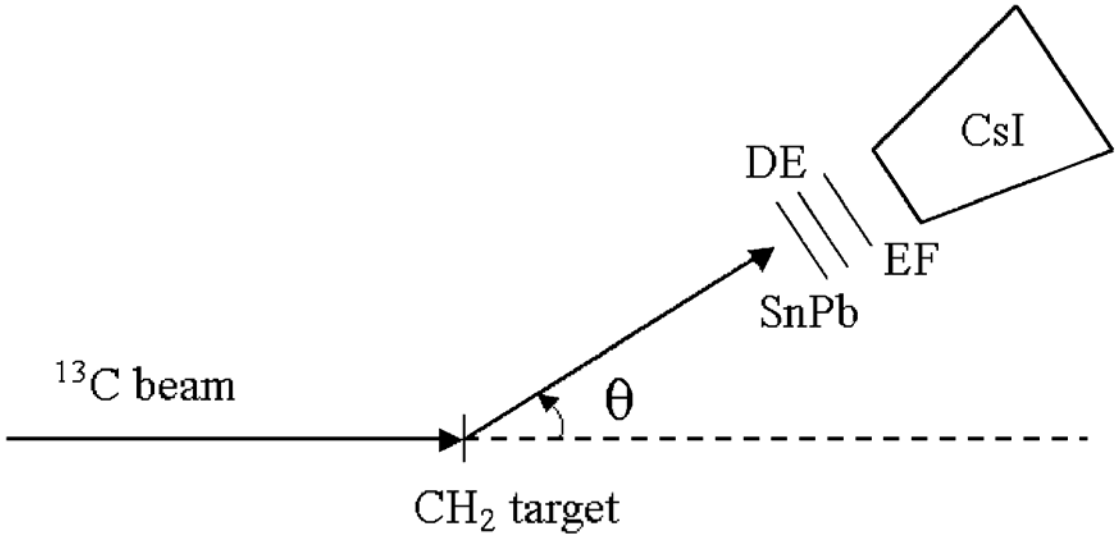

Figure 3.16: Schematic of the CsI calibration. The deuteron emitted angle is determined by the pixel on DE and EF(EB) silicon strip detectors. The deuteron emitted energy is obtained by kinematic calculation. The deuteron deposited its energy into the CsI crystal after going through target, window foil, DE and EF(EB) silicon strip detectors.

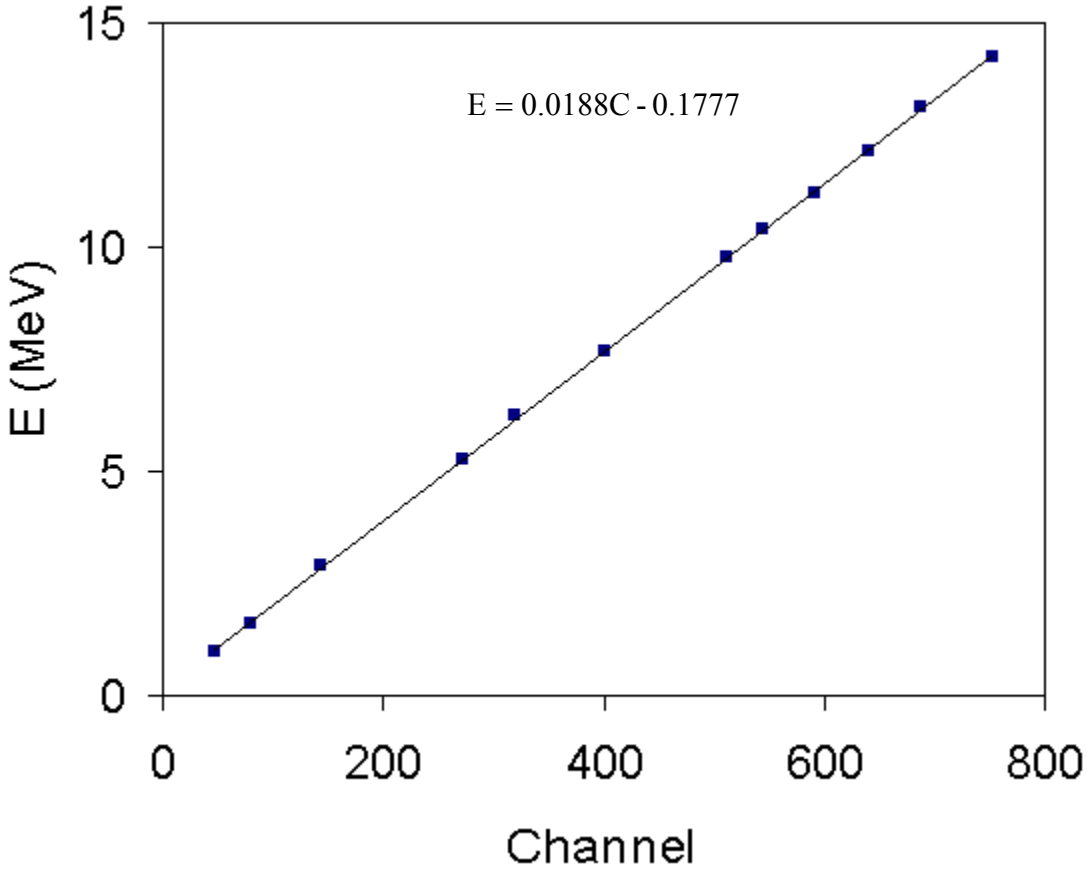

Figure 3.17: Calibration for CsI detector, by which the channel readout of the CsI detector is converted to particle energy in units of MeV. This figure shows the calibration for the No. 3 crystal in telescope 3.

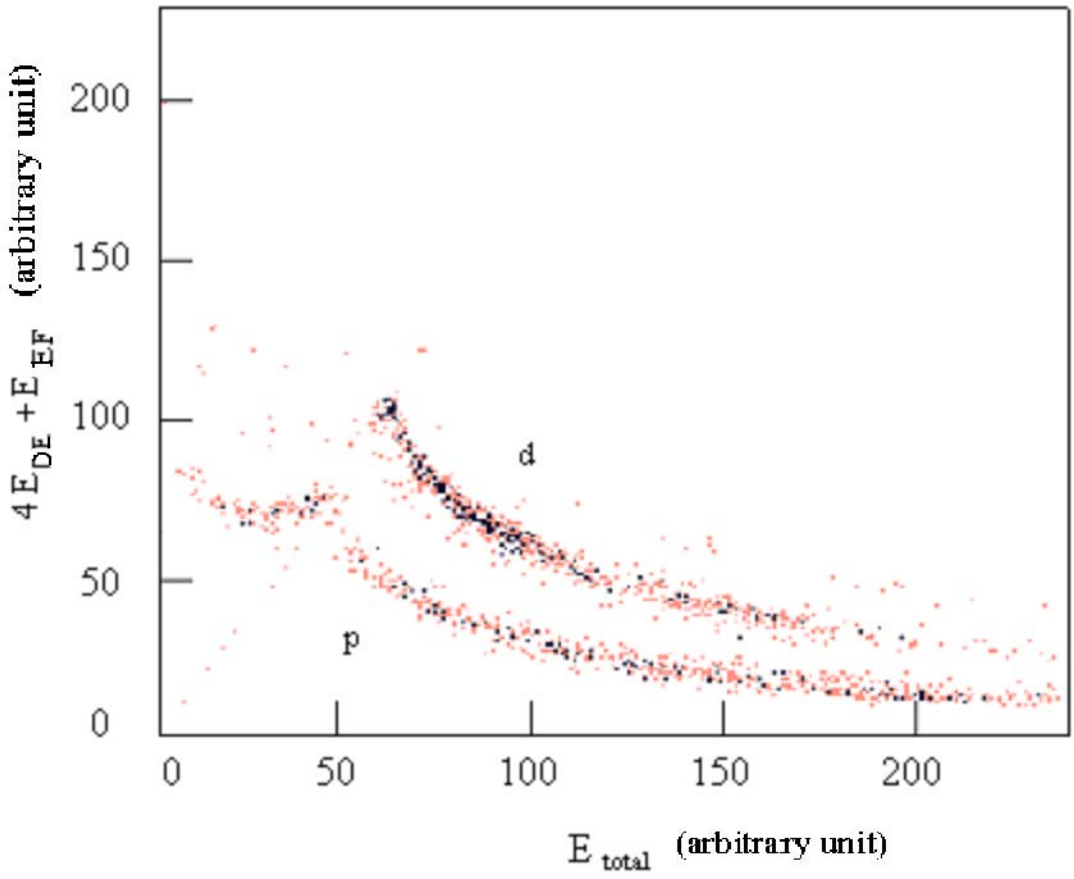

Figure 3.18: Particle identification in the energy spectrum of $4E_{DE} + E_{EF}$ vs. E_{total} for telescope 3.

3.4 S800 Spectrometer

3.4.1 Overview

The working principle of magnetic spectrometer is following: A particle with charge q and mass m, traveling at speed v, passing through a uniform magnetic field with strength **B**, will travel in a circular path with radius ρ given by

$$m\frac{v}{q} = B\rho \tag{3.4.1}$$

Relativistically, the mass is γm, where m is the rest mass and γ is the Lorenz transformation factor. Thus, for a given magnetic field setting, particles with identical momentum to charge ratios are deflected the same amount by the magnet.

A schematic of the S800 spectrometer is shown in Figure 3.2. It stands behind the target chamber and consists of one quadruple doublet, two dipoles, and one focal plane detector. The advantages of S800 spectrometer are the high energy resolution and large solid angle acceptance [Zha97, Yur99, Cag99]. Some of notable characteristics of the S800 spectrometer are listed in Table 3.4.

Figure 3.19 shows the schematic of the focal plane detector of S800. It consists of two Cathode Readout Drift Chambers (CRDC), one ion chamber, and four plastic scintillators. The CRDC detectors measure the two transverse positions and angles of the particles; the ion chamber measures energy loss in the gas; the plastic scintillators measure the particles energies.

The particle flight time is measured relative to the cyclotron radiofrequency (RF) pulses. Different species of particles emitted from the reactions have different velocity,

and hence different flight time to the focal plane. This flight time measurements can then be used in conjunction with the energy loss measurements or total energy measurement to identify the particle species that arrive at the focal plane.

3.4.2 Cathode Readout Drift Counters

The CRDC detectors have an active area of 30 cm × 59 cm and an active depth of 1.5 cm. They are filled to a pressure of 140 Torr with 80% CF_4 and 20% C_4H_{10}. Figure 3.20 shows a schematic illustrating the principles of their operation. Ions traveling through the gas create ionizations. A constant vertical electric field in the detector move the electrons toward an anode wire, where charge amplification takes place in the high electric field close to the wire. The anode wires are placed below a ground Frisch grid and held at a constant voltage, typically 1400 Volts. The electrons are collected on the anode wire. Cathode pads are located in front and back of the anode wires. The charges collected on the anode wire induce positive charges on the cathode pads. There are 224 pads in each CRDC detector. The centroid of the Gaussian fit to the charge distribution is used as the horizontal position in the detector.

The vertical position is determined by the drift time of the electrons to the anode wire. The typical drift time of the electrons to the anode wire is 0-20 μs, depending on their vertical position. Measuring the time between the scintillator signal and the anode wire signal provides a direct vertical position measurement of the particle track.

Masks with well-defined holes and slit patterns as shown in Figure 3.21(a) are placed in front of the CRDC detectors to calibrate the detector positions. Figure 3.21(b) is the

position spectra taken with ^{10}Be beam with the mask placed in front of the first CRDC detector. The position resolution of 0.2 mm is achieved.

3.4.3 Ion Chamber

Immediately following the CRDCs, the beam particles pass through an ionization chamber. The ion chamber (IC) used in the S800 is a standard Frisch grid ion chamber [Yur99]. It is designed to measure the energy loss as the beam particles ionize the gas in the detector by sampling the signal generated along sixteen anode strips. The gas used is P10, which is composed of 90% argon (Ar) and 10% CH_4 (methane). The energy loss in the ion chamber combined with the time-of-flight or the energy deposited in scintillator detectors can provide particle identification.

3.4.4 Plastic Scintillators

There are four plastic scintillators in S800 spectrometer. They are made of BC-408 scintillant plastics manufactured by Bicron [Yur99]. In the order from first to last, with respect to the beam direction, the scintillators are labeled as E1, E2, E3, and E4 in Figure 3.19 with the thickness of 3 mm, 5 cm, 10 cm, and 20 cm respectively. Light guides are mounted on each end to enhance the collection of the light in the photomultiplier tubes (PMT). The light travels through the plastic as well as the light guide and is collected in the PMT's on the top and bottom ends of the scintillator. The energy deposited in the scintillator is calculated by:

$$E_i = \sqrt{E_i^{Up} \times E_i^{Down}} \tag{3.4.2}$$

In the meanwhile, we get the number of particles that enter into S800. We performed normalization run at the beginning of each kind particle beam, when the targets are moved out of the position and the beam particles enter S800 directly. We measure the beam transfer efficiency by the ratio of particle number in S800 to the particle number going through BLT2 scintillator. The normalization procedure will be introduced in Section 4.3.

Since both energy degraded beam particles and the residual particles from the (p,d) reaction enter S800 spectrometer simultaneously, we need to separate them out by the combination of deposited energy in E1 vs. time-of-flight. As an example, Figure 3.22 shows the spectrum of the deposited energy in E1 versus the particle time-of-flight for the reaction of p(^{11}B,d)^{10}B. The residual particle of ^{10}B is separated from the incident beam of ^{11}B.

3.4.5 Summary

Originally, we plan to use S800 spectrometer to detect the recoiled residual nuclei in coincidence with the deuterons detected by LASSA detector to perform complete kinematic measurement. Based on the above analyses, S800 supplies excellent particle position determination via CRDC detectors and good particle identification via the combinations of energy loss in ion chamber, energy deposited in scintillators, and time-of-flight of particles. Unfortunately, there were errors in writing the data from S800 spectrometer onto the tape in this experiment so that some S800 data were lost. In the

present work, the S800 spectrometer was used only for the normalization, when the data from S800 are complete.

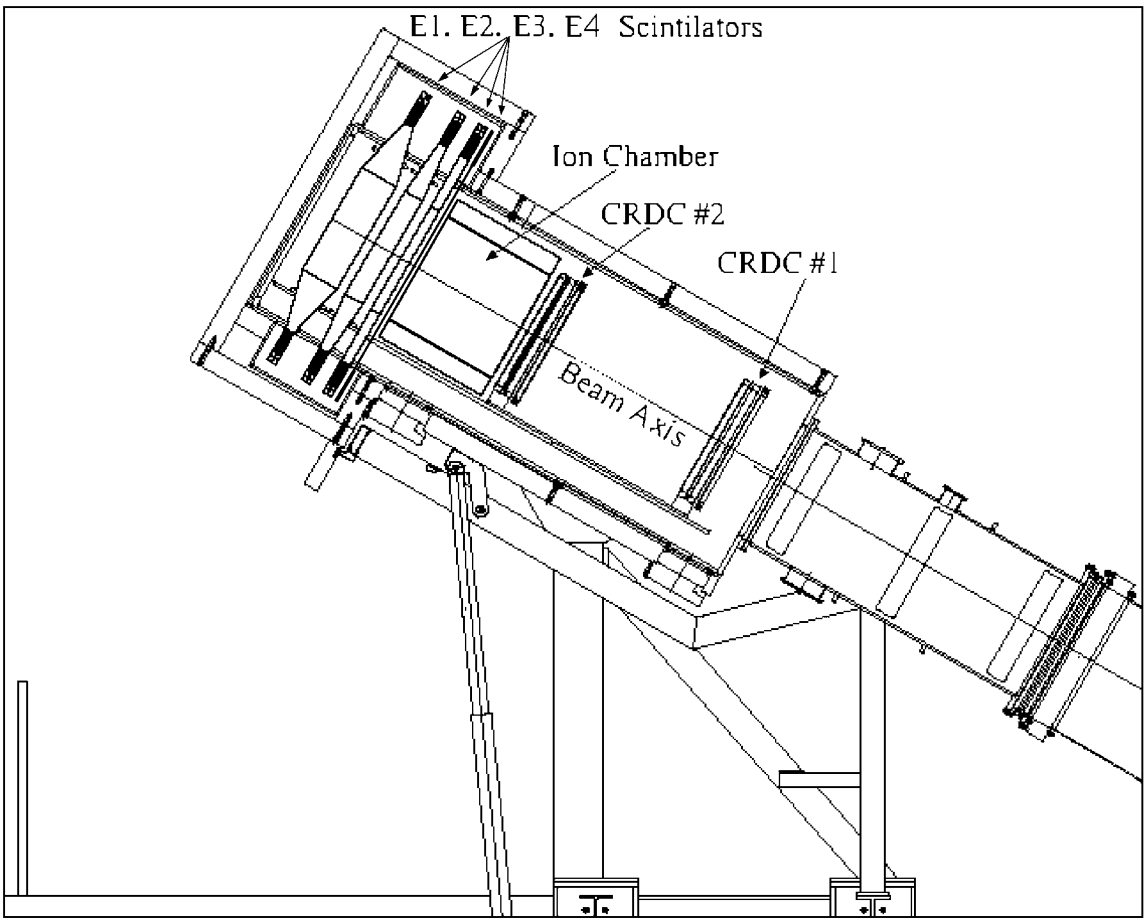

Figure 3.19: Schematic of the focal plane detector of S800 spectrometer. It consists of two CRDC detectors, one ion chamber, and four plastic scintillators.

Table 3.4: Characteristics of the S800 spectrometer

Energy resolution	$\frac{\Delta E}{E} = 10^{-4}$
Momentum resolution	$\frac{\Delta P}{P} = 5 \times 10^{-5}$
Energy range	11.6 %
Momentum range	5.8 %
Solid angle	20 msr
Angular resolution	≤2 mrd
Horizontal detector resolution	0.3 mm
Vertical detector resolution	0.3 mm
Maximum rigidity	4.0 T-m
Maximum dipole field	1.42 Tesla

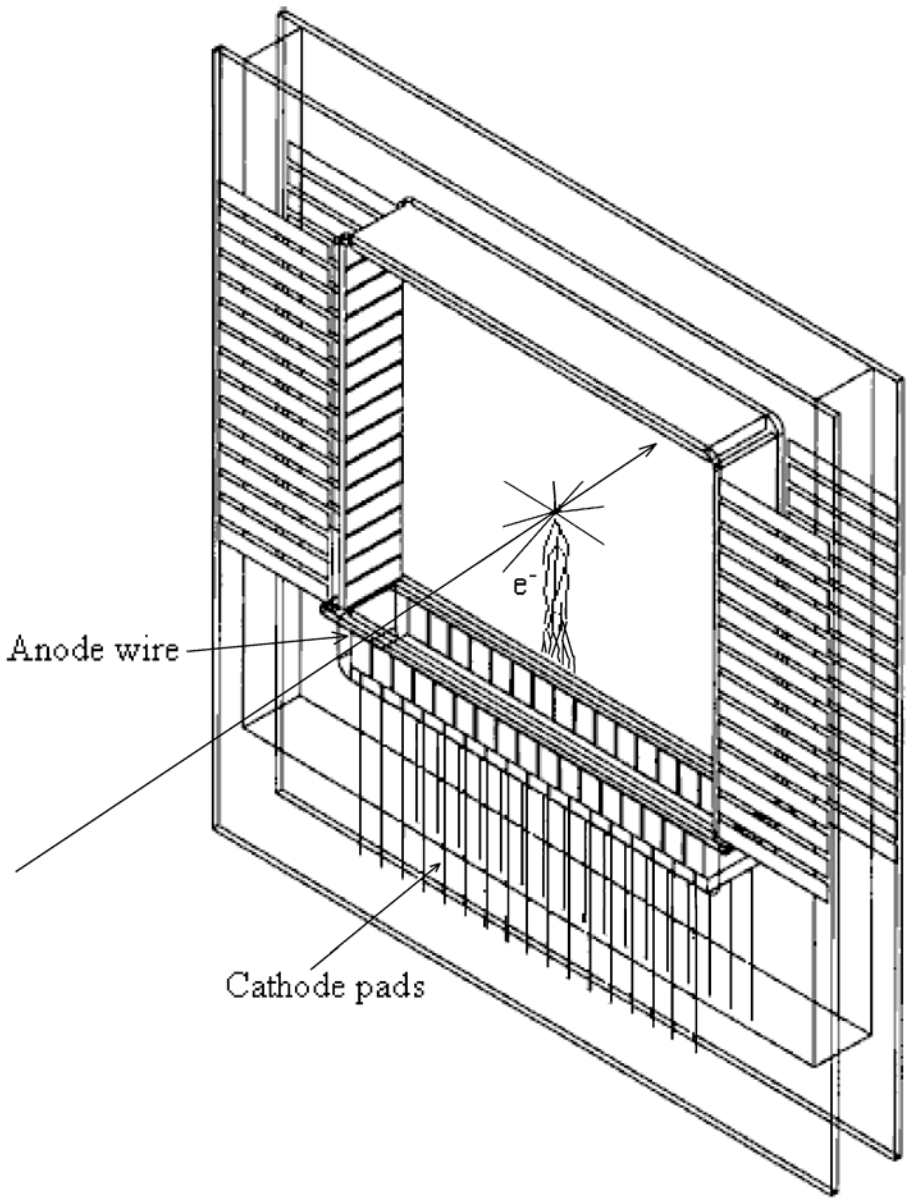

Figure 3.20: Schematic of the CRDC detector. A particle ionizes the gas as it passes through the detector. The electrons drift to the anode wire where they are collected. The induced image charges on the cathode pads provide horizontal position information. The drift time of the electrons to the anode wire provide vertical position information.

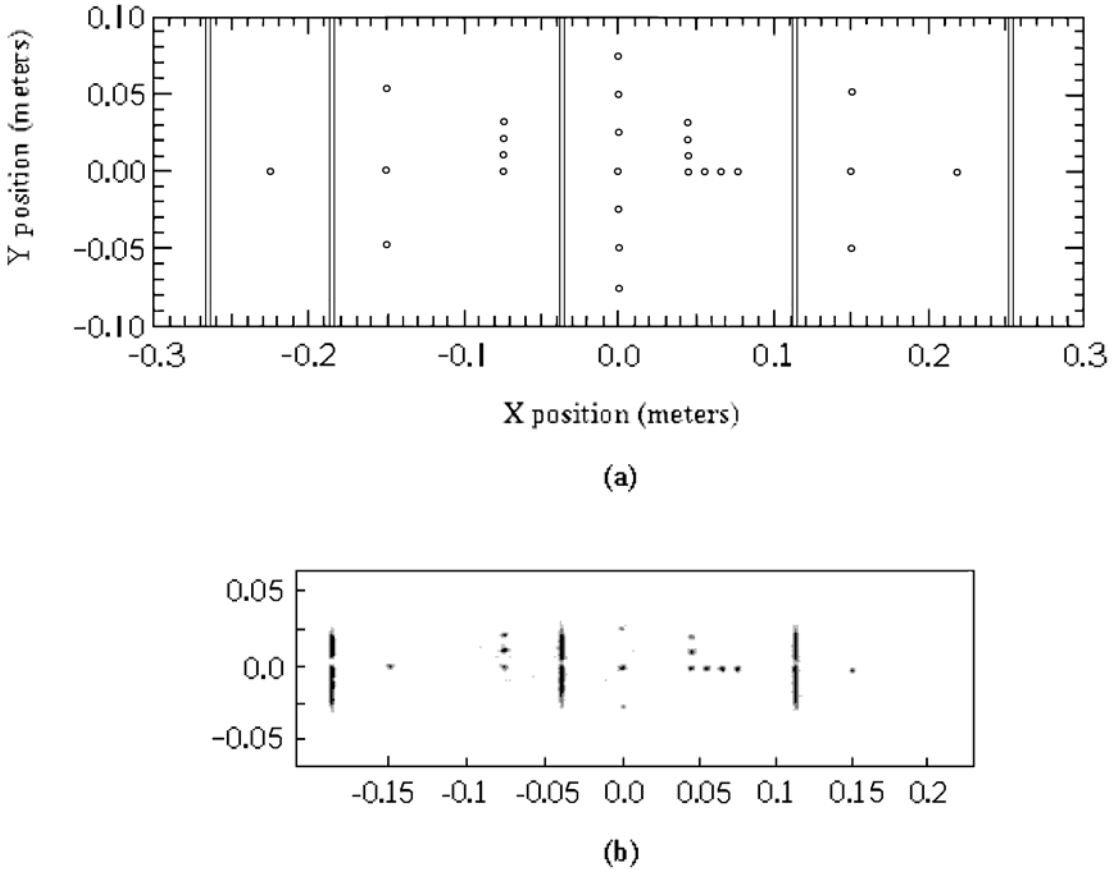

Figure 3.21: (a) Patterns on the mask. (b) Position spectrum of the mask placed in front of the first CRDC detector.

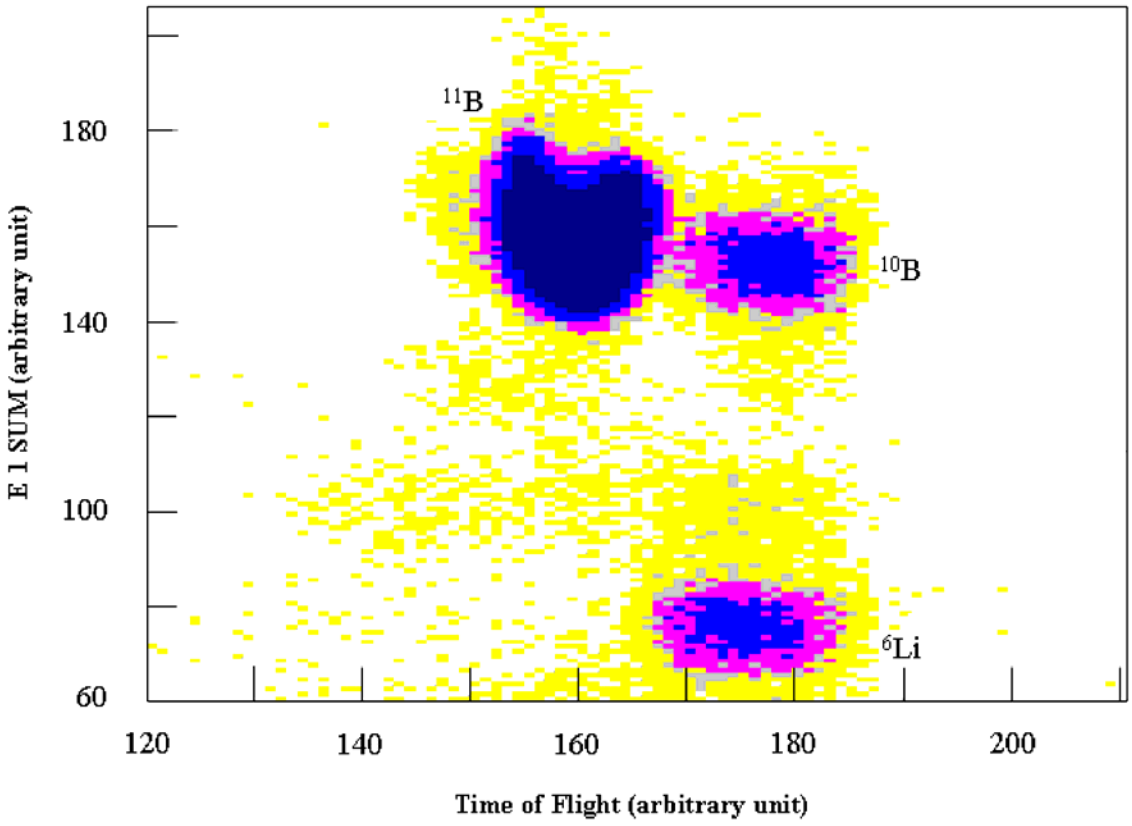

Figure 3.22: Spectrum of the energy deposited in E1 scintillator versus the time-of-flight for the p(^{11}B,d)^{10}B reaction.

3.5 Data Acquisition Electronics

Figure 3.23 is a schematic of the electronics used in this experiment. The signals from the up and down PMT's of the first scintillator E1 are sent to constant fraction discriminator (CFD) module. The outputs of the CFDs are AND-ed to give the S800 premaster signal. The S800 premaster signal and the CFD outputs of the anode wires of CRDC detector are used as the start and stop for the drift time in the CRDCs. The TAC output is input to module of analog-to-digital converter (ADC). The cathode pads are read by the fast encoding and reading ADCs (FERA). The gate for the FERAs is given by the AND of the S800 premaster and the anode pulse.

The signals from the silicon and CsI(Tl) detectors are digitized in Phillips Scientific peak-sensing ADCs (7164H). The signals from the EF silicon strip detectors are sent to Shaper-Discriminator-TFC dual modules. For this module, the shaper outputs are sent to ADCs; the TFC outputs are sent to Lecroy 4300B fast encoding and reading ADCs (FERA) to give the time signals; the trig outputs from all 9 telescopes are OR-ed to give LASSA Premaster signal.

The LASSA Premaster will be AND-ed with S800 premaster to give coincidence Premaster signal. The LASSA Premaster will also be delayed and downscaled to give LASSA trigger signal.

The Master signal is logically AND-ed with the $\overline{Busy}$ signal from the computer, coincidence Premaster, S800 premaster, and LASSA trigger. The Master signal is the start signal to the computer and stop signal for the TFC. The gates for the modules of ADCs and FERAs are also supplied by the Master signal.

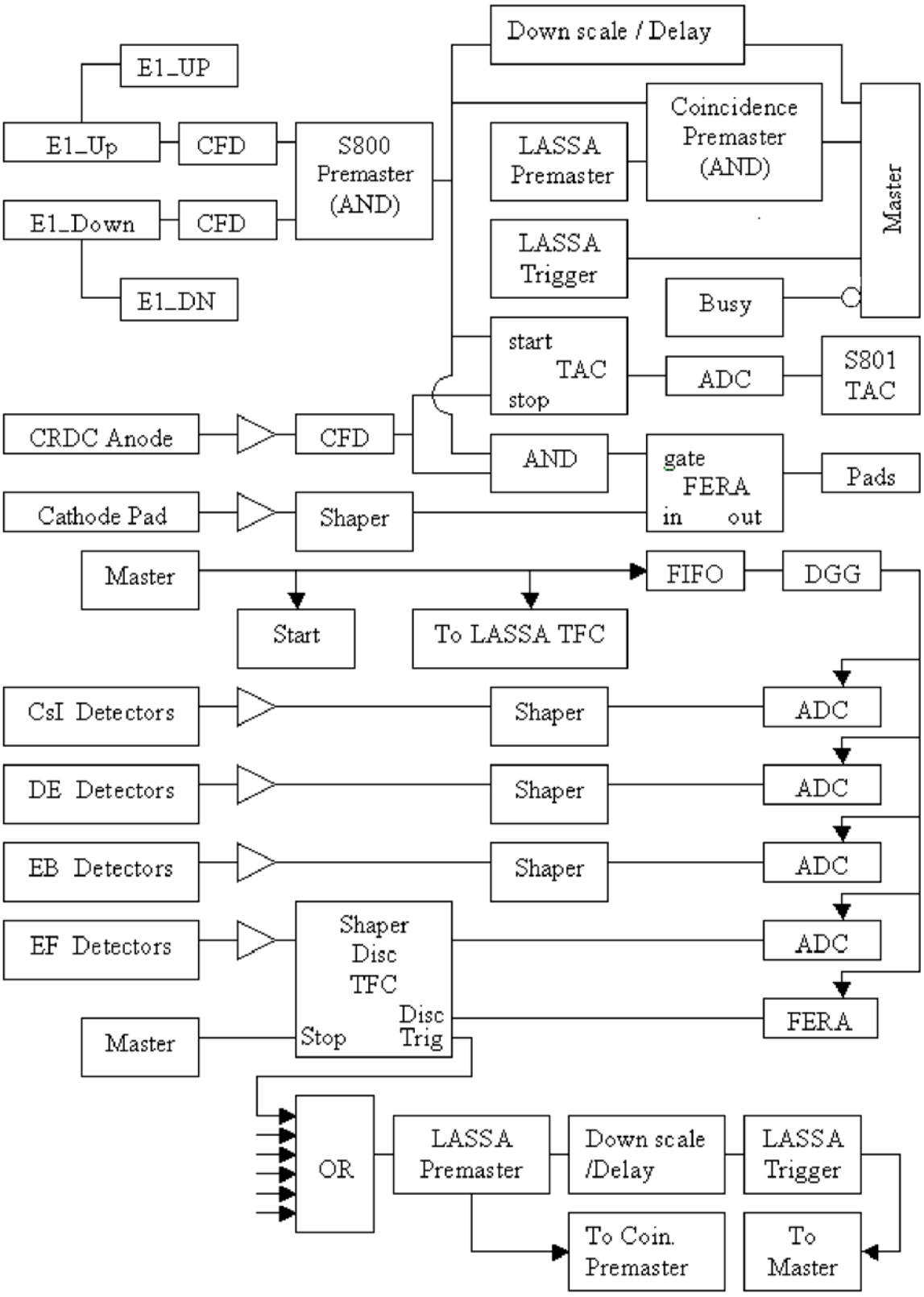

Figure 3.23: Schematic of the electronics.

CHAPTER 4

EXTRACTION OF ANGULAR DIFFERENTIAL CROSS SECTIONS

4.1 Overview

This chapter will discuss the extraction of the deuteron spectra and analyze the contributions to the energy resolution in Section 4.2. In section 4.3, the procedure to extract the differential cross sections will be introduced and the measured data are presented.

4.2 Deuteron Spectra

Applying the PID gates obtained in Section 3.3, we can pick out the deuterons and obtain their energies in laboratory frame via Equation 3.3.2 and Equation 3.3.8 for silicon strip detectors and CsI(Tl) crystal detectors respectively. The deuteron energy in the center of mass is obtained by converting the measured deuteron energy in the laboratory frame to the center of mass frame.

$$E_{cm} = \frac{1}{2}mV^2 + \frac{1}{2}mV_0{}^2 - mV\,V_0\cos\theta \qquad (4.2.1)$$

where m is the deuteron mass, V is the deuteron velocity, V_0 is the velocity of the center of mass, and θ is the emitted angle of deuteron. Figure 4.1 shows the deuteron energy spectrum of the p(^{13}C,d)^{12}C reaction at the laboratory angle of 19°. The peaks of ground

state (0^+) and first excited state 4.439 MeV (2^+) can be distinguished clearly. The peaks at 7.654 MeV (0^+) and 12.71 MeV (1^+) do not have enough statistics but still can be identified. The peaks at 15.11 MeV (1^+) and 15.44 MeV (2^+) cannot be resolved completely.

To estimate the full width at half maximum (FWHM) of the peaks in the laboratory frame ΔE_L, we need to take into account that the emitted deuterons emitted from the reactions have to go through the remainder of the target and the SnPb foil before reaching the Si detectors.

$$\Delta E_L = \sqrt{\Delta E_{tar}{}^2 + \Delta E_{SnPb}{}^2 + \Delta E_\theta{}^2} \qquad (4.2.2)$$

where ΔE_{tar} is the rms width of the deuteron energy loss distribution in the target, ΔE_{SnPb} is the deuteron energy straggling in the SnPb foil, and the ΔE_θ is the kinematic broadening due to the angular resolution of the strip detectors. ΔE_{tar} is larger than the width given by energy loss straggling because of the variation of energy loss in the target depend on how much of the target is traversed before the reaction occurs. The beam broadening and the beam straggling in the target are not included in Equation 4.2.2 because they contribute little to the deuteron resolution. The FWHM in the center of mass derived from Equation 4.2.1 is

$$\Delta E_{cm} = \Delta E_L - mV_0 \cos\theta \cdot \Delta V_L + mV_L V_0 \sin\theta \cdot \Delta\theta \qquad (4.2.3)$$

where $\Delta\theta$ is the angular accuracy of pixelation (±0.1°), ΔV_L is the FWHM of deuteron velocity in laboratory frame. Table 4.1 lists the contributions to deuteron resolution. The energy straggling are calculated by the program SRIM [Srim]. The energy broadening

ΔE_θ due to the angular resolution and the energy loss in the target contribute most to the final energy resolution. The experimental FWHM for the peaks of 0.0 MeV and 4.439 MeV are 800 keV. The estimated energy resolutions are pretty close to the measured ones.

Figure 4.2 shows the deuteron spectrum of the $p(^{11}B,d)^{10}B$ reaction at the laboratory angle of 13°. The energy resolutions are about 640 keV for the ground state and the first excited state at 1.74 MeV. The other states cannot be evaluated because of low statistics. From Table 4.1, we see again that the kinematic broadening due to the angular resolution and the energy loss in target contribute most to the energy resolution. A smaller kinematic broadening and a thinner target will result in a better energy resolution.

Figure 4.3 shows the deuteron spectrum of the $p(^{10}Be,d)^{9}Be$ reaction at the laboratory angle of 15°. The energy resolution is 800 keV for the ground state. The excited states cannot be distinguished because of low statistics. Contributions to the energy resolution are also listed in Table 4.1.

4.3 Extraction of Angular Differential Cross Sections

Before the extraction of the angular differential cross sections, we need to know the beam transfer efficiency f and the total beam particles N_{par} that hit the target. The beam transfer efficiency is measured in a normalization run at the beginning of each experiment, where the target is moved out of the beam line. The beam particle delivered before the target is measured by the BLT2 scintillator and the beam particle through the target is measured by the E1 scintillator of S800 spectrometer. The beam transfer efficiency is:

$$f = \frac{N_{E1}}{N_{BLT2} \cdot R_{LT}} \tag{4.3.1}$$

where R_{LT} is the life time of the data acquisition system. The total beam particles that hit the target N_{par} are calculated by the summation over all the runs:

$$N_{par} = \sum_i N_{BLT2}{}^i \cdot R_{LT}{}^i \cdot f \tag{4.3.2}$$

where $N_{BLT2}{}^i$, and $R_{LT}{}^i$ are the number of particle detected by the BLT2 scintillator and the life time of the data acquisition system for each experimental run, *i*.

The angular differential cross section in the laboratory frame is obtained for each telescope individually:

$$\left(\frac{d\sigma}{d\Omega}\right)_{\theta_L}^{i} = \frac{N_d}{d\Omega_L \cdot N_{tar} \cdot N_{par}} \tag{4.3.3}$$

where i denotes individual telescope, θ_L is the angle in the laboratory frame, N_d is the number of deuterons detected in the interval of ±1.0° relative to θ_L, $d\Omega_L$ is the solid angle in the laboratory frame, and N_{tar} is the target thickness in number of hydrogen atoms per centimeter square. The statistical error for each telescope is calculated by

$$\Delta\left(\frac{d\sigma}{d\Omega}\right)_{\theta_L}^{i} = \left(\frac{d\sigma}{d\Omega}\right)_{\theta_L}^{i} \cdot \frac{1}{\sqrt{N_d}} \tag{4.3.4}$$

The average angular differential cross section and statistical error are obtained by

$$\left(\frac{d\sigma}{d\Omega}\right)_{\theta_L} = \frac{\sum \frac{\left(\frac{d\sigma}{d\Omega}\right)_{\theta_L}^{i}}{\left[\Delta\left(\frac{d\sigma}{d\Omega}\right)_{\theta_L}^{i}\right]^2}}{\sum\left[\Delta\left(\frac{d\sigma}{d\Omega}\right)_{\theta_L}^{i}\right]^{-2}} \tag{4.3.5}$$

$$\Delta\left(\frac{d\sigma}{d\Omega}\right)_{\theta_L} = \sqrt{\frac{1}{\sum\left[\Delta\left(\frac{d\sigma}{d\Omega}\right)_{\theta_L}^{i}\right]^{-2}}} \tag{4.3.6}$$

The angular differential cross section and statistical error in the center of mass are

$$\left(\frac{d\sigma}{d\Omega}\right)_{\theta_{cm}} = \gamma \cdot \left(\frac{d\sigma}{d\Omega}\right)_{\theta_L}$$

$$\Delta\left(\frac{d\sigma}{d\Omega}\right)_{\theta_{cm}} = \gamma \cdot \Delta\left(\frac{d\sigma}{d\Omega}\right)_{\theta_L} \tag{4.3.7}$$

$$\gamma = \frac{\left|1 + \frac{m_1}{m_2}\cos\theta_{cm}\right|}{\left(1 + \frac{{m_1}^2}{{m_2}^2} + 2\frac{m_1}{m_2}\cos\theta_{cm}\right)^{\frac{3}{2}}}$$

where γ is the ratio of $d\Omega_L / d\Omega_{cm}$, m_1 and m_2 are the mass of projectile and target nuclei.

For the p(^{13}C,d)^{12}C reaction, the angular differential cross sections to ground state and first excited state at 4.439MeV have been extracted. For the reaction of p(^{11}B,d)^{10}B and p(^{10}Be,d)^{9}Be, only the angular differential cross sections to the ground state have been extracted because of the low statistics of the excited states. The data and the statistical errors are listed in Table 4.2.

The open red symbols in Figure 4.4 show our measured angular differential cross sections of p(^{13}C,d)^{12}C (g.s.) reaction. It is compared to the published data of Ref. [Cam87] at proton energy of 41.3 MeV (solid red circles). There are additional data in Ref. [Sco70] at proton energy of 50 MeV. However, the latter set of data was published in arbitrary unit. We match Scott's data [Sco70] at 12.1° to the data of this measurement and get the normalization factor of 2.45. The three sets of data show fairly good agreement especially when the difference in beam energies is taken into consideration.

Figure 4.5 shows the comparison of the differential cross section of p(^{13}C,d)^{12}C to the first excited state from our measurement (open circle), data of ref. [Cam87] (closed red circles), and data from ref [Sco70] (diamonds) with the same normalization factor of 2.45. Again, our data agree with the past measurements fairly well suggesting that the experimental procedures we used for measuring angular distributions for inverse kinematic reactions with high resolution strip detectors work rather well.

Figure 4.6 shows the angular differential cross sections of p(^{11}B,d)^{10}B (g.s.). Unfortunately, the ^{11}B data were taken with relatively short time so that the total statistics we have collected are low. Only telescopes 1, 2, 3, and 7 yield significant counts to the measurements. The measured data have large error bars.

Figure 4.7 shows the angular differential cross section of p(^{10}Be,d)^{9}Be to the ground state. However, we have problem with the absolute normalization. In this particular reaction, the S800 trigger some time did not fire. When that happens, the LASSA trigger fired alone but with a downscale factor of 5. We have to add the events by S800 trigger together with 5 times of the events by LASSA trigger. This problem only happened in the beam of ^{10}Be. We still do not understand the reason of this problem thus there are unresolved questions about the absolute value of the cross section.

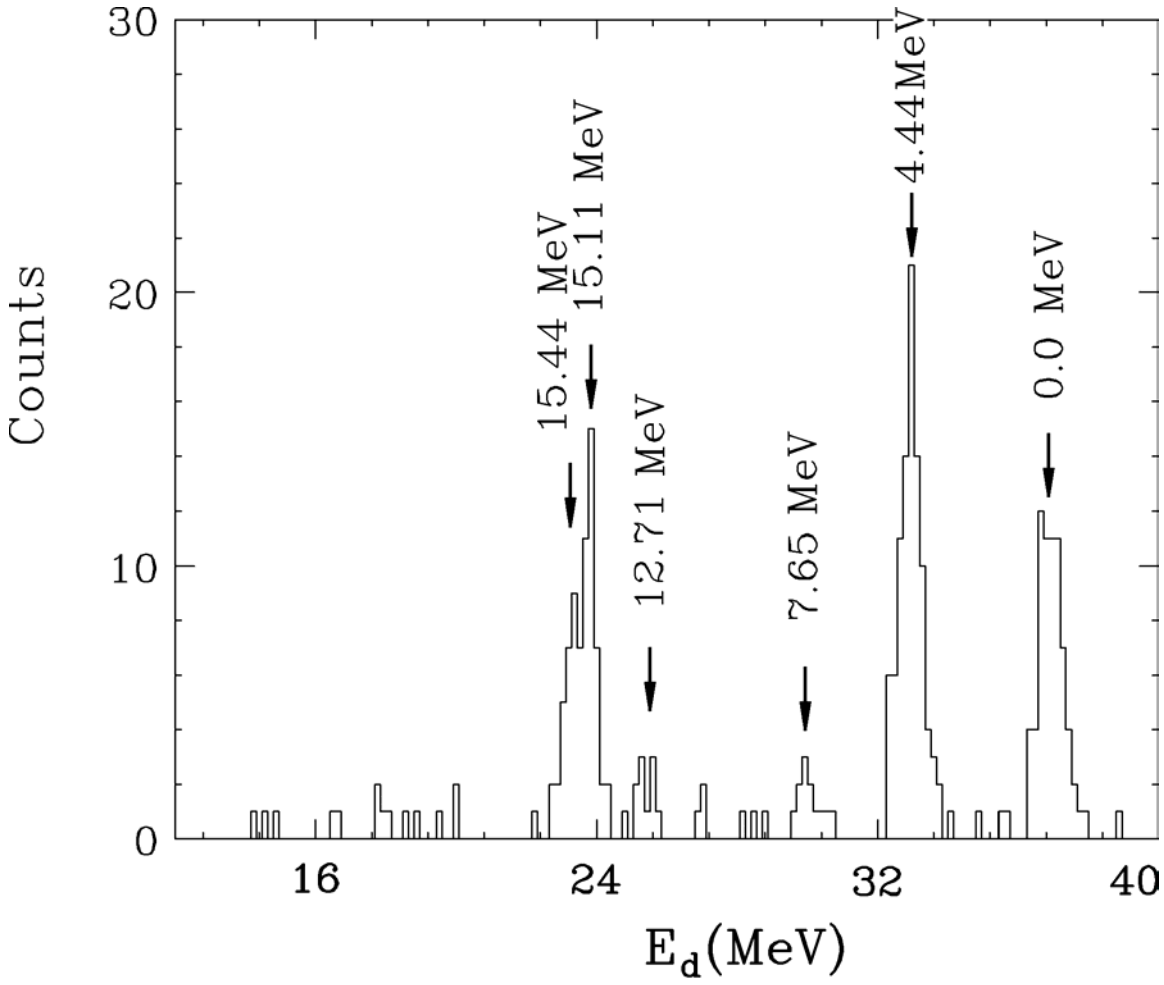

Figure 4.1: Deuteron energy spectrum of the p(^{13}C,d)^{12}C reaction at the laboratory angle of 19° measured by telescope 7.

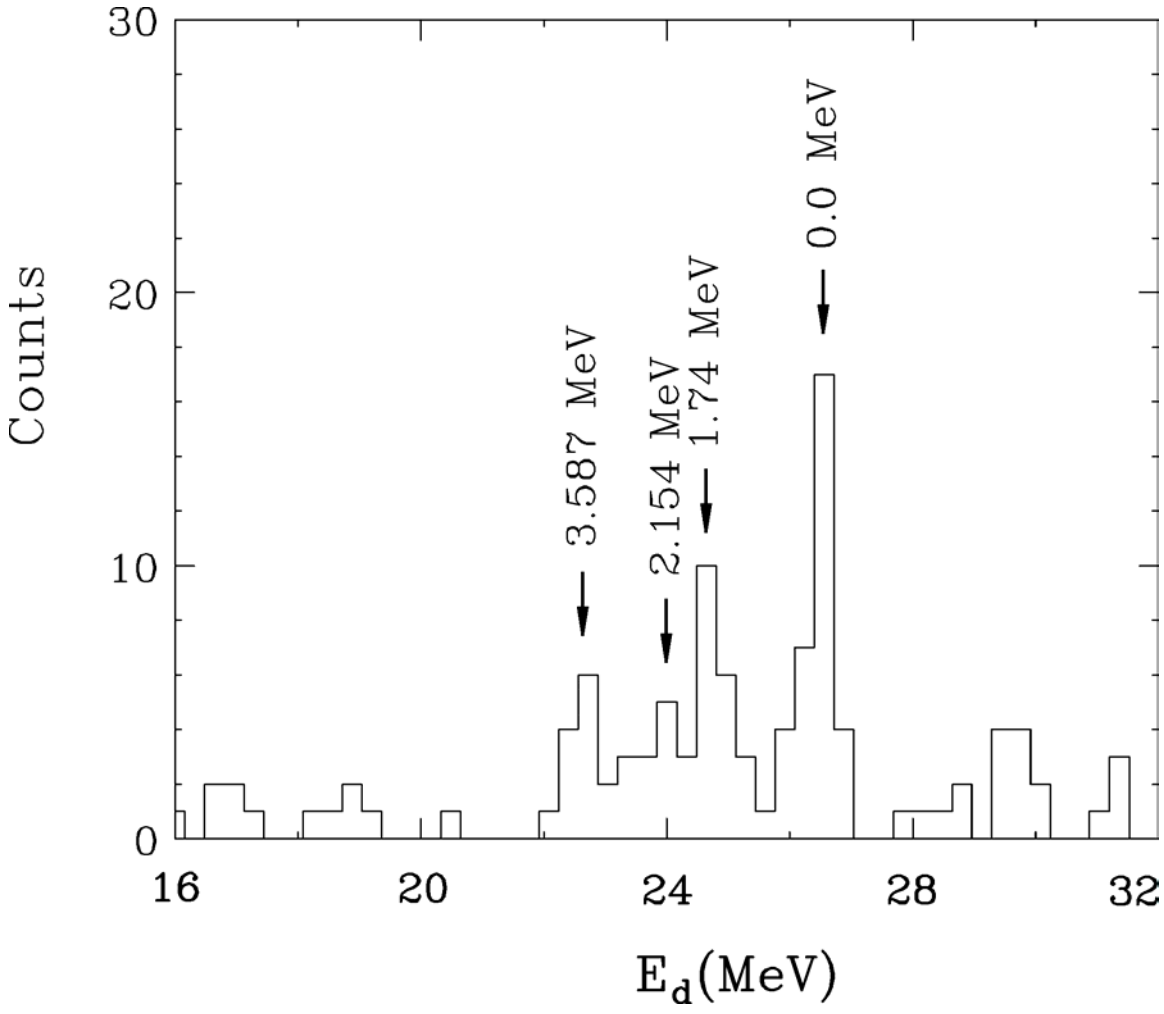

Figure 4.2: Deuteron energy spectrum of p(^{11}B,d)^{10}B reaction at the laboratory angle of 13° measured by telescope 7.

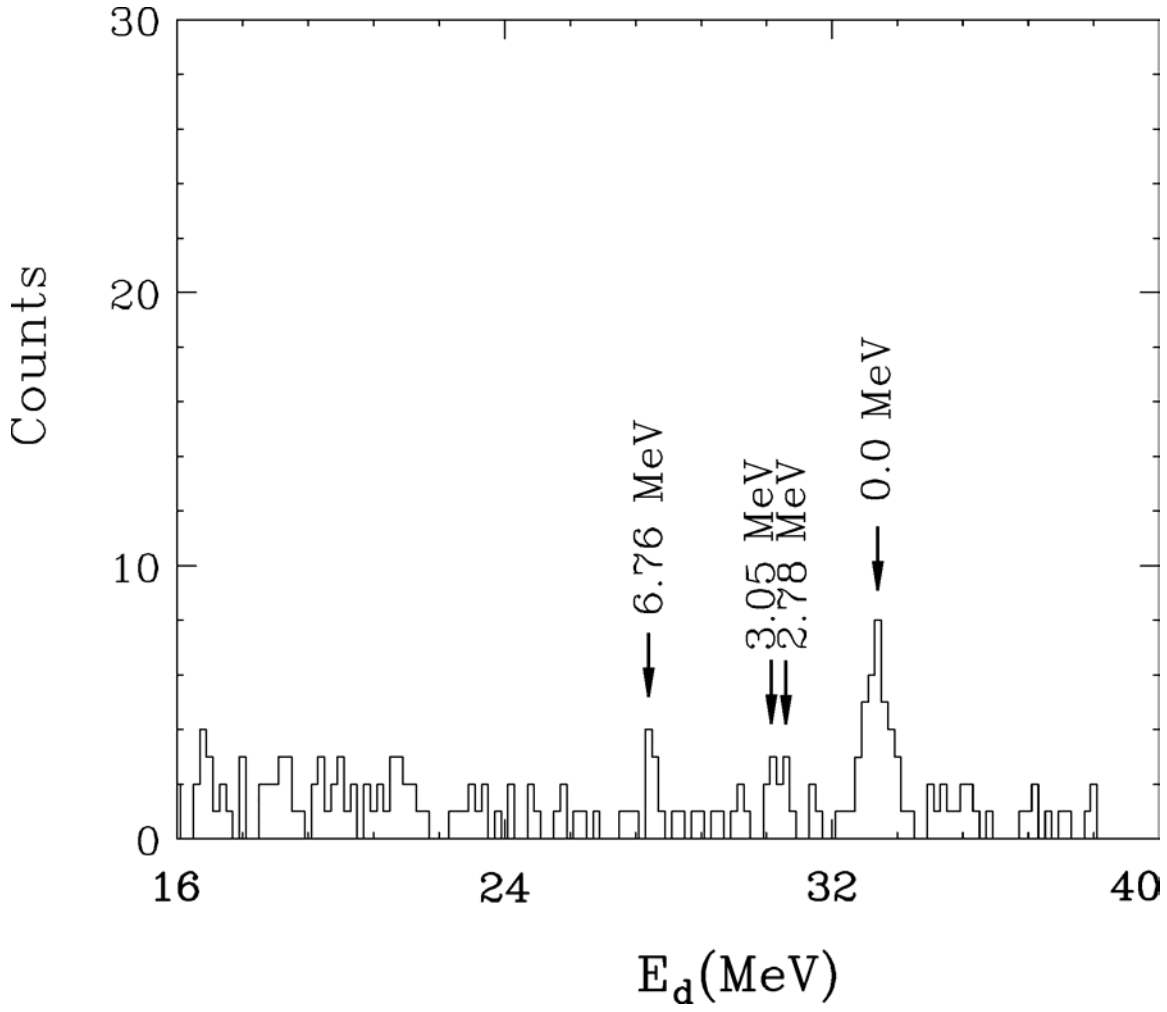

Figure 4.3: Deuteron energy spectrum of p(^{10}Be,d)^{9}Be reaction at the laboratory angle of 15° measured by telescope 7.

Table 4.1: Contributions to the energy resolution of the single neutron pickup reactions in inverse kinematics.

Beam	Level (MeV)	Level width Γ (eV)	θ_{Lab}	Energy loss in target $\Delta E_{d\text{-}tar}$ (keV)	Energy straggling in SnPb foil ΔE_{foil} (keV)	Energy broadening ΔE_{θ} (keV)	Estimated FWHM in Lab. frame ΔE_{L} (keV)	Estimated FWHM in center of mass ΔE_{cm} (keV)	Measured FWHM in center of mass ΔE_{exp} (keV)
^{13}C	0.0 (0^+)	0.0	19.0	305	33	195	364	672	800
	4.439 (2^+)	0.01	19.0	257	40	263	370	586	800
^{11}B	0.0 (3^+)	0.0	13.0	178	38	165	246	417	640
	1.74 (0^+)	0.09	13.0	164	40	187	252	398	640
^{10}Be	0.0 ($\frac{3}{2}^-$)	0.0	15.0	291	35	161	334	610	800

Table 4.2 Experimental angular differential cross sections and statistical errors

(a)

$p(^{13}C,d)^{12}C$, E_x= 0.0 MeV		
θ_{cm} (deg)	$\frac{d\sigma}{d\Omega}$ (mb/sr)	$\Delta\frac{d\sigma}{d\Omega}$ (mb/sr)
4.0	11.54	1.07
5.2	11.48	1.19
6.4	11.88	1.59
7.7	11.09	1.80
8.9	10.07	0.58
10.2	9.60	0.49
11.6	8.70	0.61
13.0	7.85	0.45
14.5	6.68	0.41
16.1	5.39	0.37

(b)

$p(^{13}C,d)^{12}C$, E_x= 4.439 MeV		
θ_{cm} (deg)	$\frac{d\sigma}{d\Omega}$ (mb/sr)	$\Delta\frac{d\sigma}{d\Omega}$ (mb/sr)
7.5	7.19	1.04
8.9	8.74	1.51
10.4	9.54	0.45
11.9	9.20	0.40
13.6	8.33	0.45
15.3	7.35	0.31
17.1	6.08	0.27
19.1	4.87	0.26

(c)

$p(^{11}B,d)^{10}B$, E_x= 0.0 MeV		
θ_{cm} (deg)	$\frac{d\sigma}{d\Omega}$ (mb/sr)	$\Delta\frac{d\sigma}{d\Omega}$ (mb/sr)
6.8	6.12	1.49
8.4	6.73	1.28
10.0	7.59	1.27
11.7	8.44	1.16
13.5	7.45	1.2
15.4	6.84	1.25

(d)

$p(^{10}Be,d)^{9}Be$, E_x= 0.0 MeV		
θ_{cm} (deg)	$\frac{d\sigma}{d\Omega}$ (mb/sr)	$\Delta\frac{d\sigma}{d\Omega}$ (mb/sr)
3.2	27.40	5.27
4.4	27.06	4.20
7.1	27.95	6.04
9.8	26.18	1.96
11.3	22.91	3.51
12.8	19.43	3.80
14.4	16.68	1.70
16.1	12.89	1.18
17.9	10.98	1.24

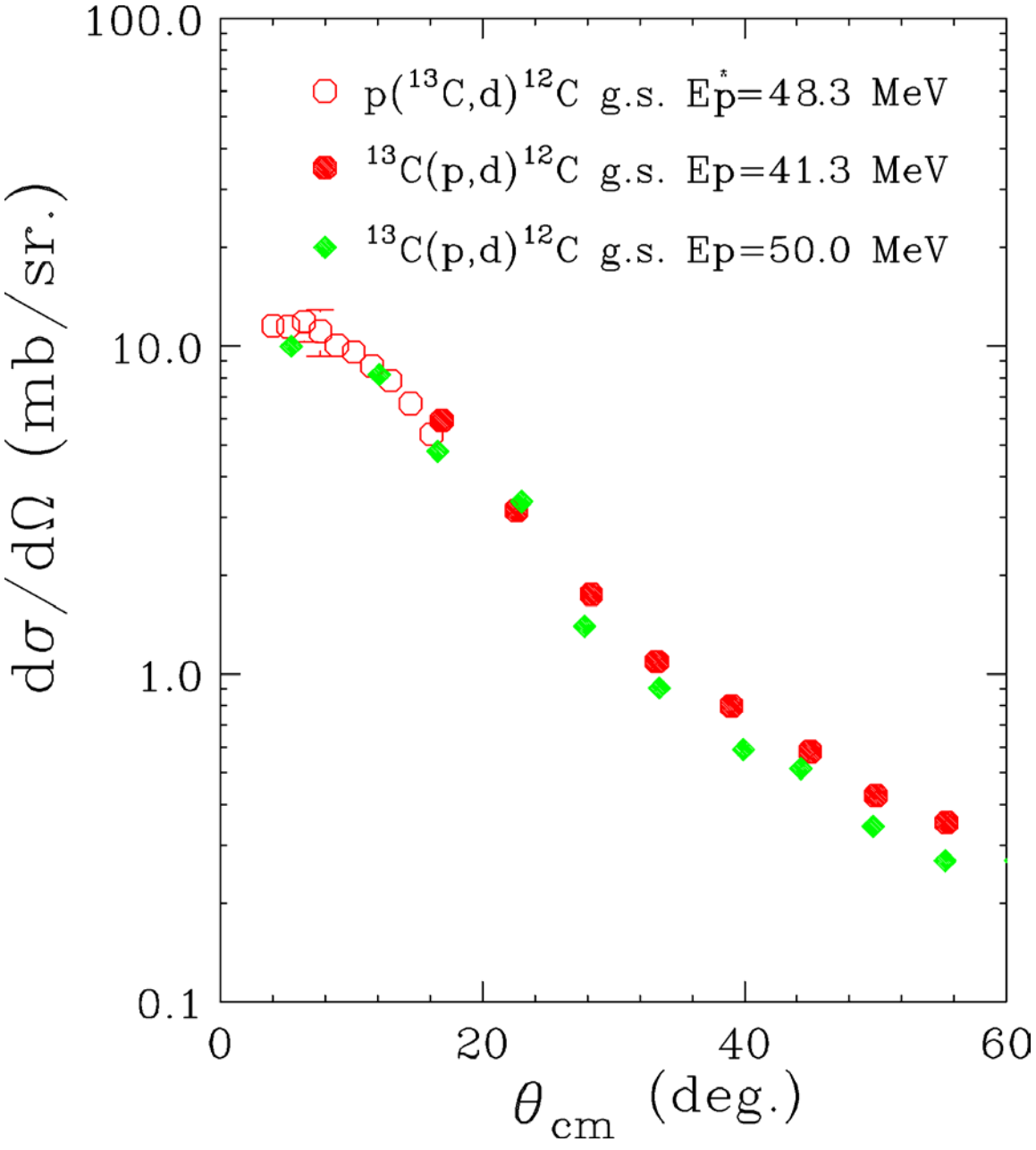

Figure 4.4: The measured angular differential cross section of p(^{13}C,d)^{12}C (g.s.) (open circle) reaction compared to the published data of Ref. [Cam87] (closed circle) and Ref. [Sco70] (diamonds).

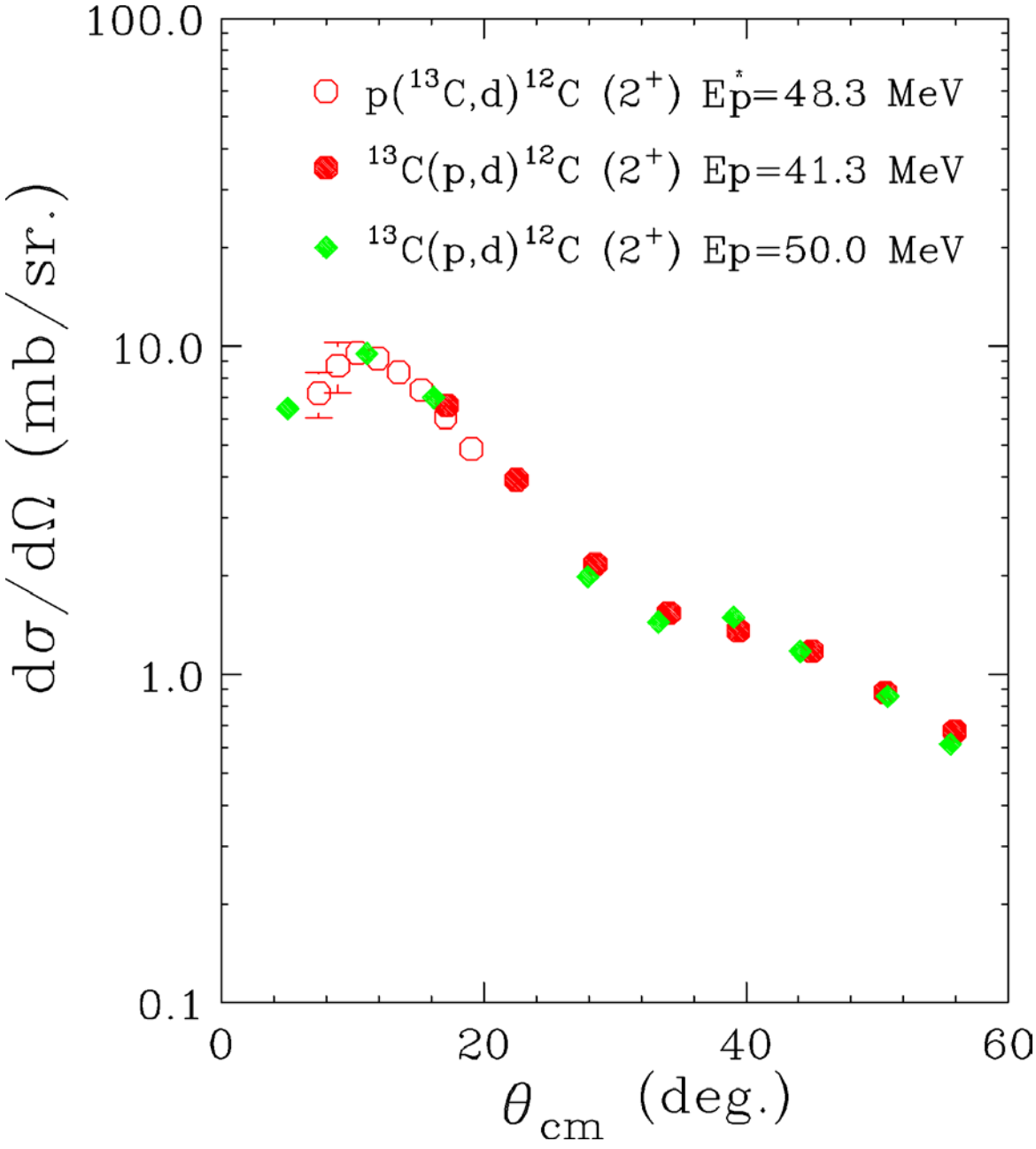

Figure 4.5: The measured angular differential cross section of p(^{13}C,d)^{12}C (2^+) (open circle) reaction compared to the published data of Ref. [Cam87] (closed circle) and Ref. [Sco70] (diamonds).

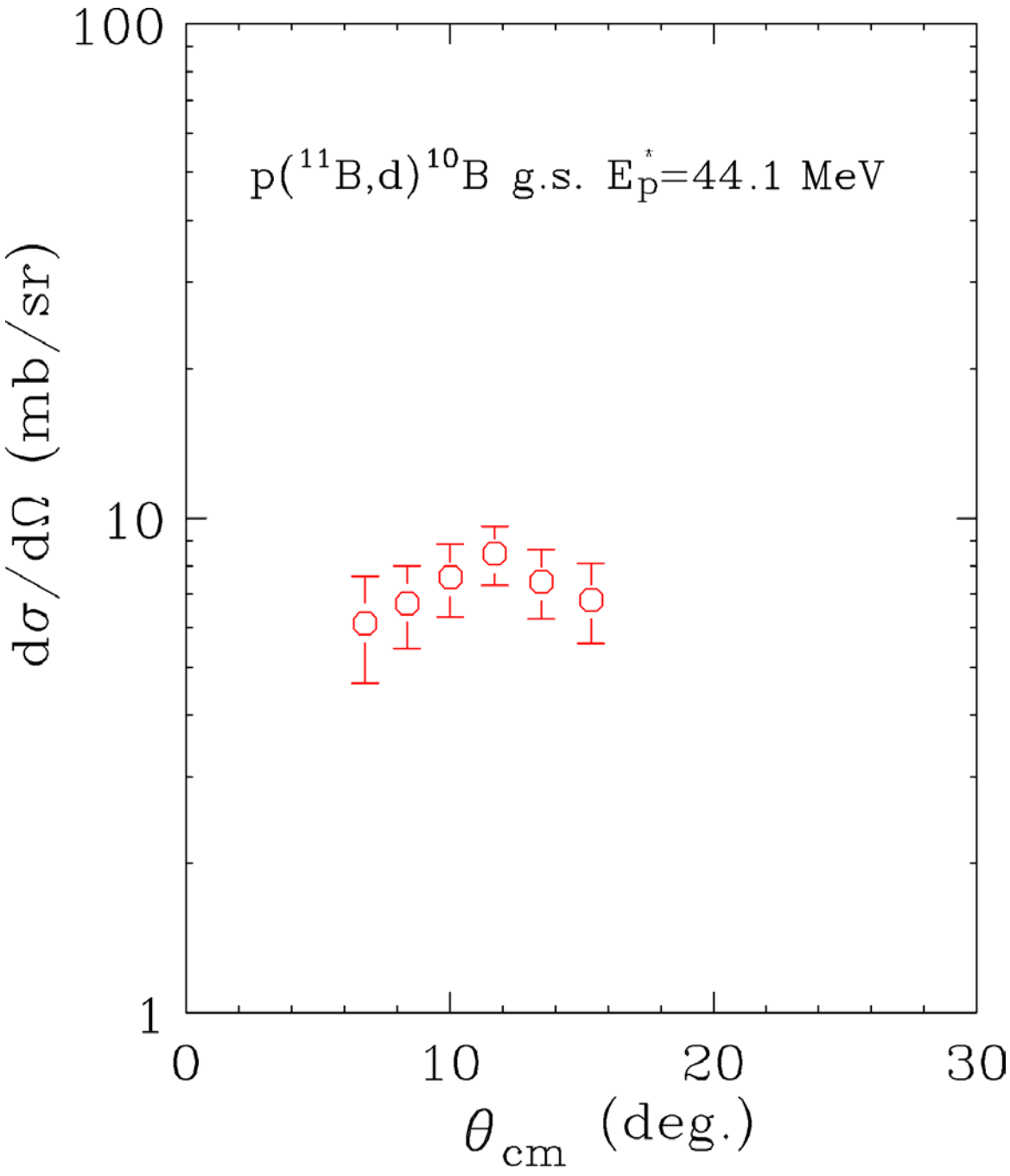

Figure 4.6: The measured angular differential cross section of p(^{11}B,d)^{10}B (g.s.) reaction.

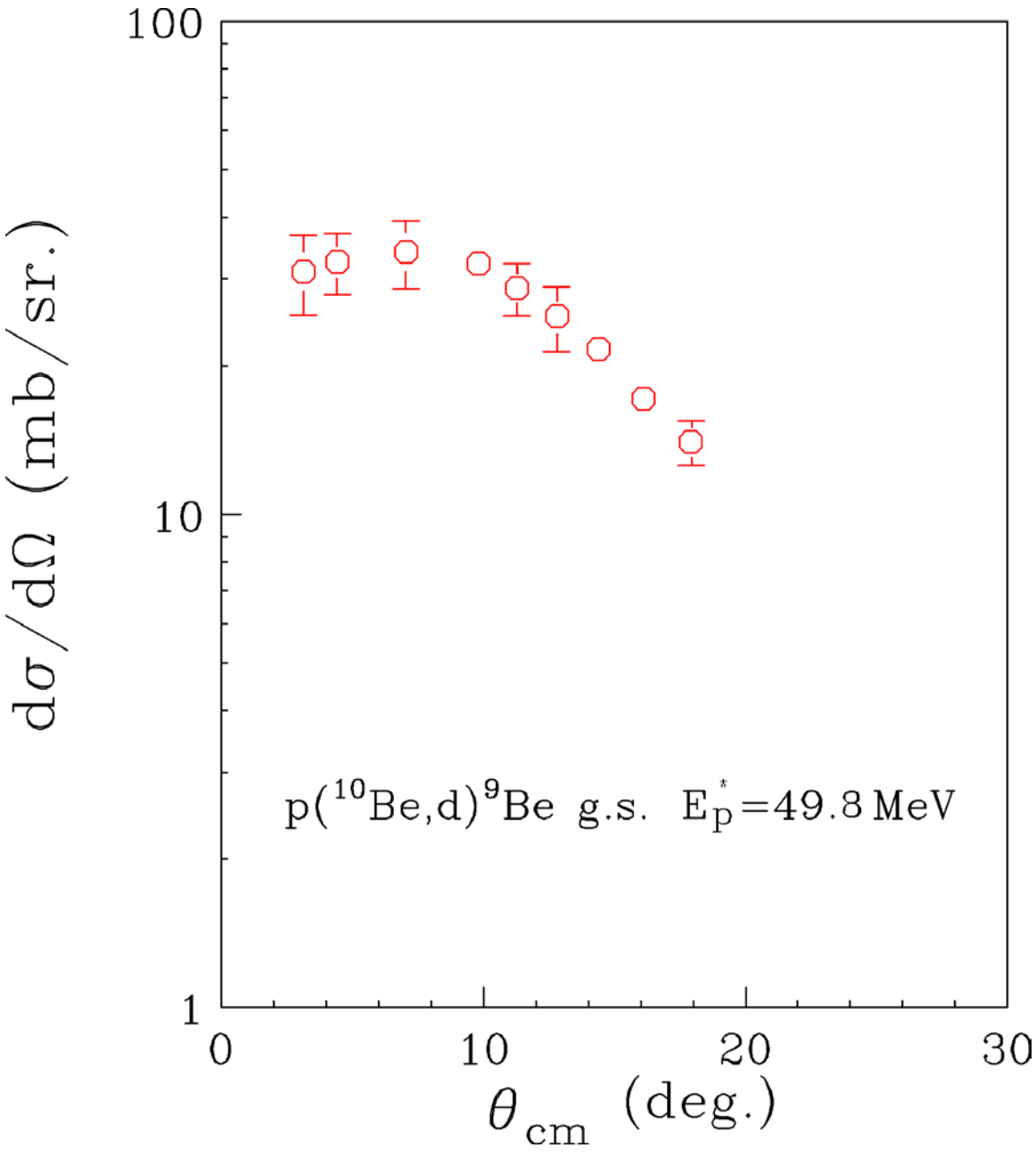

Figure 4.7: The measured angular differential cross section of p(^{10}Be,d)^{9}Be (g.s.) reaction.

CHAPTER 5

EXTRACTION OF SPECTROSCOPIC FACTORS

5.1 Overview

Single-nucleon transfer reactions, such as the (d,p) and (p,d) processes, have been used extensively to study the spectroscopy of nuclei [But51, Mac60, Aus70, Mac74, Sat83, Cat02], in particular for the extraction of single-nucleon spectroscopic factors (SF). The SF is obtained by taking the ratio of the measured cross section to that calculated using a reaction model [Mac60, Mac74]. Theoretically, the spectroscopic factor can be considered as the overlap integral between the initial and final state of the target nuclei and yield information on the occupancy of a given single-particle orbit [Mac60, Mac74, Sat83].

The properties of rare isotopes far away from the valley of stability are very important in the study of astrophysics and in the understanding of how heavy elements are created in the universe. Spectroscopic information about the orbits of the valence nucleons in these unstable nuclei have led to novel and surprising properties for the corresponding unstable nuclear states [Han95, Mad01]. Due to their short life time, transfer reactions in inverse kinematics with rare nuclei as projectiles are the optimal way to study these nuclei [Cat02] and they are becoming a viable tool to explore single-particle states in neutron- and proton-rich nuclei [For99, Win01, Han01, Cat02, Han03]. However, since rare isotope beam intensities remain very much less than that of stable beams, and the history and experience of the spectroscopy of rare isotopes is much shorter, it is critical to

understand the limitations of transfer reaction theory by selectively re-examining the consistency of more precise measurements made with intense light-ion beams.

It is well documented that large uncertainties have been associated with the extraction of spectroscopic factors. In a systematic compilation of spectroscopic factors for sd-shell nuclei, Endt [End77] noted that very different values of the spectroscopic factors arise from different analyses and/or experiments. By examining a large amount of data, and using consistency checks when available, Endt extracted an error of about 25% for individual spectroscopic factor for the sd-shell. The uncertainty increases to 50% if only (p,d) and (d,p) transfer reactions are used. However, this analysis, performed in 1977 and limited to heavy nuclei with A between 21 to 44, did not provide the systematic uncertainties associated with the method and relied heavily on the analyses of different authors. To assess the systematic uncertainties associated with the extraction of spectroscopic factors using a standardized procedure, we re-analyze the reaction of ^{12}C(d,p)^{13}C(g.s.) and its inverse reaction, ^{13}C(p,d)^{12}C(g.s.), measured over a range of incident energies from 12 MeV to 60 MeV from the published literatures [Liu04].

5.2 ^{12}C(d,p)^{13}C (g.s.) Reaction

There are published angular distributions for the ^{12}C(d,p)^{13}C reaction at incident deuteron energies from 0.4 to 56 MeV. Until now, spectroscopic factors have been extracted from only a subset of these experiments. The associated analyses relied mainly on distorted-waves Born approximation (DWBA) calculations, but with no consistent choice of input parameters. The published ^{12}C(d,p)^{13}C (g.s.) spectroscopic factors are

listed in Table 5.1 and shown by closed points in Figure 5.1 as a function of the incident deuteron energy. For comparison, the published spectroscopic factors for the reaction of $^{13}C(p,d)^{12}C$ (g.s.), to be discussed in Section 5.3, are shown by open points as a function of the equivalent incident deuteron energy. The values fluctuate from 0.3 to 1.4 with no evident correlation with incident energies. In some experiments, multiple values were deduced from different optical model parameter sets or different theories. In these cases the higher values are shown as squares in Figure 5.1. The dashed line shows the theoretical prediction (0.62) of the Cohen and Kurath shell model calculation [Coh67]. Large fluctuations in the data highlight the problem of extracting of a meaningful empirical spectroscopic factor that can be compared to theoretical value.

Our calculations use a modified version of the code TWOFNR [Iga77]. All calculations include the local energy approximation (LEA) for finite range effects [But64] using the zero-range strength (D_0) and range (β) parameter of the Reid Soft core $^3S_1$-$^3D_1$ neutron-proton interaction [Knu75]. For simplicity, no spin-orbit coupling is included as explained in Section 2.3.1.5. Non-locality corrections [Per62] are included in the proton and deuteron channels. All the parameters are listed in Table 2.7.

We first perform calculations where both the exit channel proton and the entrance channel Johnson-Soper (JS) adiabatic potentials using the JLM nucleon-target optical potentials [Pet85]. These are calculated by folding the density-dependent JLM nucleon-nucleon effective interaction [Jeu77], assumed to have a Gaussian form factor of range 1 fm [Mel83], with the assumed target matter density in the mid-point local-density approximation [Mel83]. The matter density distribution for both ^{12}C and ^{13}C are evaluated assuming the modified Harmonic oscillator density parameters (α=1.247 fm,

a=1.649 fm for ^{12}C; α=1.403 fm, a=1.635 fm for ^{13}C) compiled in Ref. [Dej74]. The corresponding root-mean-square (rms) charge radii are 2.46 fm and 2.44 fm for ^{12}C and ^{13}C respectively. The resulting real and imaginary parts of the nucleon potentials are scaled by the factors λ_v=1.0 and λ_w=0.8, respectively, obtained from a systematic study of light nuclei [Pet85].

The spectroscopic factor is extracted by fitting the theory to the data at the first peak in the angular distribution, since the backward angle data are more sensitive to the effects of inelastic couplings and other higher-order effects. To be consistent, the spectroscopic factors are extracted by minimizing χ^2, including only angular points that are (i) within 30% of the maximum yield at the predicted angle and (ii) at θ_{cm}< 30°.

In the present analyses we consider measured angular distributions for the reactions of ^{12}C(d,p)^{13}C (g.s.) over a range of incident energies from 7 MeV to 56 MeV. The calculated angular distributions normalized by the extracted spectroscopic factors are shown as solid lines in Figure 5.2. Each is displaced by a factor of 10 for ease of presentation, the displacement factor being unity for the angular distribution at 19.6 MeV. The associated spectroscopic factors are listed in Table 5.1 and shown at the bottom of Figure 5.3 include re-analysis of the data shown in Figure 5.1 (closed circles) [Mor60, Zai61, Dan63, Sch67, Fet71, Dar73, Ohn86, Lan88] and of additional data sets (closed squares) [Mcg55, Mor60, Rob61, Ham61, Sch64]. Available data at E_d=28 and 56 MeV are not included since their angular distributions do not include the first peak. The rise of the spectroscopic factors with decreasing energy below 12 MeV shown in Figure 5.3 has been observed before [Sch67] and has been attributed to the effect of

resonant structures in the elastic scattering of deuterons [Ohl63] and in the $^{12}C(d,p)^{13}C$ reactions [Eva63]. Excluding measurements affected by compound nucleus formation and resonances, the extracted spectroscopic factors for E_d=12-60 MeV provide an average spectroscopic factor of 0.58±0.09. In contrast, the published values in Figure 5.1 vary from 0.3 to 1.5. Our consistent, theoretically motivated analyses thus reduce the fluctuations substantially.

To find out whether the uncertainty comes from the accuracy in the measurements or from the calculations, we examine the consistency in different measurements at the same incident energy. Figure 5.4, 5.5, and 5.6 show the comparisons of the measurements of $^{12}C(d,p)^{13}C$ reaction for deuteron energies at around 4.5 MeV, 12 MeV, and 15 MeV respectively. In Figure 5.4, the difference among the data is more than 30% in the region from 20° to 50° in the center of mass with no quoted error in the literatures. In Figure 5.5, the quoted error from Ref. [Sch67] and Ref. [Ham61] are 15% and 25% respectively. The difference among the data is close to 20% for the first peak from 10° to 30° in the center of mass. In Figure 5.6, the quoted error from Ref. [Ham61] and Ref. [Mcg55] are both 20%. Ref. [Dar73] did not give error of the data. The difference in the region around 20 deg in the center of mass is more than 20%. From the above analyses, the measured angular distributions do not agree to better than 20%. Thus the variations in the spectroscopic factors we obtained partly come from the uncertainties in the experimental measurements.

To assess the stability of the above adiabatic three-body model calculations, we have repeated the analyses by replacing the JLM nucleon optical potentials everywhere with the Chapel-Hill (CH89) [Var91] global potential set. The calculated angular distributions

normalized by the spectroscopic factors are shown by the dotted curves in Figure 5.2. The spectroscopic factors are shown in the center of Figure 5.3. Overall, the values are quite similar, but consistently higher. The average spectroscopic factors is 0.71±0.10. It should be noted that light nuclei are not included in the extraction of the CH89 potential evaluation. Thus it is remarkable that the CH89 potential seems to work well.

For a final comparison, we also analyzed the full data set within the DWBA formalism, neglecting the role of deuteron break-up channels. To remove energy-dependent optical potential ambiguity, we used the CH89 and Daehnick [Dae80] global potentials for the proton and deuteron channels, respectively. The calculated angular distributions normalized by the spectroscopic factors are shown as dashed curves in Figure 5.2 and the deduced spectroscopic factors are plotted at the top of Figure 5.3. Again, the extracted values are more consistent than the published values; see Figure 5.1. The average value is 0.79±0.19. Comparisons with the JS adiabatic calculations suggest that neglect of the break-up channel within the DWBA is a significant contributing factor at high energies.

Table 5.1: List of references and spectroscopic factors for the $^{12}C(d,p)^{13}C$ (g.s.) reaction

Reaction	E_{beam} (MeV)	SF (Liter.)	SF (JLM)	SF (CH89)	SF (DWBA)	Ref.
$^{12}C(d,p)^{13}C$ (g.s.)	4	0.99	0.62	0.61	0.65	[Gal66]
$^{12}C(d,p)^{13}C$ (g.s.)	4.5	0.72	0.69	0.69	0.6	[Gal66]
$^{12}C(d,p)^{13}C$ (g.s.)	4.5		0.52	0.53	0.4	[Bon56]
$^{12}C(d,p)^{13}C$ (g.s.)	4.5	0.55 0.6 0.8	0.42	0.43	0.49	[Gur69]
$^{12}C(d,p)^{13}C$ (g.s.)	7.15	0.53	0.89	0.93	0.94	[Zai61]
$^{12}C(d,p)^{13}C$ (g.s.)	8.9		0.8	0.9	0.91	[Rob61]
$^{12}C(d,p)^{13}C$ (g.s.)	9.0	0.84	N/A	N/A	N/A	[Smi63]
$^{12}C(d,p)^{13}C$ (g.s.)	10.2		0.68	0.79	0.81	[Ham61]
$^{12}C(d,p)^{13}C$ (g.s.)	11.8		0.61	0.74	0.77	[Sch64]
$^{12}C(d,p)^{13}C$ (g.s.)	12	1.15	0.50	0.63	0.68	[Lan88]
$^{12}C(d,p)^{13}C$ (g.s.)	12	1.16 0.64 0.83 0.85	0.75	0.85	0.86	[Sch67] [Dob70] [Gri75]
$^{12}C(d,p)^{13}C$ (g.s.)	12.4		0.63	0.74	0.78	[Ham61]
$^{12}C(d,p)^{13}C$ (g.s.)	14.7		0.61	0.74	0.79	[Ham61]
$^{12}C(d,p)^{13}C$ (g.s.)	14.8		0.64	0.75	0.78	[Mcg55]
$^{12}C(d,p)^{13}C$ (g.s.)	15	1.1 1.4	0.53	0.67	0.74	[Dar73]
$^{12}C(d,p)^{13}C$ (g.s.)	16.6	0.85	0.48	0.59	0.66	[Mor60]
$^{12}C(d,p)^{13}C$ (g.s.)	19.6		0.52	0.65	0.76	[Mor60]
$^{12}C(d,p)^{13}C$ (g.s.)	25.9	0.7	0.59	0.69	0.79	[Dan63]
$^{12}C(d,p)^{13}C$ (g.s.)	28		0.82	1.06	1.49	[Slo62]
$^{12}C(d,p)^{13}C$ (g.s.)	30	0.77	0.52	0.65	0.79	[Ohn86]
$^{12}C(d,p)^{13}C$ (g.s.)	51	0.95	0.66	0.82	1.06	[Fet71] [Gol72]
$^{12}C(d,p)^{13}C$ (g.s.)	56	0.63 0.75 1.26	1.05	1.26	1.44	[Hat84]
(average)			0.58 ±0.09	0.71 ±0.10	0.79 ±0.19	

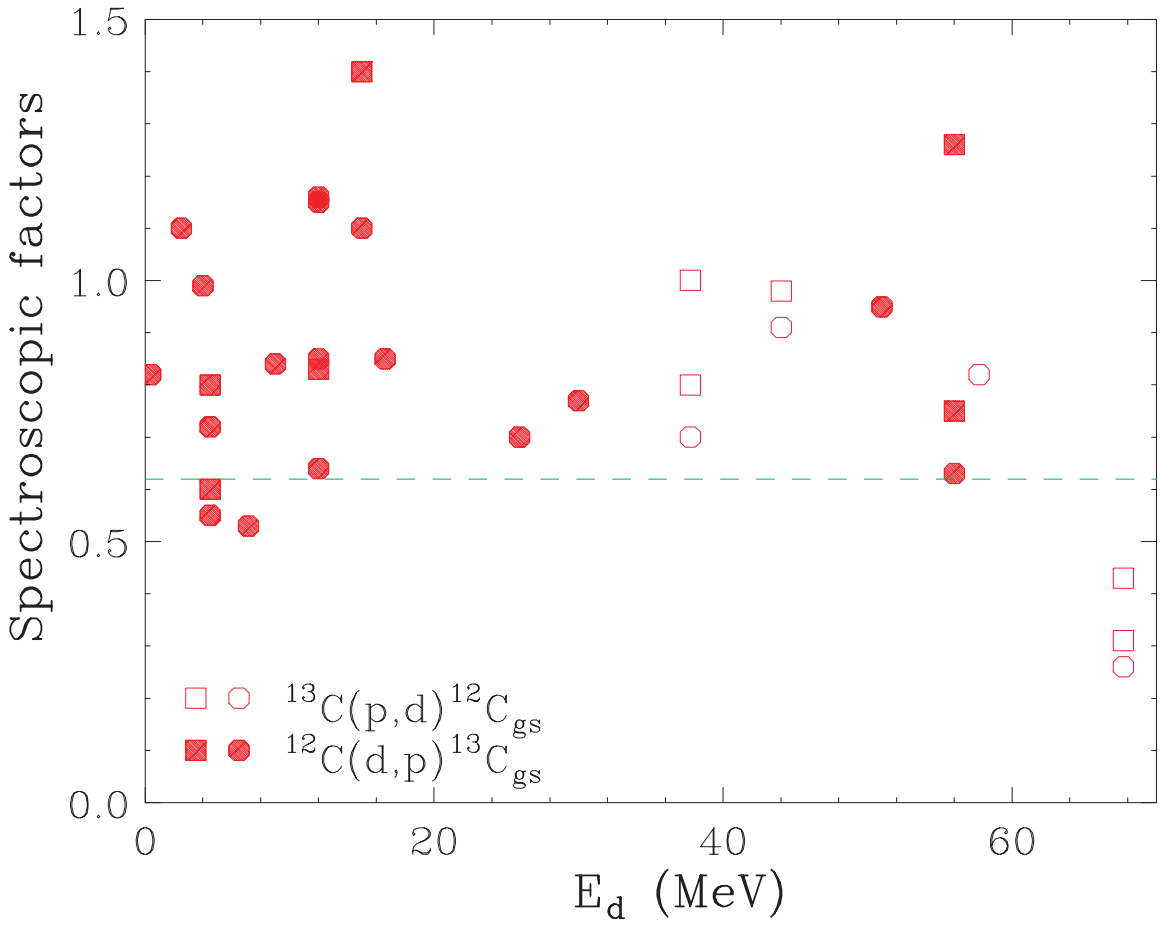

Figure 5.1: Spectroscopic factors for $^{12}C(d,p)^{13}C$ (g.s.) and $^{13}C(p,d)^{12}C$ (g.s.) reactions extracted from the literatures (see Table 5.1 and Table 5.2) .

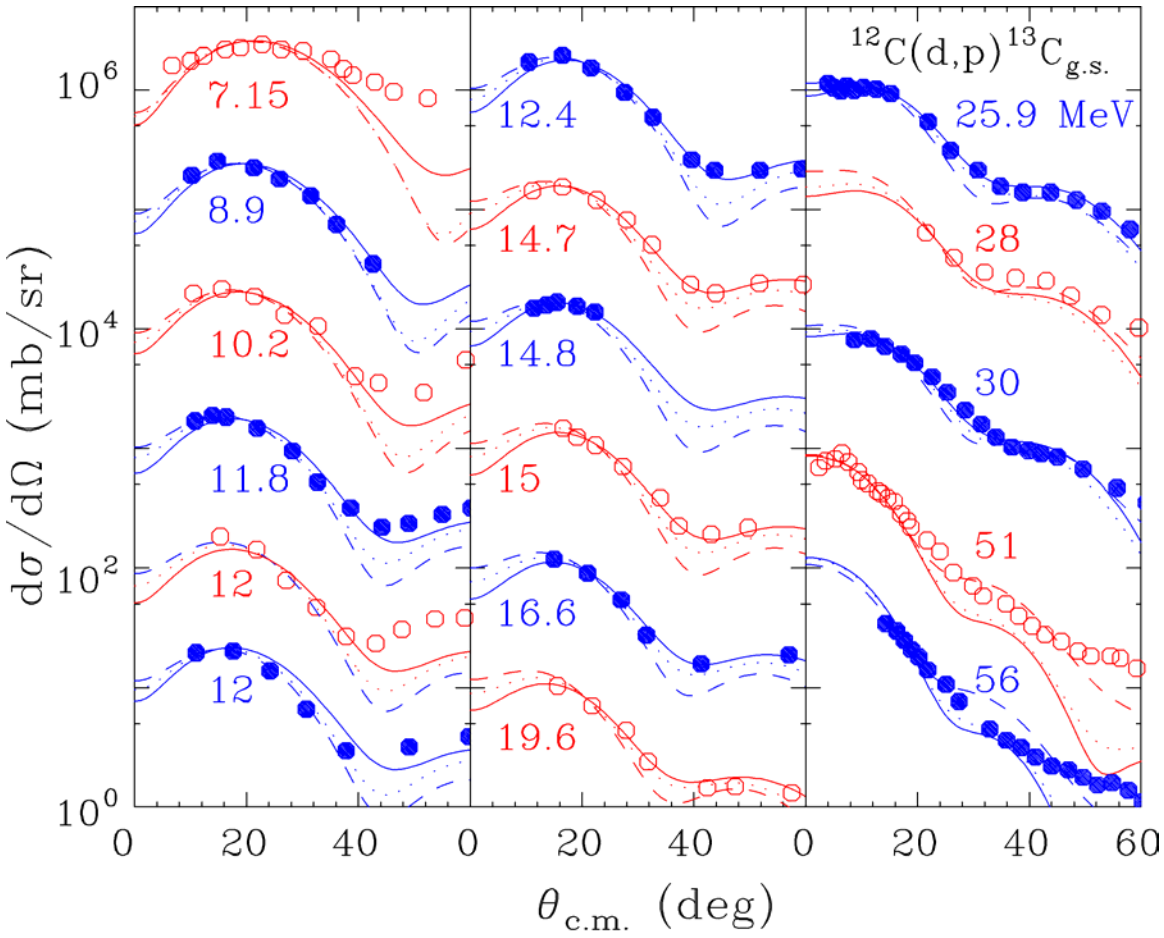

Figure 5.2: Angular distributions for $^{12}C(d,p)^{13}C$ (g.s.) reactions for beam energies from 7 to 56 MeV: solid lines present ADBA (JLM); dotted lines present ADBA (CH89); dashed lines present DWBA. Each distribution is displaced by factor of 10 from adjacent distributions. The overall normalization factor is 1 for the 19.6 MeV data. References are listed in Table 5.1.

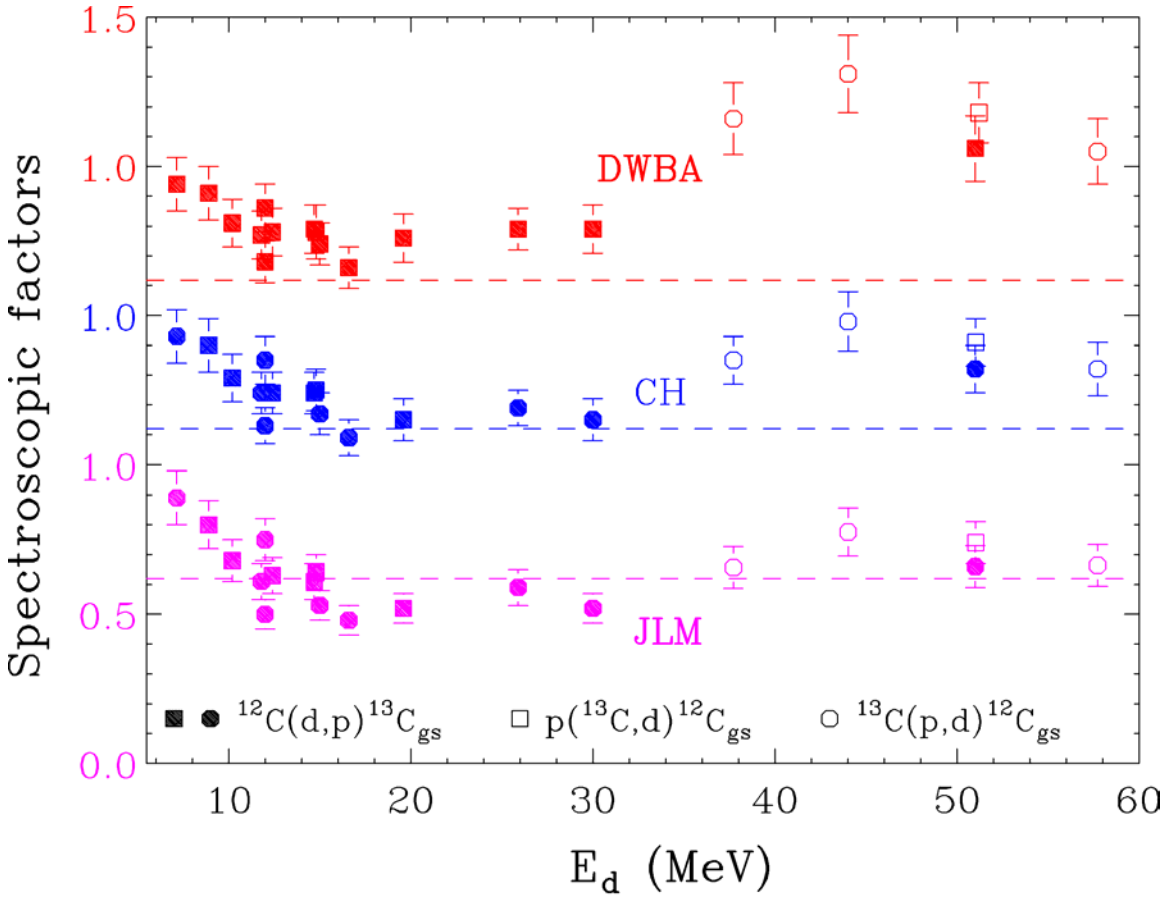

Figure 5.3: Extracted spectroscopic factors in the present work for ^{12}C(d,p)^{13}C (g.s.), ^{13}C(p,d)^{12}C (g.s.), and p(^{13}C,d)^{12}C (g.s.) reactions. The dashed lines represent the shell model prediction of Cohen and Kurath [Coh67] of 0.62. See text for detail explanation.

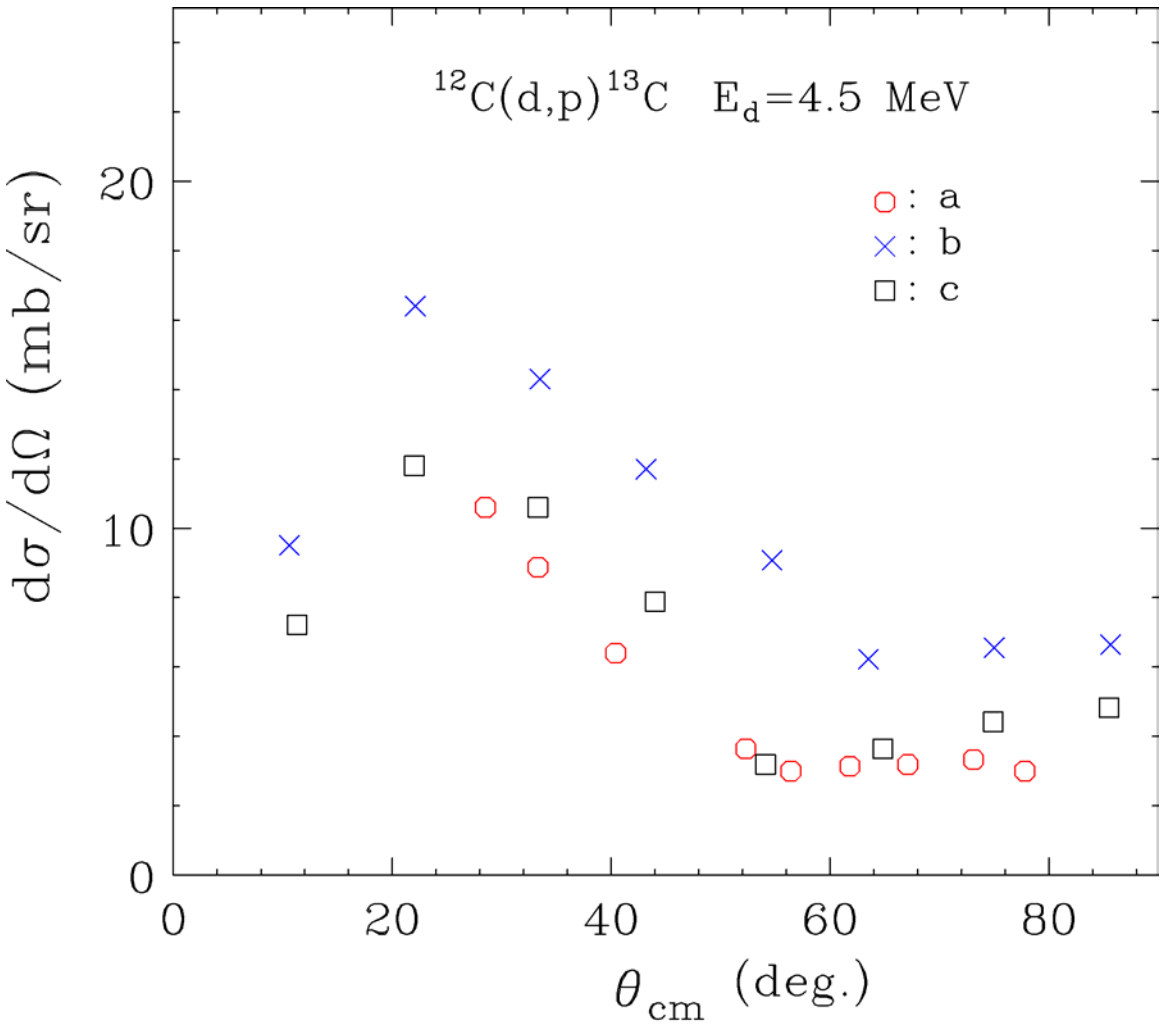

Figure 5.4: Comparison of the existing measurements of ^{12}C(d,p)^{13}C (g.s.) reaction for deuteron energy at 4.5 MeV, a [Gur69], b [Gal66], and c [Bon56].

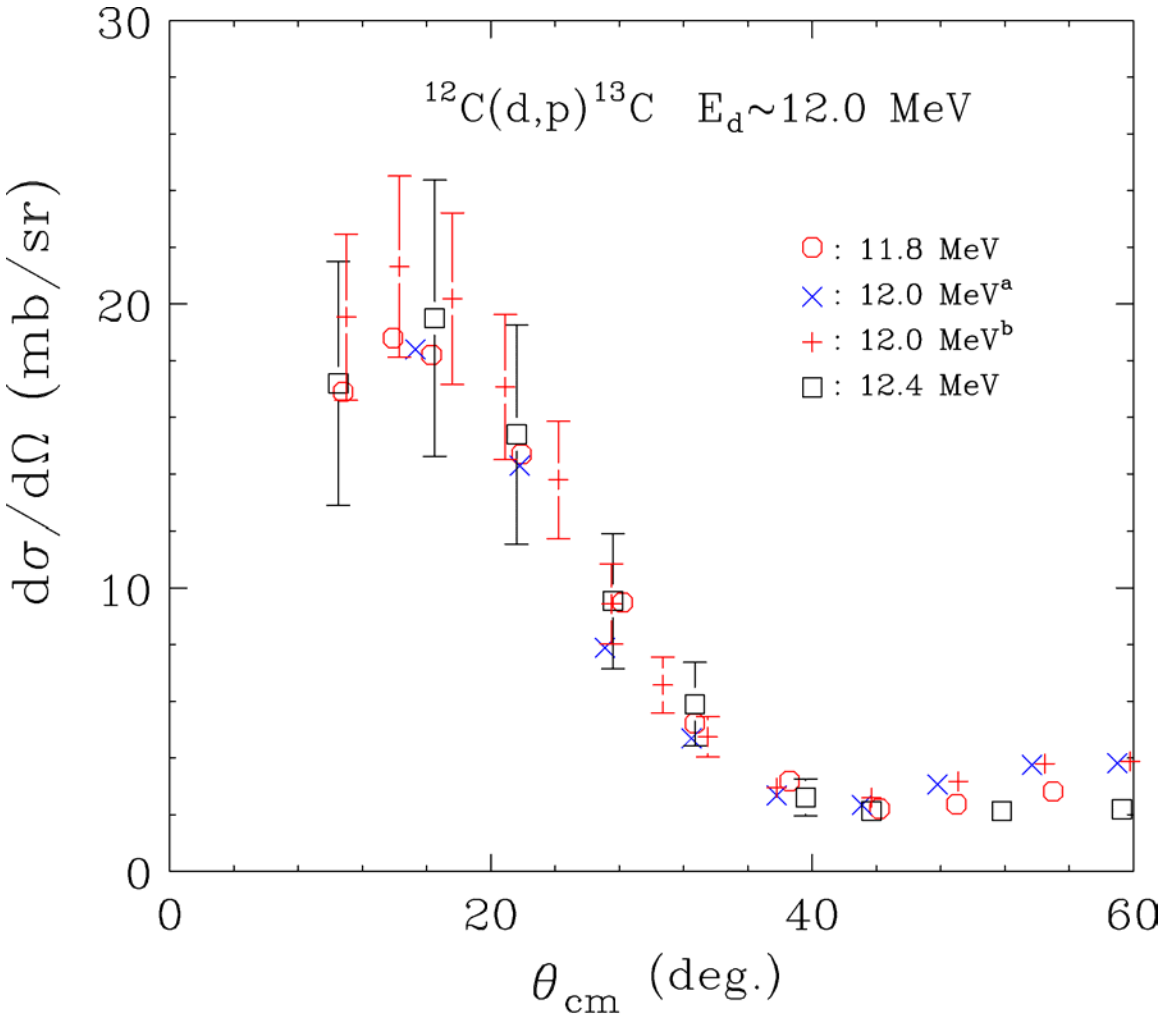

Figure 5.5: Comparison of the existing measurements of ^{12}C(d,p)^{13}C (g.s.) reaction for deuteron energies at 11.8 MeV [Sch64], 12.0 MeV a [Lan88], 12.0 MeV b [Sch67], and 12.4 MeV [Ham61].

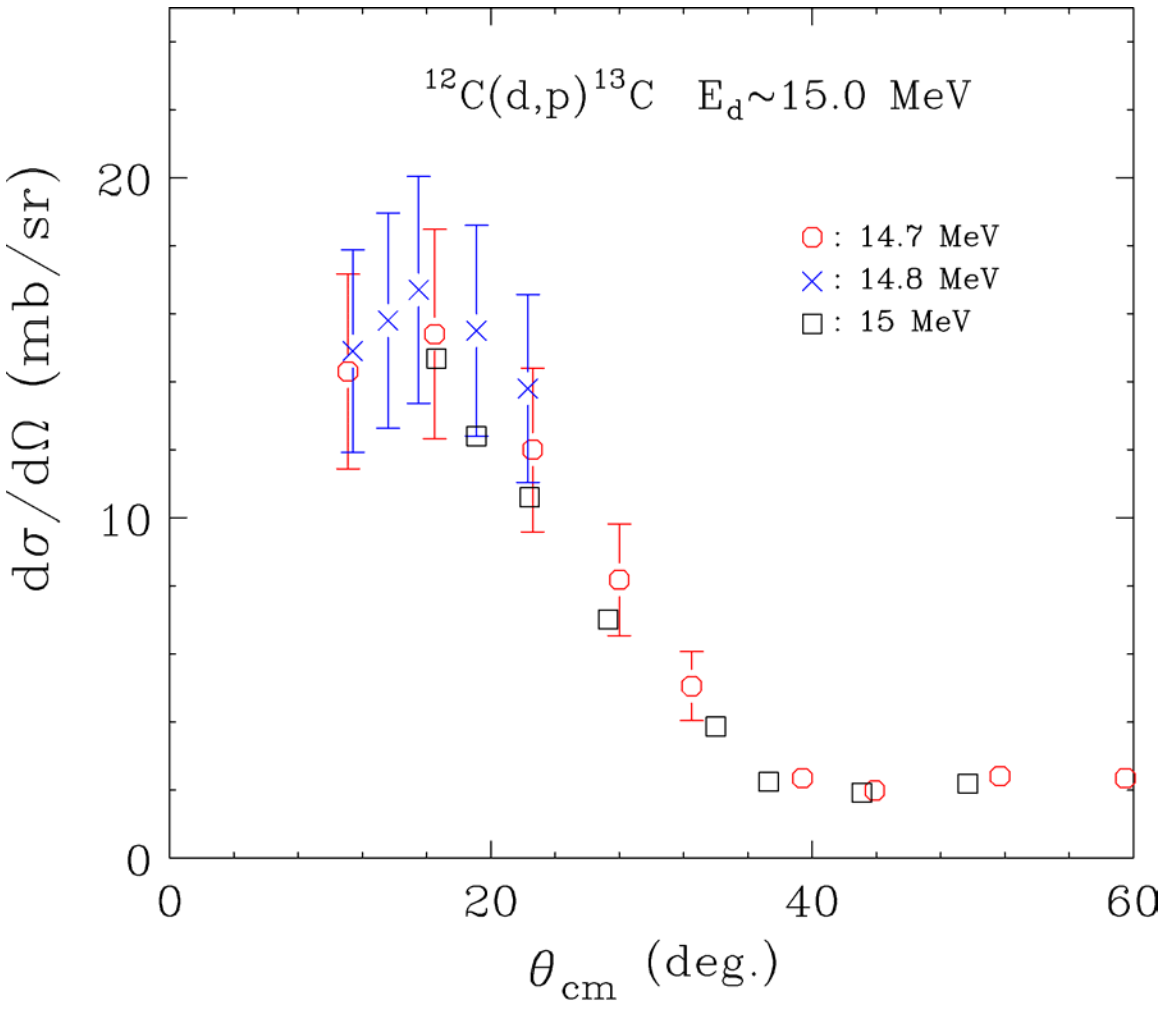

Figure 5.6: Comparison of the existing measurements of ^{12}C(d,p)^{13}C (g.s.) reaction for deuteron energies at 14.7 MeV [Ham61], 14.8 MeV [Mcg55], and 15 MeV [Dar73].

5.3 $^{13}C(p,d)^{12}C$ (g.s.) and $p(^{13}C,d)^{12}C$ (g.s.) Reactions

Systematic analyses are performed to the measurements of $^{13}C(p,d)^{12}C$ reaction to the ground state [Toy95, Cam87, Tak68, Hos80] listed in Table 5.2. The proton energies range from 35 MeV to 65 MeV. Same parameters listed in Table 2.7 and same procedure as described in section 5.2 are employed.

The data and calculations multiplied by the corresponding spectroscopic factors listed in Table 5.2 are shown in Figure 5.7. The angular distributions at 35 MeV, 41.3 MeV, and 65.0 MeV do not have data at forward angles. These data without the first peak may not give reliable SF. The data at 55.0 MeV have data at forward angles but the shape is different from that of the calculations. The extracted SF at 65.0 MeV is almost twice the expected value. Thus the data at 65.0 MeV may not be correct. The extracted SF from the data at 35.0 MeV, 41.3 MeV, and 55.0 MeV are plotted in Figure 5.3 as open circle points. As the existing measurements do not give reliable SF, a new measurement to cover the first peak in inverse kinematics is desirable.

The data and calculations for the inverse kinematic reaction of $p(^{13}C,d)^{12}C$ (g.s.) performed in the present work are plotted as the third set of data (open points) and lines in Figure 5.7 The extracted spectroscopic factors, as shown in open squares in Figure 5.3, are 0.74, 0.91, and 1.18 for ADBA (JLM), ADBA (CH89), and DWBA calculations, respectively. One possible reason that the (p,d) reactions give higher spectroscopic factors than the (d,p) reactions in Section 5.2 is that the (p,d) reactions are performed at higher energies. The overall averaged spectroscopic factors from all the (d,p) and (p,d) reactions are 0.62±0.09, 0.76±0.11, and 0.89±0.20 for ADBA (JLM), ADBA (CH), and

DWBA calculations, respectively. The ADBA calculations based on JLM potentials give the best result compared to theory. Again, the SF values from the DWBA calculations are higher. As the importance of the deuteron break-up effects has been demonstrated, we will not discuss the DWBA calculations in the remaining part of this chapter.

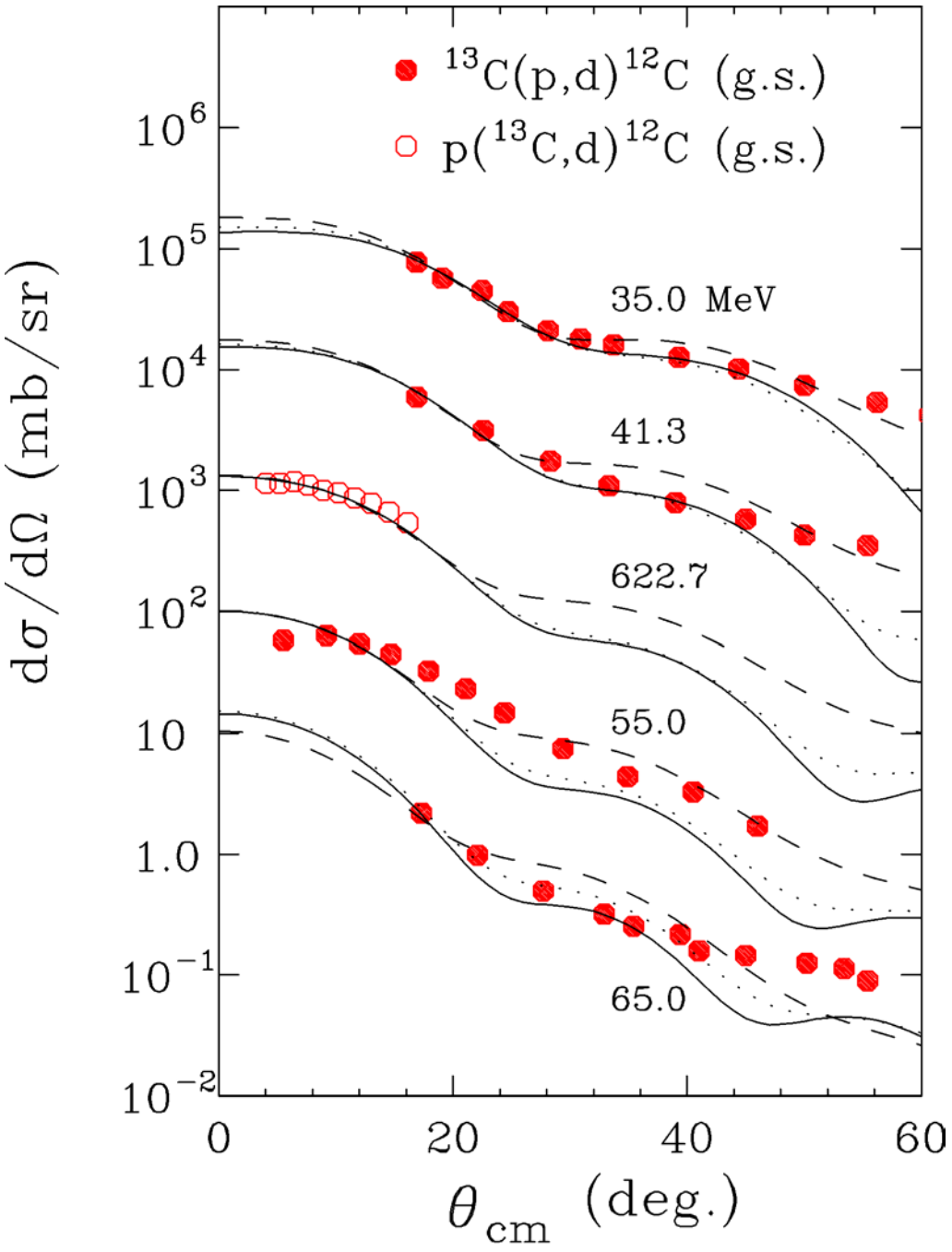

Figure 5.7: Angular distributions for ^{13}C(p,d)^{12}C (g.s.) and p(^{13}C,d)^{12}C (g.s.) reactions for beam energies from 35 to 65 MeV: solid lines present ADBA (JLM); dotted lines present ADBA (CH89); dashed lines present DWBA. The calculations have been normalized by the spectroscopic factors. Each distribution is displaced by factor of 10 from adjacent distributions. The overall normalization factor is 1 for the 65.0 MeV data.

Table 5.2: List of references and spectroscopic factors for the $^{13}C(p,d)^{12}C$ (g.s.) and $p(^{13}C,d)^{12}C$ (g.s.) reactions

Reaction	E_p (MeV)	SF (Liter.)	SF (JLM)	SF (CH89)	SF (DWBA)	Ref.
$^{13}C(p,d)^{12}C$ (g.s.)	35	0.7 0.8 1.0	0.66	0.85	1.16	[Toy95]
$^{13}C(p,d)^{12}C$ (g.s.)	41.3	0.91 0.98	0.78	0.98	1.31	[Cam87]
$^{13}C(p,d)^{12}C$ (g.s.)	55	0.82	0.66	0.82	1.05	[Tak68]
$^{13}C(p,d)^{12}C$ (g.s.)	65	0.26 0.31 0.43	1.22	1.57	1.33	[Hos80]
(average)			0.70 ±0.07	0.88 ±0.09	1.17 ±0.13	
$p(^{13}C,d)^{12}C$ (g.s.)	48.3*		0.74	0.91	1.18	

* Equivalent proton energy

5.4 $^{13}C(p,d)^{12}C$ (2^+) and $p(^{13}C,d)^{12}C$ (2^+) Reactions

Theoretically the transferred neutron in the reaction of $^{13}C(p,d)^{12}C$ to the first excited state 2^+ at 4.439MeV of ^{12}C is predicted to be in pure $1p_{3/2}$ orbit [Cam87]. The theoretical spectroscopic factor from Cohen and Kurath [Coh67] is 1.12. This clearly identified state provides another opportunity to test our strategy to extract the SF.

Systematic analyses are performed to the existing measurements of $^{13}C(p,d)^{12}C$ reaction to the first excited state [Toy95, Cam87, Tak68]. The proton energies range from 35 MeV to 65 MeV. The same procedure as described in section 5.2 is employed.

The data and calculations for the present measurement of $p(^{13}C,d)^{12}C^*$ (4.439MeV) are plotted as the third set (open points) in Figure 5.8 together with the data (closed points) from the literatures [Toy95, Cam87, Tak68]. Among the published data, only the data at 55.0MeV have reasonable coverage at forward angles. The data at 35.0 MeV and 41.3 MeV are not reliable since they did not include the first peak. However, the extracted spectroscopic factors by fitting the slope of these two data sets may provide consistent checks. The extracted spectroscopic factors are listed in Table 5.3 and plotted in Figure 5.9. The averaged spectroscopic factors from ADBA calculations based on JLM potentials and CH89 potentials are 0.92±0.09 and 1.08±0.13, respectively. The extracted SF for present measurement are 1.03 and 1.2 from ADBA(JLM) and ADBA(CH89), respectively. These values are listed in Table 5.3. The SF values from CH89 potentials are usually higher than that from JLM potentials.

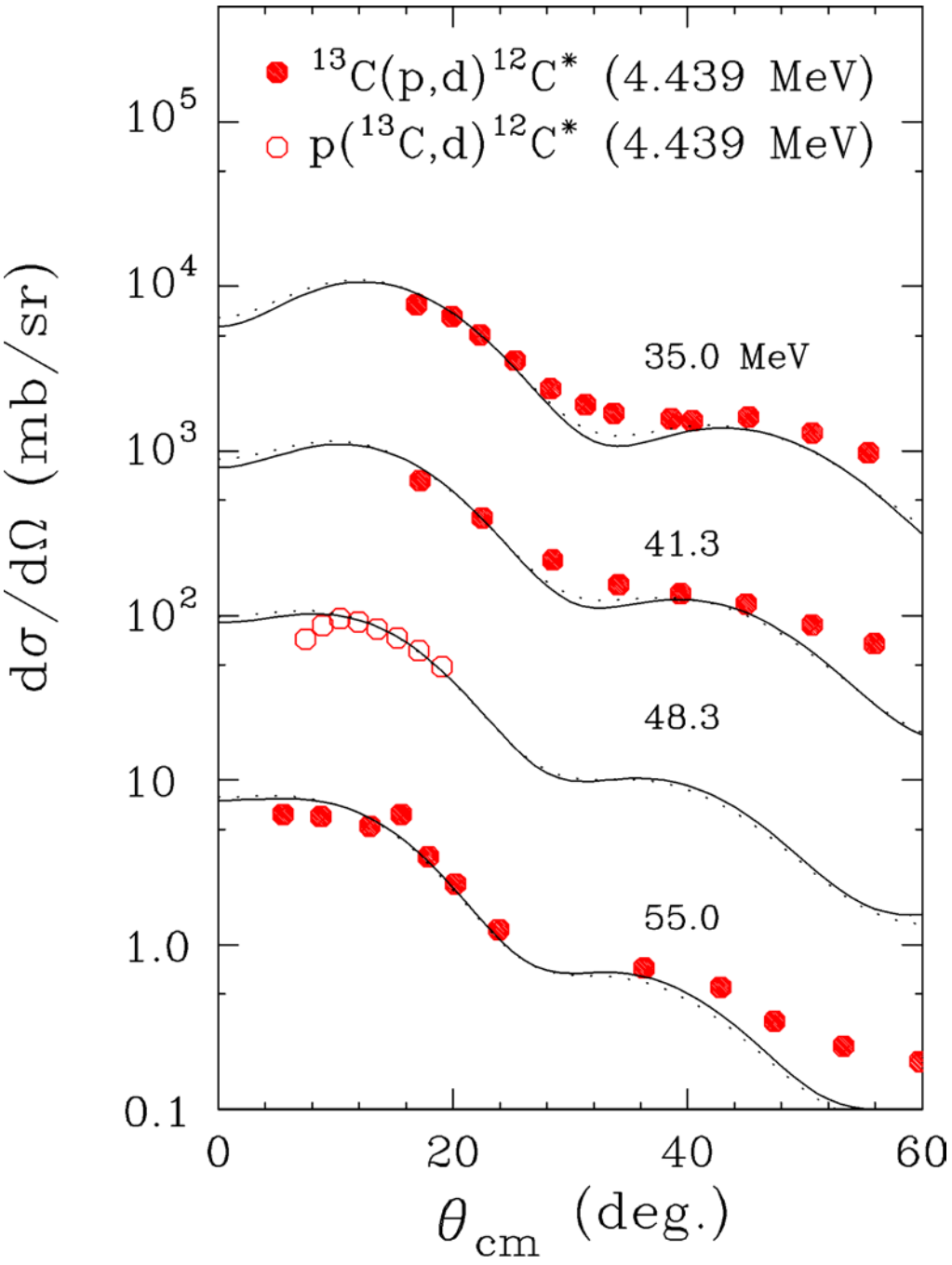

Figure 5.8: **C**alculations for reactions of ^{13}C(p,d)^{12}C* (4.439MeV) and p(^{13}C,d)^{12}C* (4.439MeV) [Toy95, Cam87, Tak68]; solid lines present ADBA (JLM); dotted lines present ADBA (CH89). The calculations have been normalized by the spectroscopic factors. Each distribution is displaced by factor of 10 from adjacent distributions. The overall normalization factor is 1 for the 55.0 MeV data.

Table 5.3: Extracted spectroscopic factors of the $1p_{3/2}$ neutron from the $^{13}C(p,d)^{12}C\ (2^+)$ and $p(^{13}C,d)^{12}C\ (2^+)$ reactions.

Reaction	Proton energy (MeV)	SF ADBA (JLM)	SF ADBA (CH89)	Ref.
$^{13}C(p,d)^{12}C^*\ (2^+)$	35	0.92	1.08	[Toy95]
$^{13}C(p,d)^{12}C^*\ (2^+)$	41.3	1.01	1.2	[Cam87]
$^{13}C(p,d)^{12}C^*\ (2^+)$	55	0.84	0.95	[Tak68]
(average)		(0.92±0.09)	(1.08±0.13)	
$p(^{13}C,d)^{12}C^*\ (2^+)$	48.3*	1.03	1.2	

* Equivalent proton energy

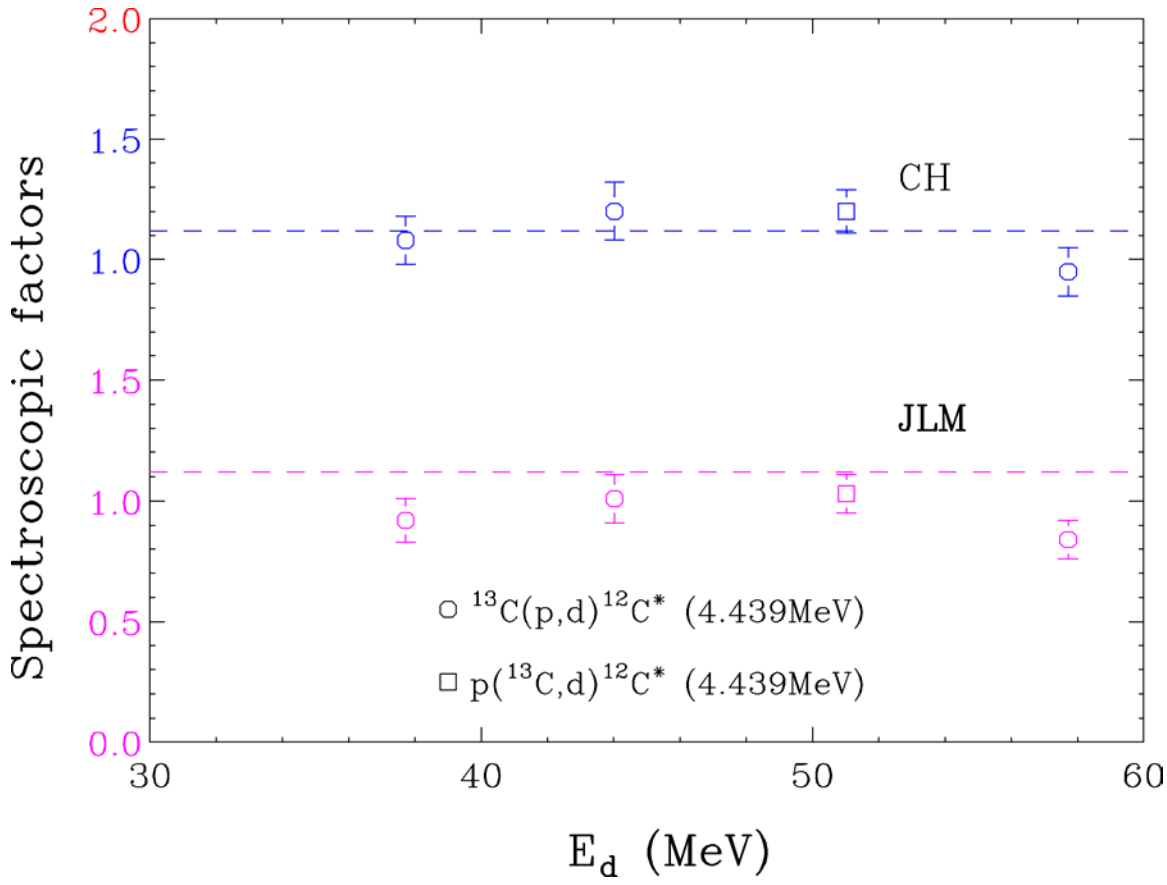

Figure 5.9: Extracted spectroscopic factors of the reactions $^{13}C(p,d)^{12}C^*$ (4.439MeV) (circle) and $p(^{13}C,d)^{12}C^*$ (4.439MeV) (square). The dashed lines represent the shell model prediction of 1.12 by Cohen and Kurath [Coh67].

5.4 $^{10}B(d,p)^{11}B$ (g.s.), $^{11}B(p,d)^{10}B$ (g.s.), and $p(^{11}B,d)^{10}B$ (g.s.) Reactions

Systematic analyses are performed for the reaction of $^{11}B(p,d)^{10}B$ (g.s.) [Leg63] [Kul68] [Slo62] and its inverse reaction of $^{10}B(d,p)^{11}B$ (g.s.) [Hin62] [Sch67] [Bar65]. The transferred neutron is in $1p_{3/2}$ orbit and its form factor is plotted in Figure 2.23. The theoretical spectroscopic factor from the shell model is 1.09 [Coh67]. Applying the consistent procedure as described above, the ADBA calculations are performed based on CH89 and JLM potentials respectively. The modified harmonic oscillator densities (α=0.837 fm, a=1.71 fm for ^{10}B; α=0.811 fm, a=1.69 fm for ^{11}B) compiled in Ref. [Dej74] are used in the JLM potentials.

The data and calculations are shown in Figure 5.10 for the (d,p) reactions and in Figure 5.11 for the (p,d) reactions, respectively. The ADBA calculations based on CH89 and JLM potentials give similar results. The spectroscopic factors have been extracted by fitting the first peaks as described in section 5.2. The results are listed in Table 5.4 and plotted in Figure 5.12. The spectroscopic factors from the published data present a trend with larger value at 30 MeV and lower value at lower (10 MeV) and higher (50 MeV) energies. Particularly, the measurement of $^{11}B(p,d)^{10}B$ at incident energy of 19 MeV (not plotted) gave a much higher SF compared to other experiments. In general, the absolute cross sections increase with incident energy. However, instead of lower cross section, the measured cross sections at 19 MeV are nearly twice as large as the cross sections measured at 33.6 MeV and 44.1 MeV. Thus, we believe this data set has normalization

problems and disregard it. The average value of the extracted SF except the data at 19 MeV is 1.37±0.34 and 1.34±0.31 by using potentials of JLM and CH89 respectively.

The theoretical angular distribution calculations for the $p(^{11}B,d)^{10}B$ reaction are shown in Figure 5.11 as open symbols. The spectroscopic factors calculated from ADBA based on JLM and CH89 potentials are 1.05 and 0.97 respectively. Due to low statistics, the data of this measurement have larger error bar. The statistical uncertainty of the extracted SF is 17.2% for both the JLM potential and CH89 potential. However we cannot determine systematic errors due to our concern about the absolute normalization of those cross sections. Some data from the S800 scintillator are missed. Although the data for present measurements seem reasonable, we are not sure the normalization is absolutely correct.

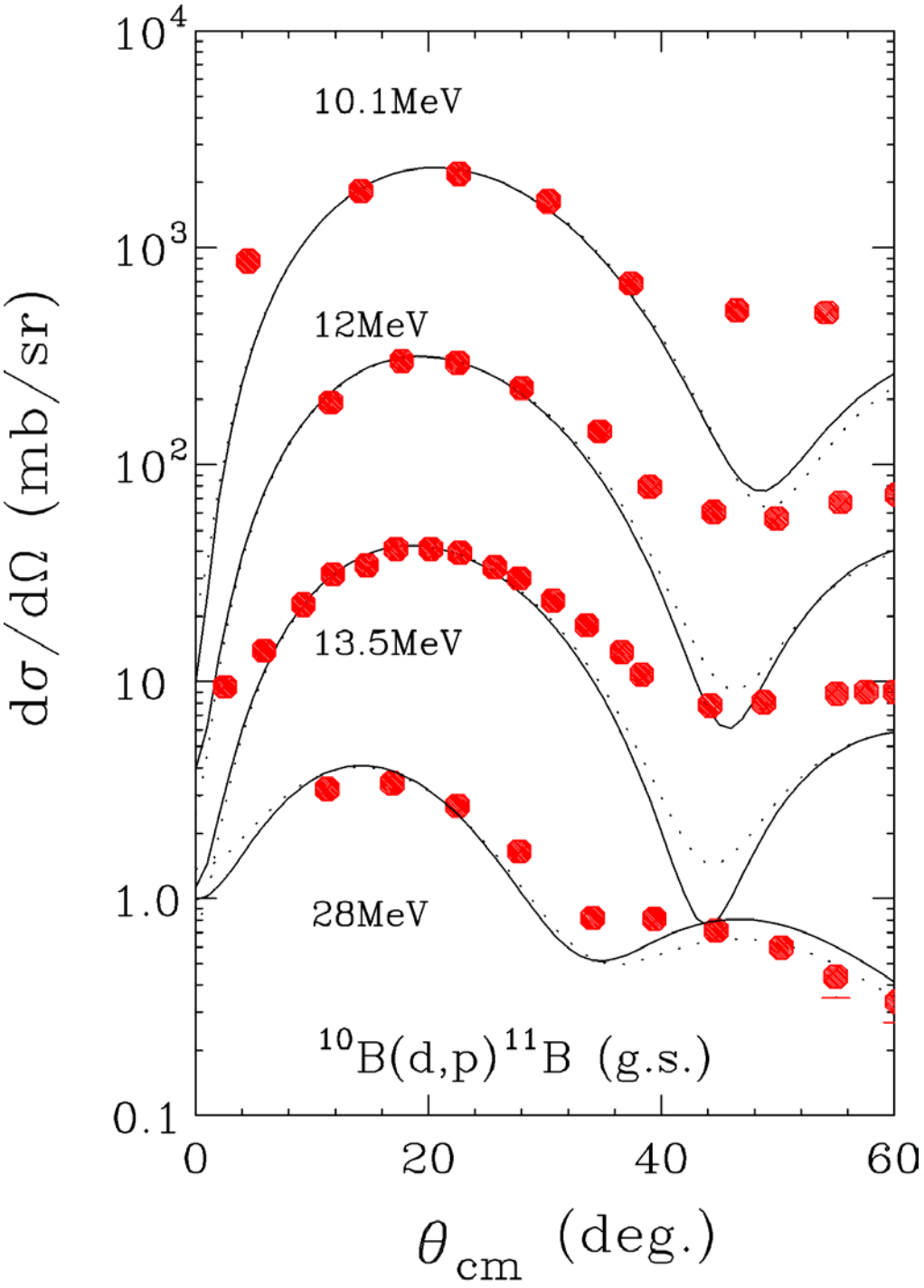

Figure 5.10: Calculations of ^{10}B(d,p)^{11}B (g.s.) reaction at 10.1 MeV [Hin62], 12.0 MeV [Sch67], 13.5 MeV [Bar65], and 28 MeV [Slo62]: solid lines present ADBA (JLM); dotted lines present ADBA (CH89). The calculations have been normalized by the spectroscopic factors. Each distribution is displaced by factor of 10 from adjacent distributions. The overall normalization factor is 1 for the 28.0 MeV data.

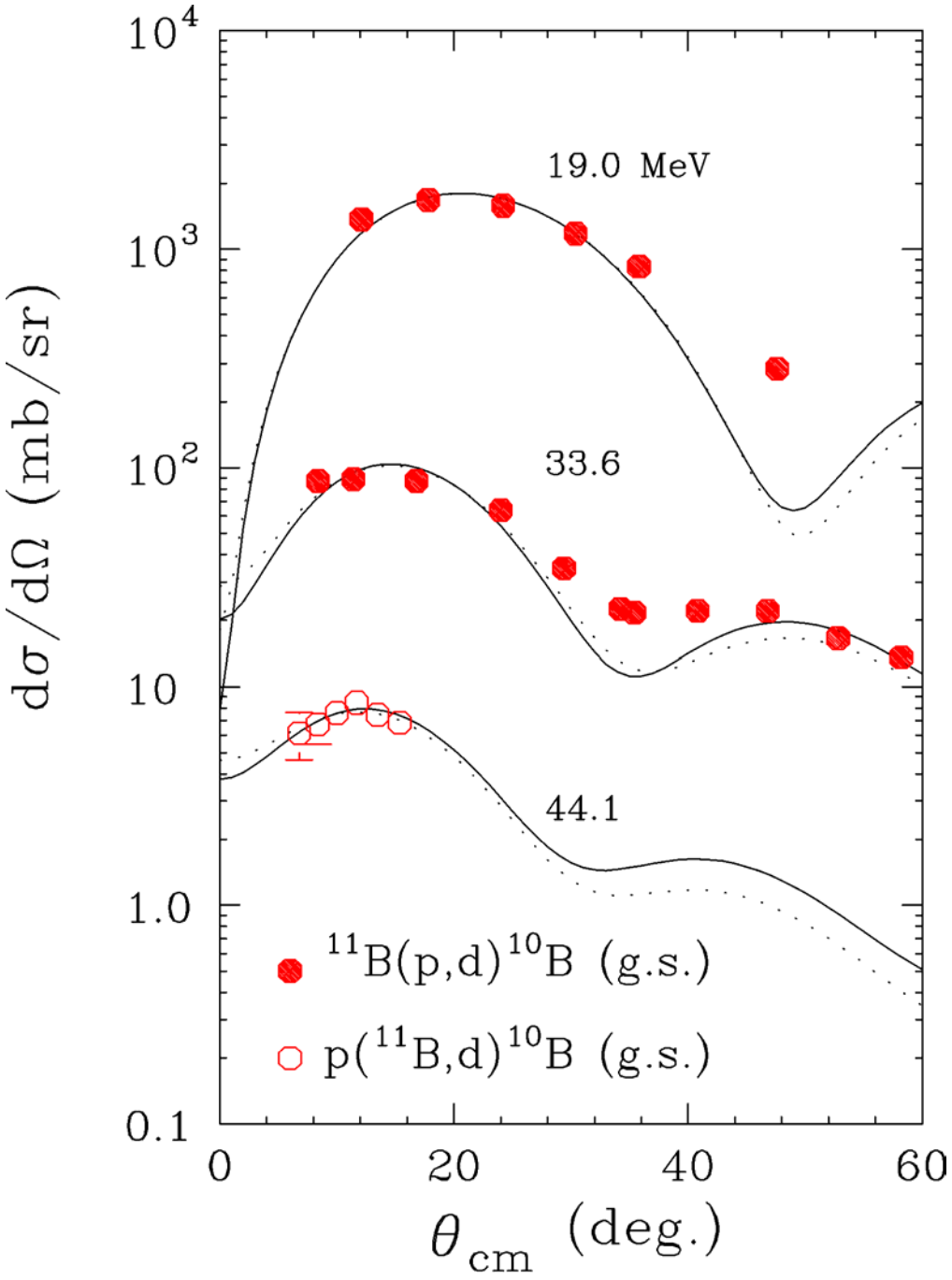

Figure 5.11: Calculations of ^{11}B(p,d)^{10}B (g.s.) (closed points) p(^{11}B,d)^{10}B (g.s.) (open points): solid lines present ADBA (JLM); dotted lines present ADBA (CH89). The calculations have been normalized by the spectroscopic factors. Each distribution is displaced by factor of 10 from adjacent distributions. The overall normalization factor is 1 for the present data.

Table 5.4: Extracted spectroscopic factors of the $1p_{3/2}$ neutron from the reactions of $^{11}B(p,d)^{10}B$ (g.s.), $^{10}B(d,p)^{11}B$ (g.s.), and $p(^{11}B,d)^{10}B$ (g.s.)

Reaction	Beam energy (MeV)	SF ADBA (JLM)	SF ADBA (CH89)	Ref.
$^{11}B(p,d)^{10}B$ (g.s.)	19	3.25	3.22	[Leg63]
^{11}B (p,d) ^{10}B (g.s.)	33.6	1.35	1.24	[Kul68]
$^{10}B(d,p)^{11}B$ (g.s.)	10.1	0.94	0.94	[Hin62]
$^{10}B(d,p)^{11}B$ (g.s.)	12	1.20	1.22	[Sch67]
$^{10}B(d,p)^{11}B$ (g.s.)	13.5	1.56	1.61	[Bar65]
$^{10}B(d,p)^{11}B$ (g.s.)	28	1.82	1.68	[Slo62]
(average)		(1.37±0.34)	(1.34±0.31)	
$p(^{11}B,d)^{10}B$ (g.s.)	44.1*	1.05	0.97	

* Equivalent proton energy

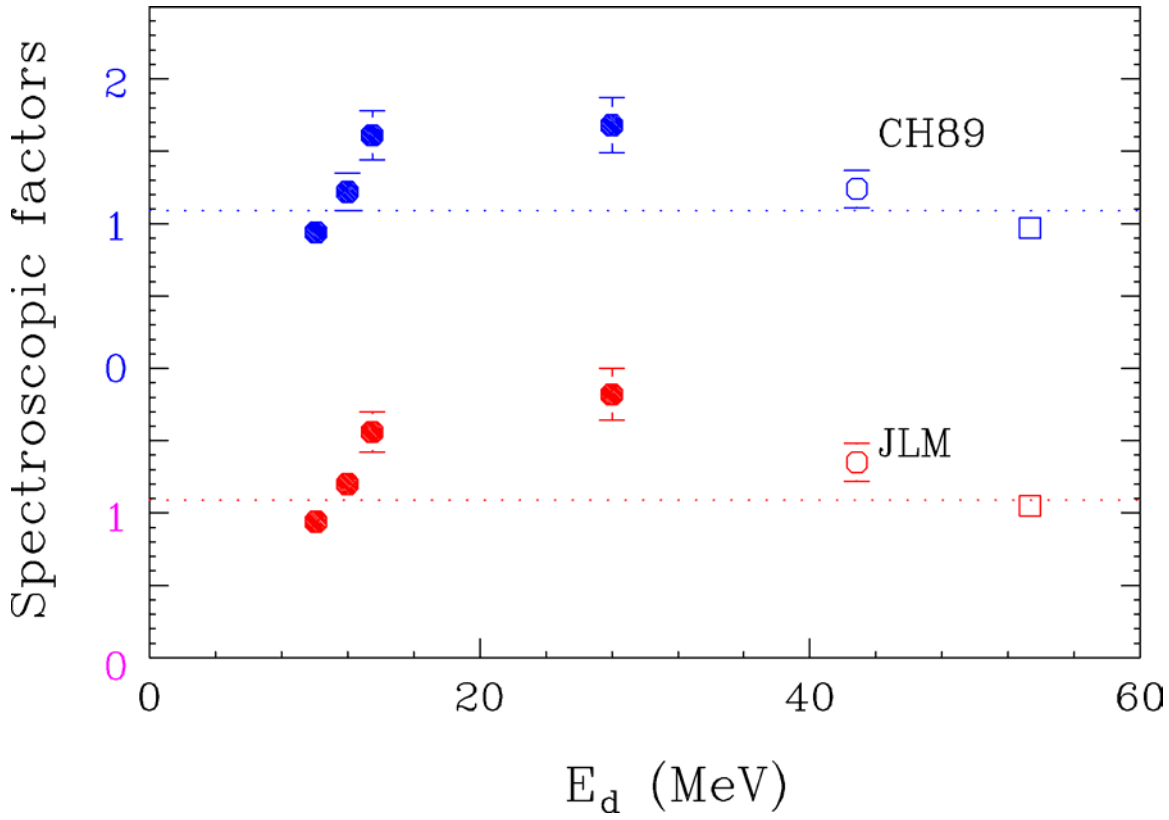

Figure 5.12: Extracted spectroscopic factors for the reaction of p(^{11}B,d)^{10}B (g.s.) (open square), ^{11}B(p,d)^{10}B (g.s.) (open circle), and ^{10}B(d,p)^{11}B (g.s.) (closed circle). The dashed lines represent the shell model prediction of 1.09 by Cohen and Kurath [Coh67].

5.6 ^{9}Be(d,p)^{10}Be (g.s.) and p(^{10}Be,d)^{9}Be (g.s.) Reactions

Systematic analyses are performed on the angular distributions measured from the ^{9}Be(d,p)^{10}Be reactions that were published in the literatures [Zel01, Gen00, Vas87, Sch64, Dar76, And74, Slo62]. The transferred neutron is in the $1p_{3/2}$ orbit and its form factor is shown in Figure 2.23. The SF value obtained from the theoretical prediction of shell model is 2.35 [Coh67]. The ADBA calculations are based on CH potentials as described in section 5.2. The JLM potential is not used since the nucleon radius information of ^{10}Be is not available. The experimental data and calculations are shown in Figure 5.13. The extracted spectroscopic factors are listed in Table 5.5 and plotted in Figure 5.14. The systematic studies do not give a consistent value of spectroscopic factor. The data from 6.0 MeV to 11.0 MeV came from one reference of [Gen00], which gave the spectroscopic factor value around 1.0 for deuteron energies from 7.0 MeV to 11.0 MeV. The other data yield spectroscopic factor values from 0.97 to 2.59. There is big difference in the measured cross sections at 15 MeV and at 15.3 MeV, which give spectroscopic factor of 1.83 and 1.19 respectively at nearly the same energies. The average value (to give the same weight for different systems, only one set from Ref. [Gen00] at 11.0 MeV is included) is 1.40±0.41 with rather large uncertainty.

The data and the calculations for the present measurement in the inverse kinematics of p(^{10}Be,d)^{9}Be are shown as open points in Figure 5.13. Our ADBA (CH89) calculation gives spectroscopic factor of 2.99, which is 27% higher than the theoretical value and nearly a factor of two higher than the values obtained from seven (d,p) reactions measured by different groups. Since we have problems in the absolute normalization as

discussed in Section 4.3, it is not clear if the discrepancies arise from problems in our measurements.

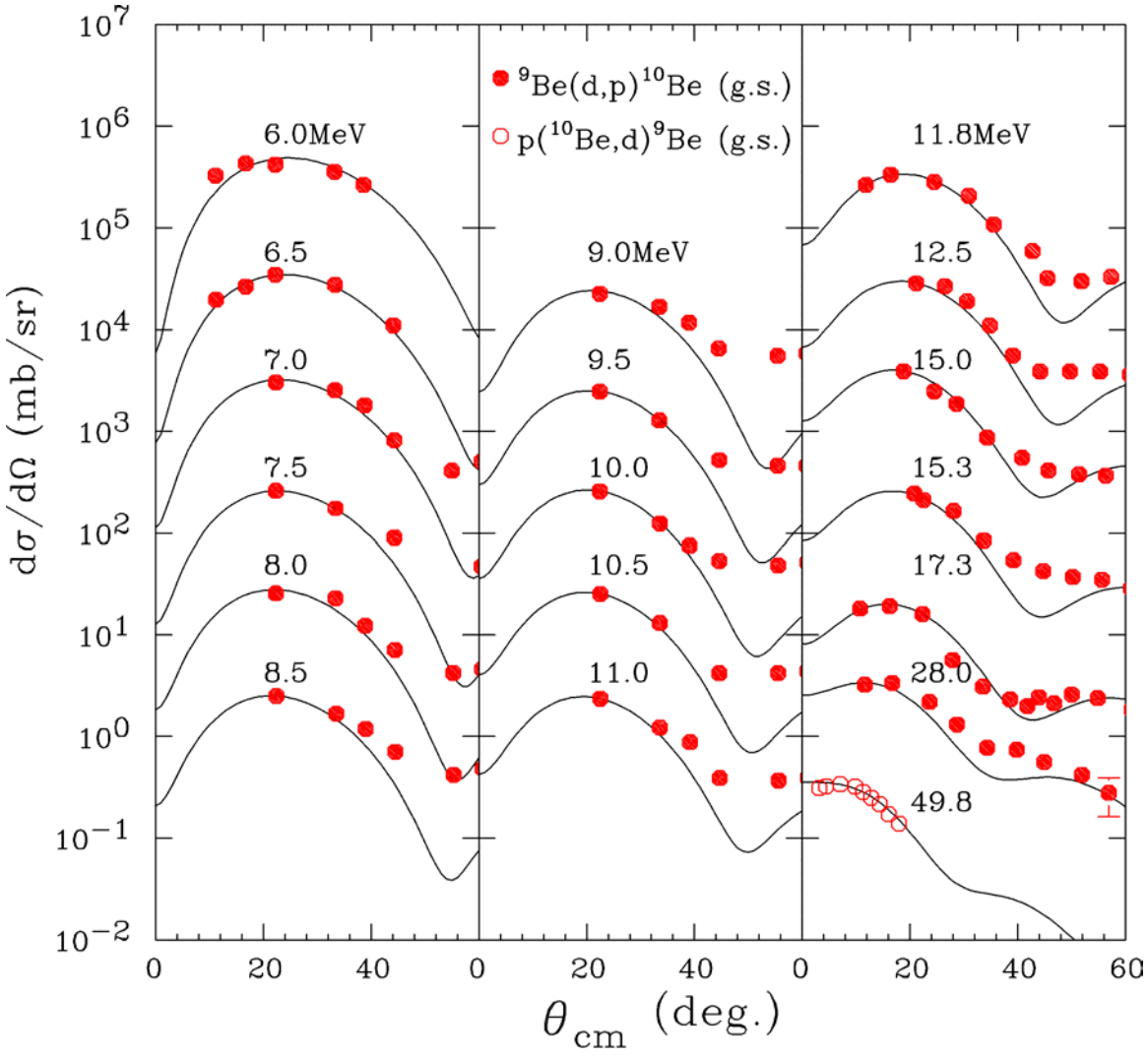

Figure 5.13: ADBA calculations based on CH89 potentials for the reactions of ^{9}Be(d,p)^{10}Be (g.s.) (closed circle) [Zel01, Gen00, Vas87, Sch64, Dar76, And74, Slo62] and p(^{10}Be,d)^{9}Be (g.s.) (open circle). The calculations have been normalized by the spectroscopic factors. Each distribution in closed circle is displaced by factor of 10 from adjacent distributions. The overall normalization factor is 1 for the data at 11.0 MeV. The present data is reduced by a factor of 100.

Table 5.5: Extracted spectroscopic factors of the $1p_{3/2}$ neutron from the reactions of p(^{10}Be,d)^{9}Be (g.s.), and ^{9}Be(d,p)^{10}Be (g.s.)

Reaction	Incident Energy (MeV)	SF ADBA (CH89)	Ref.
^{9}Be(d,p)^{10}Be (g.s.)	6	2.05	[Gen00]
^{9}Be(d,p)^{10}Be (g.s.)	6.5	1.43	[Gen00]
^{9}Be(d,p)^{10}Be (g.s.)	7	1.3	[Gen00]
^{9}Be(d,p)^{10}Be (g.s.)	7.5	1.04	[Gen00]
^{9}Be(d,p)^{10}Be (g.s.)	8	1.12	[Gen00]
^{9}Be(d,p)^{10}Be (g.s.)	8.5	1.01	[Gen00]
^{9}Be(d,p)^{10}Be (g.s.)	9	0.97	[Gen00]
^{9}Be(d,p)^{10}Be (g.s.)	9.5	1.01	[Gen00]
^{9}Be(d,p)^{10}Be (g.s.)	10	1.07	[Gen00]
^{9}Be(d,p)^{10}Be (g.s.)	10.5	1.08	[Gen00]
^{9}Be(d,p)^{10}Be (g.s.)	11	1.03	[Gen00]
^{9}Be(d,p)^{10}Be (g.s.)	11.8	1.44	[Sch64]
^{9}Be(d,p)^{10}Be (g.s.)	12.5	1.29	[Vas87]
^{9}Be(d,p)^{10}Be (g.s.)	15	1.83	[Dar76]
^{9}Be(d,p)^{10}Be (g.s.)	15.3	1.19	[Zel01]
^{9}Be(d,p)^{10}Be (g.s.)	17.3	0.97	[And74]
^{9}Be(d,p)^{10}Be (g.s.)	28	2.07	[Slo62]
(average)		(1.40±0.41)	
p(^{10}Be,d)^{9}Be (g.s.)	49.8*	2.99	

* Equivalent proton energy

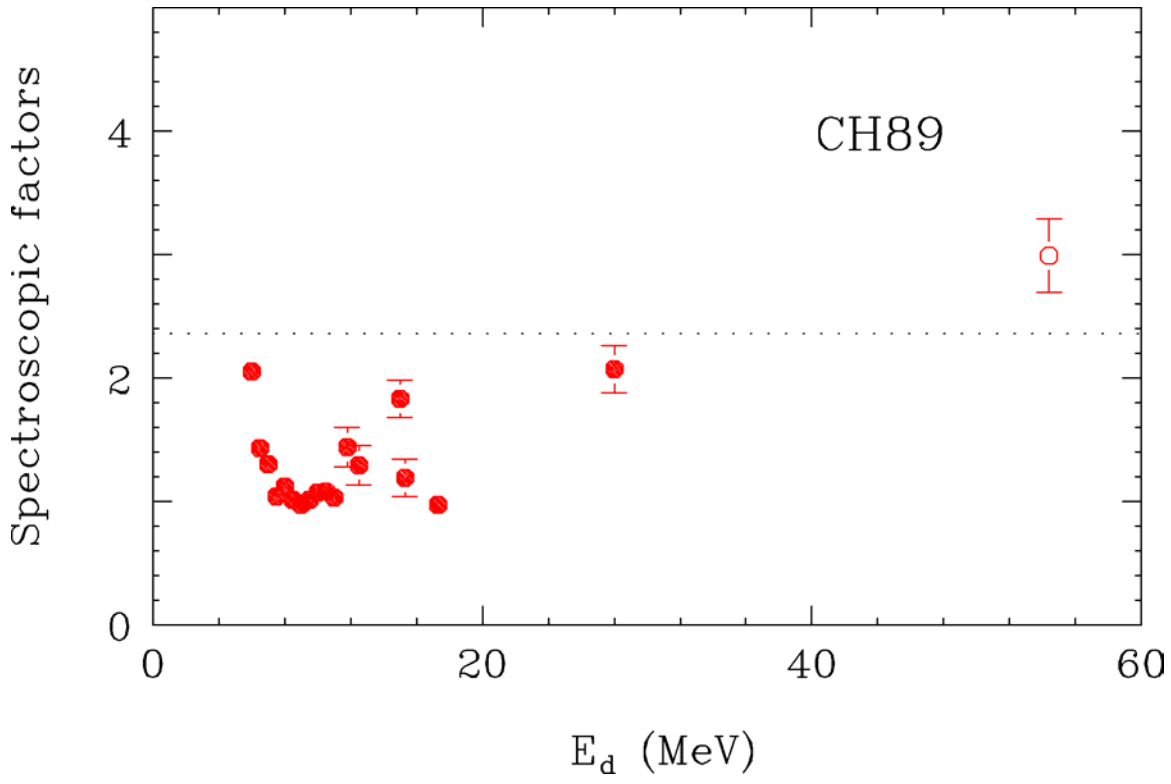

Figure 5.14: Extracted spectroscopic factors for the reactions of p(^{10}Be,d)^{9}Be (g.s.) (open square), and ^{9}Be(d,p)^{10}Be (g.s.) (closed circle). The dashed lines represent the shell model prediction of 2.35 by Cohen and Kurath [Coh67].

CHAPTER 6

SUMMARY

This experiment is originally designed to study the structure of the valence neutron of ^{10}Be and ^{11}B by extracting the spectroscopic factors. The angular differential cross sections of (p,d) reactions on ^{10}Be, ^{11}B, and ^{13}C are measured, wherein the reaction on ^{13}C is performed as a calibration system and later used as a systematic study to devise a strategy to extract spectroscopic factors using the (p,d) and (d,p) reactions. Since target of the radioactive nucleus ^{10}Be is not available, the reaction is performed in inverse kinematics. The reactions on ^{11}B and ^{13}C are also performed in inversed kinematics to keep all the three experiments similar to reduce systematic errors and to learn about the new technique of using reverse kinematics of radioactive beams. All three secondary beams are produced by bombing a thick ^{9}Be target with the ^{13}C primary beam.

This experiment provides a learning experience of how to study (p,d) transfer reactions using secondary beams. The characteristics of the reaction in inverse kinematics are analyzed in this work. The advantage of the reaction in inverse kinematics is that the emitted light particles can be easily detected at forward angles (Section 1.2). The disadvantage of the reaction in inverse kinematics is that the energy broadening requires high angular resolution of the detectors (Section 1.2). The contributions to the energy resolution are analyzed in Section 4.2, which states that thin target and high angular

resolution of the detectors are the essential keys to achieve high energy resolution for the reactions in inverse kinematics.

The angular differential cross sections are measured for the reaction of $p(^{13}C,d)^{12}C$ to the ground state (0^+) and the first excited state (2^+). The distributions are in good agreement with the published data in the literatures at adjacent energies (Section 5.3 and 5.4). The extracted SFs are in good agreement with the theory expectation. This means that the experimental techniques are good and the strategy to extract the SF works fine.

The angular differential cross sections are measured for the reaction of $p(^{11}B,d)^{10}B$ to the ground state. The extracted SF is 1.05. Past measurements give higher SF values even though this experiment in inverse kinematics presents the best agreement with the shell model prediction.

The angular differential cross sections are measured for the reaction of $p(^{10}Be,d)^{9}Be$ to the ground state. The extracted SF is 2.99, which is 27% higher than the theoretical value of 2.35. This value is not confirmed as we had problems in the beam normalization. Since the published data give lower values of spectroscopic factor, it is desirable to re-measure the differential cross section. The measurements of the differential cross sections to the excited states of ^{10}B and ^{9}Be are not performed because of the low particle counts. Therefore higher intensity of ^{11}B and ^{10}Be beams, which are available from the new Coupled Cyclotron Facility, are desirable in future measurements.

The energy resolution in this work is around 600 keV to 800 keV, which may not be high enough for the separation of some other excited states. Higher angular resolution achieved by placing the detector further away or by using smaller spacing of the strips is

desirable. This is currently under development in the construction of the HiRA (High Resolution Array) at NSCL.

In the course of this study, we have developed the strategy to extract the spectroscopic factor by using a standard set of input parameters listed in Table 2.7 for the adiabatic deuteron breakup approximation (ADBA) calculations. We find that the Optical-Model Potential (OMP) obtained from fitting individual data of elastic scatterings do not give consistent and reliable spectroscopic factors due to the ambiguity of the OMP; however, global optical-model potentials for proton and deuteron give consistent good "relative" spectroscopic factors. The OMP based on the folding model and the effective nucleon-nucleus interactions such as CH89 and JLM potentials seem to give better agreement with data.

Based on this work, specifically the analysis procedure provided, recent extraction of ground state neutron spectroscopic factors of 79 nuclei for elements ranging from Li to Cr [Tsa05]. These values are in consistent agreements with shell model predictions [Bro04]. Figure 6.1 shows the comparison of the extracted spectroscopic factors with the predictions of the modern shell model. Good agreements are achieved except for Ne, F, and Ti isotopes. Such agreement raises the possibility that the extracted spectroscopic factors are not only relative but absolute values. Furthermore, the agreement between the extracted values and the shell model predictions suggest that long-range n-n and n-core interactions can be described by modern day shell model. The disagreement between the spectroscopic factors extracted from transfer reactions and knockout reactions using the electron probe could be explained by the short-range nucleon-nucleon interactions since the electron probes the interior of the wave function where n-n interaction is more

important than that at the surface of the wave function where the transfer reactions are more sensitive. The present work has stimulated a lot of interest in the use of transfer reactions to extract spectroscopic factors, not only for rare nuclei but for stable nuclei as well.

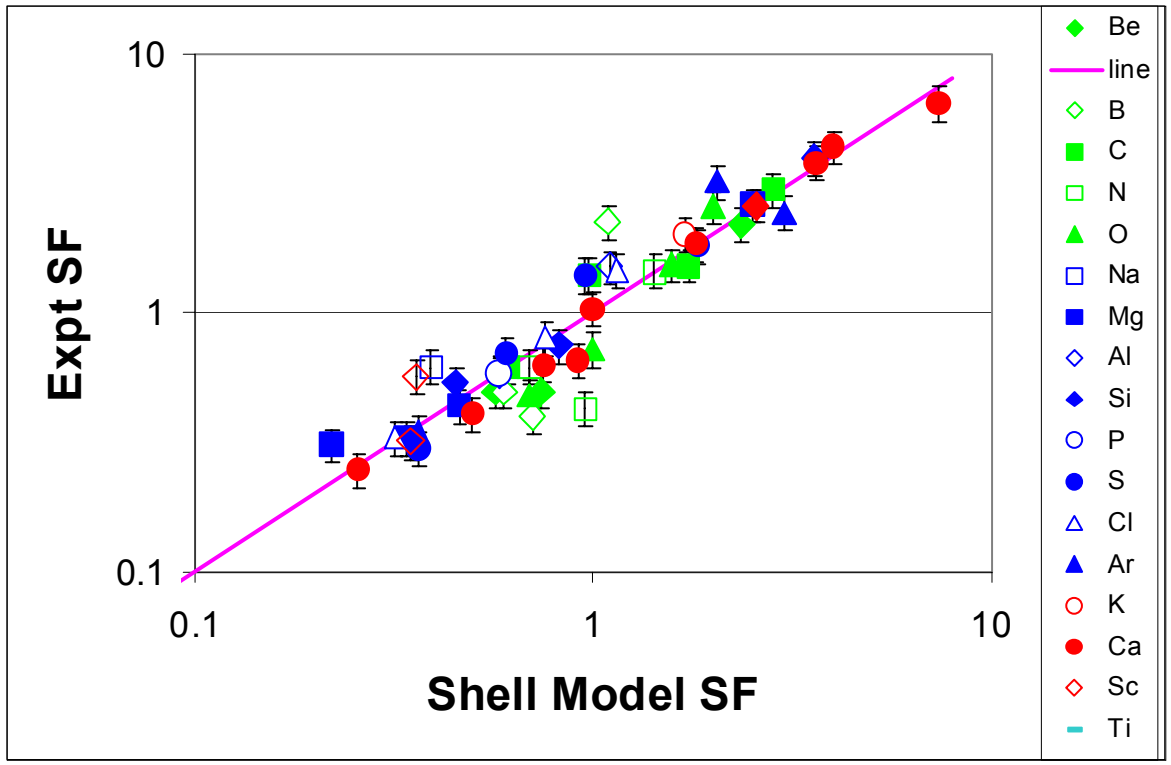

Figure 6.1: Comparison of the extracted spectroscopic factors with the predictions of the modern shell model [Bro04] for 79 nuclei ranging from Li to Cr [Tsa05]. Good agreement with most isotopes except Ne, F, and Ti isotopes.

BIBLIOGRAPHY

[And74] R. E. Anderson, J. J. Kraushaar, M. E. Rickey, and W. R. Zimmerman, Nucl. Phys. A 236, 77 (1974).

[Aus64] N. Austern, R. M. Drisko, E. C. Halbert, and G. R. Satchler, Phys. Rev. 133B, 3 (1964).

[Aus70] N. Austern, *Direct Nuclear Reaction Theories*, (Wiley, New York, 1970).

[Aus87] N. Austern, Y. Iseri, M. Kamimura, M. Kawai, G. Rawitscher, M. Yahiro, Phys. Rep. 154, 126 (1987).

[Ban85] J. M. Bang, F. G. Gareev, W. T. Pinkston, J. S. Vaagen, Phys. Rep. 125, 253 (1985).

[Bar88] A. Barbadoro, D. Consolaro, F. Pellegrini, and G. F. Segato, Phys. Rev. C 38, 517 (1988)

[Bar65] H. W. Barz, R. Fulle, D. Netzband, R. Reif, K. Schlott, and J. Slotta, Nucl. Phys. 73, 473 (1965).

[Bar96] R. M. Barnett, C. D. Carone, D. E. Groom, et al. Phys. Rev. D54, 1 (1996)

[Bec69] F. D. Bechetti, Jr. and G. W. Greenless, Phys. Rev. 182, 1190 (1969).

[Ber65] T. Berggren, Nucl. Phys. 72, 337 (1965).

[Bicr] Bicron, 12345 Kinsman Road, Newbury, Ohio 44065

[Bir51] J. B. Birks, Proc. Phys. Soc. A 64, 874 (1951).

[Bon56] T. W. Bonner, J. T. Eisinger, A. A. Kraus, Jr., and J. B. Marion, Phys. Rev. 101, 209 (1956).

[Bro04] B. A. Brown et al., Computer program, http://www.nscl.msu.edu/~brown/resources/oxbash-augsut-2004.pdf

[But51] S. T. Butler, Proc. R. Soc. London, Ser. A 208, 559 (1951).

[But64] P. J. A. Buttle and L. J. B. Goldfarb, Proc. Phys. Soc. London, 83, 701 (1964).

[But67] S. T. Butler, R. G. L. Hewitt, B. H. J. McKellar, R. M. May, Ann. Phys. (N.Y.) 43, 282 (1967).

[Cag99] J. A. Caggiano, Thesis, Michigan State University, (1999)

[Cat02] W. N. Catford, Nucl. Phys. A 701, 1c (2002).

[Cam87] J. R. Campbell, W. R. Falk, N. E. Davison, J. Knudson, R. Aryaeinejad, and R. Tkachuk, Nucl. Phys. A 470, 349 (1987).

[Coh67] S. Cohen and D. Kurath, Nucl. Phys. A 101, 1 (1967).

[Dae80] W. W. Daehnick, J. D. Childs and Z. Vrcelj, Phys. Rev. C 21, 2253 (1980).

[Dan63] R. van Dantzig and L. A. CH. Koerts, Nucl. Phys. 48, 177 (1963).

[Dar73] S. E. Darden, S. Sen, H. R. Hiddleston, J. A. Aymar and W. A. Toh, Nucl. Phys. A 208, 77 (1973).

[Dar76] S. E. Darden, G. Murillo, and S. Sen, Nucl. Phys. A 266, 29 (1976).

[Dav01] B. Davin, R. T. de Souza, R. Yanez, Y. Larochelle, R. Alfaro, H. S. Xu, A. Alexander, K. Bastin, L. Beaulien, J. Dorsett, G. Fleener, L. Gelovani, T. Lefort, J. Poehlman, R. J. Charity, L. G. Sobotka, J. Elson, A. Wagner, T. X. Liu, X. D. Liu, W. G. Lynch, L. Morris, R. Shomin, W. P. Tan, M. B. Tsang, G. Verde, J. Yurkon, Nucl. Inst. Meth. Phys. Res. A 473, 302 (2001).

[Dej74] C. W. De Jager, H. De Vries and C. De Vries, At. Data Nucl. Data Tables 14, 479 (1974).

[Del74] G. Delic, B. A. Robson, Nucl. Phys. A 232, 493 (1974).

[Dob70] J. Dobes, Nucl. Phys. A 157, 661 (1970).

[End77] P. M. Endt, At. Data Nucl. Data Tables 19, 23 (1977).

[Enlo] ENLOSS, computer program, NSCL

[Eva63] J. E. Evans, J. A. Kuehner, and E. Almqvist, Phys. Rev. 131, 1632 (1963).

[Fes92] H. Feshbach, *Theoretical Nuclear Physics: Nuclear Reactions*, (John Wiley & Sons, New York, 1992)

[Fet71] W. Fetscher, K. Sattler, E. Seibt, R. Staudt and Ch. Weddigen, in *Proceedings of the Third International Symposium on Polarization Phenomena in Nuclear Reactions*. Edited by H.H. Barschall and W. Haeberli (University of Wisconsin Press, Madison, 1971), p772.

[Fit67] W. Fitz, R. Jahr, and R. Santo, Nucl. Phys. A 101, 449 (1967)

[For99] S. Fortier, S. Pita, J. S. Winfield, et al., Phys. Lett. B 461, 22 (1999).

[Fuj89] T. Fujita, T. Fujiwara, E. Sato, and K. Nagasawa, Polymer Engineering and Science, v29, No. 18, 1237 (1989).

[Gal66] A. Gallmann, P. Fintz, P. E. Hodgson, Nucl. Phys. 82, 161 (1966).

[Gene] General Electric, Silicone Products Department, Waterford, New York 12188

[Gen00] L. N. Generalov, S. N. Abramovich, A. G. Zvenigorodskii, Bull. Rus. Acad. Sci. Phys. 64, 352 (2000)

[Gil71] V. Gillet, J. M. Normand, Nucl. Phys. A 176, 225 (1971).

[Gle04] Norman K. Glendenning, *Direct Nuclear Reactions*, (World Scientific, New Jersey ,2004).

[Gol72] L. J. B. Goldfarb and E. F. Hefter, Phys. Lett. 38B, 379 (1972).

[Gre68] G. W. Greenlees, G. J. Pyle, Y. C. Tang, Phys. Rev. 171, 1115 (1968).

[Gri75] K. A. Gridnev, E. F. Hefter, Z. Phys. A 273, 99 (1975).

[Gur69] H. Guratzsch, G. Hofmann, H. Muller, G. Stiller, Nucl. Phys. A 129, 405 (1969).

[Ha95] D. O. Handzy, Thesis, Department of Physics & Astronomy, Michigan State University, (1995)

[Ham] Hamamatsu Photonics K. K., 360 Foothill RD., Bridgewater, NJ 08807, USA

[Ham61] E. W. Hamburger, Phys. Rev. 123, 619 (1961).

[Han01] P. G. Hansen and B. M. Sherrill, Nucl. Phys. A 693, 133 (2001).

[Han03] P. G. Hansen and J. A. Tostevin, Ann. Rev. Nucl. Part. Sci. 53, 219 (2003).

[Han95] P. G. Hansen, A. S. Jensen and B. Jonson, Ann. Rev. Nucl. Part. Sci. 45, 591 (1995).

[Hav71] J. D. Harvey and R. C. Johnson, Phys. Rev. C3, 636 (1971).

[Hat84] K. Hatanaka, N. Matsuoka, T. Saito, et al., Nucl. Phys. A 419, 530 (1984).

[Hin62] S. Hinds and R. Middleton, Nucl. Phys. 38, 114 (1962).

[Hos80] K. Hosono, M. Kondo and T. Saito, Nucl. Phys. A. 343, 234 (1980).

[Iga77] M. Igarashi, et al, Computer Program TWOFNR (Surrey University version).

[Jeu77] J. -P. Jeukenne, A. Lejeune and C. Mahaux, Phys. Rev. C 15, 10 (1977) and Phys. Rev. C 16, 80 (1977).

[Joh70] R. C. Johnson and P. J. R. Soper, Phys. Rev. C 1, 976 (1970).

[Knu75] L. D. Knutson, J. A. Thomson and H. O. Meyer, Nucl. Phys. A 241, 36 (1975).

[Kul68] L. A. Kull and E. Kashy, Phys. Rev. 167, 963 (1968).

[Kunz] P. D. Kunz, DWUCK5, computer program, http://spot.colorado.edu/~kunz/DWBA.html

[Lan88] J. Lang, J. Liechti, R. Muller, et al, Nucl. Phys. A 477, 77 (1988).

[Lar94] Y. Larochelle et al., Nucl. Instr. Meth. Phys. Res. A 348, 167 (1994).

[Lee64a] L. L. Lee, J. P. Schiffer, Phys. Rev. B136, 405 (1964).

[Lee64b] L. L. Lee, J. P. Schiffer, B. Zeidman, G. R. Satchler, G. R. Drisko, R. H. Bassel, Phys. Rev. B 136, 971 (1964).

[Leg63] J. C. Legg, Phys. Rev. 129, 272 (1963).

[Liu04] X. D. Liu, M. A. Famiano, W. G. Lynch, and M. B. Tsang, Phys. Rev. C 69, 064313 (2004)

[Liu05] Tianxiao Liu, Ph.D. Thesis, Michigan State University, 2005

[Loh74] J. M. Lohr and W. Haeberli Nucl. Phys. A 232, 381 (1974).

[Mac60] M. H. Macfarlane and J. B. French, Rev. Mod. Phys. 32, 567 (1960).

[Mac74] M. H. Macfarlane and J. P. Schiffer, *Nuclear Spectroscopy and Reactions*, (Academic, New York, London, 1974), Vol. 40B, pp 170-194.

[Mad01] V. Maddalena et al., Phys. Rev. C 63, 024613 (2001).

[Mar98] Marie Ramos, *Investigating the Crosstalk Problem in the MSU Forward Array Telescope*, REU report, 1998, MSU

[Mca71] G. M. McAllen, W. T. Pinkston, G. R. Satchler, Particles Nuclei 1, 412 (1971).

[Mcg55] J. N. McGruer, E. K. Warburton, and R. S. bender, Phys. Rev. 100, 235 (1955).

[Mel83] S. Mellema, R. W. Finlay, F. S. Dietrich, and F. Petrovich, Phys. Rev. C 28, 2267 (1983).

[Men71] J. J. H. Menet, E. E. Gross, J. J. Malanify, and A. Zucker, Phys. Rev. C 4, 1114 (1971).

[Micr] Micron Superconductor LTD, 1 Royal Buildings, Marlborough Road, Lancing, Sussex BN15 8UN, UK.

[Mic99] Michael D. Lennek, *The uniformity of cesium iodide crystals*, REU report, 1999, MSU

[Mor60] S. Morita, N. Kawai, N. Takano, Y. Goto, R. Hanada, Y. Nakajima, S. Takemoto, and Y. Taegashi, J. Phys. Soc. Japan, 15, 550 (1960).

[Mye73] W. D. Myers, Nucl. Phys. A 204, 465 (1973).

[Neg70] J. W. Negele, Phys. Rev. C1, 1260 (1970).

[New67] E. Newman, L. C. Becker, and B. M. Preedom, and J. C. Hiebert, Nucl. Phys. A 100, 225 (1967)

[Oga99] Yu. Ts. Oganessian et al. Phys. Rev. Lett. 82, 4996 (1999).

[Ohl63] G. G. Ohlsen and R. E. Shamu, Nucl. Phys. 45, 523 (1963).

[Ohn86] H. Ohnuma, N. Hoshino, O. Mikoshiba, et al., Nucl. Phys. A 448, 205 (1986).

[Pea66] C. A. Pearson, M. Coz, Nucl. Phys. 82, 545 (1966).

[Per62] F. Perey and B. Buck, Nucl. Phys. 32, 353 (1962).

[Per74] F. G. Perey, in *Nuclear spectroscopic and Reactions*, edited by J. Cerny (Academic, New York, 1974), pt. B, p.137

[Per76] C. M. Perey and F. G. Perey, At. Data Nucl. Data Tables 17, p6 (1976).

[Pet85] J. S. Petler, M. S. Islam, R. W. Finlay, and F. S. Dietrich, Phys. Rev. C 32, 673 (1985).

[Phi68] R. J. Philpott, W. T. Pinkston, G. R. Satchler, Nucl. Phys. A 119, 241 (1968).

[Pin65] W. T. Pinkston, G. R. Satchler, Nucl. Phys. 72, 641 (1965).

[Pin69] W. T. Pinkston, R. J. Philpott, G.R. Satchler, Nucl. Phys. A 125, 176 (1969).

[Pre75] M. A. Preston and R. K. Bhaduri, *Structure of the Nucleus* (Addison-Wesley, Reading, MA, 1975)

[Put71] G. D. Putt, Nucl. Phys. A 161, 547 (1971).

[Reh98] K. E. Rehm et al., Phys. Rev. Lett. 80, 676 (1998).

[Rob61] D. Robson, Nucl. Phys. 22, 34 (1961).

[Sat71] G. R. Satchler, Phys. Rev. C 4, 1485 (1971).

[Sat83] G. R. Satchler, *Direct Nuclear Reactions* (Oxford University, Oxford, 1983).

[Saw67] T. Sawaguri and W. Tobocman, J. Math. Phys. 8, 2223 (1967).

[Sch64] U. Schmidt-Rohr, R. Stock, and P. Turek, Nucl. Phys. A 53, 77 (1964).

[Sch67] J. P. Schiffer, G. C. Morrison, R. H. Siemssen, and B. Zeidman, Phys. Rev. 164, 164 (1967) and Phys. Rev. 164, 1274 (1967).

[Scio] Scionix Holland BV, P.O.Box 143, 3980 CC Bunnik, The Netherlands.

[Sco70] D. K. Scott, P. M. Portner, J. M. Nelson, et al. Nucl. Phys. A 141, 497 (1970).

[Slo62] R. J. Slobodrian, Phys. Rev. 126, 1059 (1962).

[Smi63] W. R. Smith and E. V. Ivash, Phys. Rev. 131, 304 (1963).

[Srim] SRIM, *The Stopping and Range of Ions in Matter*, computer program, http://www.srim.org/

[Tak68] H. Taketani, J. Muto, H. Yamaguchi and J. Kokame, Phys. Lett. 27B, 625 (1968).

[Tan02] Wanpeng Tan, Ph.D. Thesis, Michigan State University, 2002.

[Toy95] H. Toyokawa, H. Ohnuma, Y. Tajima, et al., Phys. Rev. C 51, 2592 (1995).

[Tsa05] M. B. Tsang, H. C. Lee, B. A. Brown, X. D. Liu, W. G. Lynch, and J. A. Tostevin, to be published, 2005

[Var91] R. L. Varner, W. J. Thompson, T. L. McAbee, E. J. Ludwig and T. B. Clegg, Phys. Rep. 201, 57 (1991).

[Vas87] O. I. Vasileva, G. S. Durevich, A. V. Ignatenko, V. M. Lebedev, N. V. Orlova, A. V. Spassky, I. B. Teplov, L. N. Fateeva, G. V. Shakhvorostova, A. Kh. El-Kamkhavi, Yad. Fiz. 45, 312 (1987)

[Ver94] J. Vernotte, G. Berrier-Ronsin, J. Kalifa, R. Tamisier, B. H. Wildenthal, Nucl. Phys. A 571, 1 (1994).

[Wat58] S. Watanabe, Nucl. Phys. 8484, 484 (1958).

[Wel78] H. R. Weller, J. Szücs, P. G. Ikossi, J. A. Kuehner, and D. T. Petty, Phys. Rev. C 18, 1120 (1978)

[Win01] J. S. Winfield, S. Fortier, W. N. Catford, et al., Nucl. Phys. A 683, 48 (2001).

[Wag01] A. Wagner, W. P. Tan, K. Chalut, R. J. Charity, B. Davin, Y. Larochelle, M. D. Lennek, T. X. Liu, X. D. Liu, W. G. Lynch, A. M. Ramos, R. Shomin, L. G. Sobotka, R. T. de Souza, M. B. Tsang, G. Verde, H. S. Xu, Nucl. Instr. Meth. Phys. Res. A 456, 290 (2001).

[Woo54] R. D. Woods and D. S. Saxon, Phys. Rev. 95, 577 (1954).

[Yur99] J. Yurkon, D. Bazin, W. Benenson, D. J. Morrissey, B. M. Sherrill, D. Swan, and R. Swanson. Focal plane detector for the S800 high-resolution spectrometer. Nucl. Instr. Meth. Phys. Res. 422, 291-295 (1999).

[Zai61] N. I. Zaika, O. F. Nemets, and S. Tserino, Soviet Phys. JETP 12, 1 (1961).

[Zel01] N. S. Zelenskaya, A. V. Ignatenko, V. M. Lebedev, N. V. Orlova, A. V. Spassky, Phys. Atomic Nuclei, 64, 1909 (2001).

[Zha97] B. Zhang, Ph.D. Thesis, Michigan State University, (1997)